Threshold Raw Retrieved Contrast in Coronagraphs Is Limited by Internal Polarization

Final Report for NASA Grant # NNX17AB29G

James Breckinridge,
Principal Investigator
Wyant College of Optical Sciences, University of Arizona, Tucson AZ

Russell A. Chipman,
Co-Investigator
Wyant College of Optical Sciences, University of Arizona, Tucson AZ

Meredith Kupinski,
Research Professor
Wyant College of Optical Sciences

James E. Harvey,
Retired Professor
University of Central Florida College of Optics and Photonics (CREOL)
Photon Engineering, Tucson AZ

Jeffrey Davis & Brian Daugherty,
Graduate Students
Wyant College of Optical Sciences, University of Arizona, Tucson AZ

Signature Page

James Breckinridge,	Date
Principal Investigator	
Wyant College of Optical Sciences,	
University of Arizona, Tucson AZ	

Nicholas Siegler,	Date
Program Chief Technologist	
Exoplanet Exploration Program,	
NASA/JPL – California Institute of Technology	

Brendan Crill,	Date
Deputy Program Chief Technologist	
Exoplanet Exploration Program,	
NASA/JPL – California Institute of Technology	

Douglas Hudgins,	Date
Program Scientist	
Exoplanet Exploration Program,	
Science Mission Directorate, NASA HQ	

This research was carried out by the J. C. Wyant College of Optical Sciences of the University of Arizona, in Tucson, AZ under a contract with the National Aeronautics and Space Administration.

Reference herein to any specific commercial product, process, or service by trade name, trademark, manufacturer, or otherwise, does not constitute or imply its endorsement by the United States Government, the Jet Propulsion Laboratory, California Institute of Technology, or the University of Arizona.

Preface

Three primary investigators performed this work:

James Breckinridge, PhD. His career spans 50 years designing and building astronomical instruments, technical management, research and teaching including 3 years at Lick Observatory, 12 years at KPNO, 6 years at the College of Optical Sciences U of A., 33 years at NASA/JPL, 10 years lecturer and adjunct professor Caltech and the College of Optical Sciences U of Az. He is the author of over 160 research papers in atomic spectroscopy, solar physics, physical optics, stellar astrophysics, interferometry, atmospheric optics and space-flight optical instruments. He was the project instrument scientist and science co-investigator for the Atmospheric Trace Molecule Spectroscopy (ATMOS) flight science/instrument that flew successfully three times on the Space Shuttle to record over 10,000, one-million point spectra of the earth's stratosphere at .02 cm^{-1} spectral resolution from 2 to 16μ.

In addition, he authored one textbook (Basic Optics for the Astronomical Sciences), one book chapter, and created the new optical science and engineering section at JPL/Caltech by interviewing, hiring and funding over 35 optical scientists and engineers between 1982 and 1994. The section delivered opto-mechanical space flight hardware for Galileo, Cassini, earth and planetary cameras and spectrometers as well as WF/PC2 for HST. In addition, the section was responsible for the development of innovative science instrument concepts such as exoplanet coronagraphs, large aperture deployable space telescopes and parallax cameras. Breckinridge served on the HST NASA failure review board and led the section responsible for the optics repair using the WF/PC2 camera.

Breckinridge managed the Advanced Technology and Instruments (ATI) program for NSF for 3 years and served 1-year as the acting Chief Technologist for the NASA SMD Astronomy Division. Dr. Breckinridge was associate editor for Applied Optics between 1985 and 1995 and is currently an associate editor of the Journal of Astronomical Telescopes, Instruments and Systems (JATIS). He is currently on the faculty in the Astronomy department at Caltech and the College of Optical Sciences, U of A.

Breckinridge[1] was the first (1984) to describe a coronagraph camera for direct imaging exoplanets with a space telescope. Twenty years later, Oppenheimer and Breckinridge[2] published calculations showing that internal instrument/telescope polarization limits our ability to characterize exoplanets. It required ten additional years before the work described here was funded.

Professor Russell A. Chipman's career spans 40 years in optical system engineering, fabrication, test, calibration and analysis of instruments for remote sensing optical/UV/IR polarization metrology, materials science and analysis. He has directed the research of over 35 PhD students during his academic career. Dr. Chipman is the chief innovator and architect for the creation and development of the new vector-wave polarization ray trace analysis software: Polaris-

---

[1] J. B. Breckinridge, T. G. Kuper and R. V. Shack (1984) *Space Telescope low-scattered light camera: a model*, Optical Engineering 23, 816 to 820.

[2] B. Oppenheimer and J. Breckinridge (2004) *Polarization effects in reflecting coronagraphs for white-light applications in astronomy,* ApJ 600:1091-1098.

M, which is becoming the industry standard. Professor Chipman developed and has taught the 2-semester polarization class at the College of Optical Sciences for over 10-years. In 2007 he was awarded the SPIE G.G. Stokes award in Polarization Optics and in 2015 he was awarded the Optical Society of America Joseph Fraunhofer Award/Robert M. Burkley Prize.

Professor Meredith Kupinski, Research Professor, College of Optical Sciences, teaches the two upper division graduate classes in polarization at the University of Arizona. In addition to polarization her specialties include inverse problems, task-relevant metrics for imaging system design, estimation/detection theory in medical imaging, and stochastic systems analysis and information quantitation. Dr. Kupinski received the NSF's Fellowship for Science, Engineering, and Education for Sustainability from 2013 to 2016. In 2018 she was awarded a d'Alembert Fellowship to study polarimetry for cervical cancer detection at Ecole Polytechnique in France.

Motivation

In 1990, during the time this PI was the JPL manager responsible for JPL space optics, he was one of two technical advisors on the HST NASA failure review board and saw first-hand how fundamental physical-optics principles are neglected at the expense of the astronomy-science space optics community. The optical system requirements needed to characterize terrestrial exoplanets are far more difficult to meet than were the HST or JWST requirements. The fundamental physical optics of image formation in high performance coronagraphs is complicated enough without building in obstacles to success. He feels a strong responsibility to assure that another "optics anomaly" does not happen to astrophysics, only this time, over the characterization of terrestrial exoplanets.

In 2015 after several years of scientific and technical presentations at AAS meetings, IAU, NASA HQ, NASA GSFC/JPL, STSci, Northrop Grumman (TRW), Ball, Carnegie, Lockheed, SPIE and NSF events as well as 5 published papers, and personal 1:1 meetings with a member of a NASA science board and the NAS, the proposal, whose results are reported here was funded at the $600 K level by the NASA TDEM office.

Terrestrial exoplanet characterization technology

The work presented here is focused on those optical system technologies for the direct imaging and spectroscopy of terrestrial exoplanets using internal instrument masks. The formation flying external mask system, called starshade, requires similar technologies but with different requirements are not covered in this work.

Several metrics are used to describe terrestrial exoplanet telescope/instrument technology. The primary one is contrast. Technology to control contrast is conveniently divided into two parts: dynamic and static. Technology to control dynamic contrast include spacecraft pointing and control, thermal, and adaptive optics. Technologies to control static contrast include optical thin films, mirrors, devices (Dichroic mirrors and substrates), windows (filters) surface and bulk scatter, polarization and baffles (light traps). Control of dynamic contrast and static contrast are mutually dependent. That is each one is necessary, but not sufficient. Therefore, they interact in a system sense and require an end-to-end optical systems analysis for a mission readiness assessment.

It is more difficult to characterize terrestrial exoplanets than giant planets. Planets that shine in reflected starlight are very faint and difficult to measure in the presence very bright light from the parent star. The metric contrast is defined as the ratio of the brightness of the exoplanet divided by the brightness of the star. Let us use the symbol C_T to refer to system contrasts needed to characterize the atmosphere, chemistry and surface features of TERRESTRIAL exoplanets. Terrestrial exoplanets are of interest because these may harbor indications of life or, at least an

opportunity for life as we know it to have evolved.

Let us use the symbol C_G to refer to system contrasts needed to characterize the atmosphere, chemistry and surface features of GIANT exoplanets. By characterization we mean to make direct measurements of light from the exoplanet and its surroundings to reveal the atmosphere, chemistry, surface chemistry/geology, seasons, rotation rate and orbital inclination.

We distinguish between telescope/coronagraph systems for terrestrial exoplanet characterization ($10^{-10}<C_T<10^{-8}$) and those for giant planet characterization ($10^{-6}<C_G<10^{-8}$). Some of the optical and opto-mechanical technology requirements are different between the two. Systems to characterize terrestrial exoplanets carry requirements that are significantly more difficult to achieve than those system optimized for characterization of giant planets.

 For example, the 2.4-meter clear aperture WFIRST-CGI system will for the most part characterize Giant exoplanets. Since WFIRST-CGI is an approved flight mission in pre-phase A, the technology is flight ready by definition at TRL>5. And no further technology development or investments are needed or wanted and NASA can move with confidence into a fixed-price "fab-to-print program" with an industrial provider.

Many WFIRST-CGI project reports imply that the telescope/coronagraph system will record spectra with useful SNR for exoplanets at contrast levels of 10^{-10} at the IWA. However, this number is calculated without scattered light and without the polarization aberrations contributed by the mirrors, filters and windows.

TABLE OF CONTENTS

TABLE OF FIGURES

TABLE OF TABLES

Executive Summary

We apply the analysis tools of vector wave E&M to investigate the optical performance of space-based exoplanet coronagraph/telescope systems for the characterization of terrestrial exoplanets. We investigate in detail polarization properties of exoplanet optical systems and their subsystems, as well as discuss the roles diffraction and scattered light in telescopes/coronagraph systems designed to characterize terrestrial exoplanets. The analysis tools we used were: (1) Polaris-M, a computer-aided design (CAD) polarization ray-trace software program, (2) Vector-wave modeling of electromagnetic radiation, (3) Image formation theory, and (4) FRED, a CAD program that uses Gaussian beam propagation to accurately model complex-wave diffraction.

The Wide Field Infrared Survey Telescope/Coronagraph Instrument (WFIRST-CGI) fore-optics were raytraced with both CODE-V and Polaris-M. The surface ray intercept height differences were less than 10^{-6} mm and demonstrated that the two ray-trace programs are in agreement. The terrestrial exoplanet telescope/coronagraph systems, Habitable Exoplanet Observatory (HabEx) and the Large Ultraviolet Optical Infrared Surveyor (LUVOIR), were polarization ray-trace modeled to give: diattenuation maps and retardance maps of individual optical elements, Jones pupil and coronagraph point spread function (PSF) for HabEx, and Jones pupil and occulting mask PSF for LUVOIR. The results for LUVOIR were delivered to the team at NASA's Goddard Space Flight Center (NASA/GSFC) and those for HabEx were delivered to NASA's Jet Propulsion Laboratory.

Large aperture primary mirrors were found to exhibit polarization reflectivity variations across the surface, caused by thin film anisotropies which introduce spatially-dependent form birefringence. A 3.75-meter diameter spherical test mirror was measured for form birefringence and the values were rescaled to 4-meters and placed over the primary HabEx mirror. We compared contrast calculated using an isotropic coated primary with that calculated using the measured values and found that the contrast was reduced by about a factor of 50 for the realistic primary.

For NASA to develop a mission capable of coronagraphic direct imaging of temperate terrestrial planets in the habitable zone of solar type stars, an essential step will be to consider the design parameters of polarization aberration analysis and scattered light analysis and their effects on coronagraph contrast performance in addition to alignment sensitivities/tolerances and the environmental effects of optical contamination, thermal, structural, radiation damage, test, and end-to-end optical system calibration and performance validation.

Three milestones were successfully met.

Alternative ways to segment a large aperture were investigated to find a more efficient aperture topology than the hex segmentation used by LUVOIR. Preliminary results indicate that a spiral or "pinwheel" topology may be more efficient for exoplanet science. Further investigation is recommended. This topology may make bore-sight roll of the telescope unnecessary and therefore increase the number of objects observed during the mission significantly.

1   SUMMARY

1.1   EXOPLANET TECHNOLOGY ADVISORY COMMITTEE (TAC)–APPROVED MILESTONES

1. **Milestone 1:** Conduct a polarization aberration analysis of the WFIRST-CGI optical system from object space to the occulting-mask image plane using Polaris-M software. Calculate the intensity profiles across the occulting-mask image plane for each of the four polarization terms: I_{XX}, I_{YY}, I_{XY} and I_{YX}. Calculate the difference between those profiles determined by CODE V and those calculated by Polaris-M. If the difference between these profiles exceeds a 3% window, then provide narrative comment on the potential reasons for the difference.

    a. Results from the two codes agree to less than one part in 10^{+3} or 0.1%.

    b. Data in **Table 4-1**, below, show that the ray intercepts on each of the 20 surfaces within WFIRST-CGI differ by less than 3×10^{-7} mm, well within the rounding errors of the computation.

    c. The CAD ray trace codes Polaris-M and Code-V are in full agreement based on a comparison of the ray intercept calculations. Milestone # 1 did not request a comparison of contrast calculations and JPL did not provide the optical prescription for WFIRST-CGI end to end system to enable such a calculation and comparison. Milestone # 1 was completely successful.

2. **Milestone 2:** Collaborate as members of the LUVOIR and HabEx teams to conduct polarization aberration analyses of LUVOIR and HabEx optical systems from object space to the detector using Polaris-M software.

    a. Provided the HabEx team with Jones pupil polarization maps at the final exit pupil to the Lyot coronagraph image plane. Collaborated with the HabEx teams, led by D. Mawet and J. Krist, to produce a paper summarizing HabEx instrument polarization and contrast. Krist, Martin, Kuan, Mennesson, Ruane and Breckinridge (2019) Numerical modeling of the HabEx coronagraph, Proc SPIE 11117-17.

    b. Provided the LUVOIR team with Jones pupil polarization maps at the exit pupil of the fore-optics to the coronagraph.

    c. We requested a baseline design for a Lyot coronagraph from the LUVOIR program office, so we could run our polarization analysis through to the final image plane, but none was provided. In an effort to solve this, we designed a Lyot coronagraph with a vector vortex (VV6) occulting mask for LUVOIR based on open literature information. We discovered that it performed poorly in the presence of the LUVOIR segment gaps. This inspired us to study alternative segmentation topologies and create the "pinwheel" aperture.

    d. Milestone # 2 was successful.

3. **Milestone 3:** Polarization reflectivity anisotropy. Use laboratory apparatus to measure the spatial distribution of the form birefringence from a large (3.875) mirror with a "typical" astronomical coating. Achieve a measurement sensitivity of 1-milli-fringe at 500-nm.

a.   Measured a 3.8-meter diameter "primary" mirror with an Al thin-film coating identical to that used on the Kitt Peak National Observatory (KPNO) 4-meter Mayall astronomical telescope. We discovered a low spatial frequency pattern, or map, across the mirror that exhibits 0.002 radians retardance. We placed this map over the primary mirror of HabEx, performed a polarization ray-trace, and established that if this standard coating was used on the flight mirror, coronagraph contrast would be degraded by ~1.5 orders of magnitude. JPL engineers were provided with funding by this TDEM to assist us in the interpretation of the JPL Falco software modules. Unfortunately, other priorities prohibited JPL from assisting us, and we were unable to use Falco, or the engineering properties of their typical A/O to optimize contrast for HabEx. However, there is no doubt that the polarization form birefringence that results from modern coating techniques on large aperture mirrors contributes significantly to contrast loss. And these effects are not present in the subscale JPL test beds systems which do not represent the performance of space optical systems.

b.   Milestone #3 was successful.

We successfully provided the HabEx team with Jones exit pupil polarization maps for the final focal plane. The Jones pupil consists of four complex electric field distributions. The digital computation of these sets of four fields were repeated three times, once each for different HabEx baseline mirror metal coatings: (1) Primary and secondary mirrors assumed isotropic dielectric coated metal aluminum and all the following mirrors to the focal plane assumed dielectric coated silver., (2) All of the HabEx mirrors assumed perfectly reflecting, and (3) All metal mirrors isotropic except the 4-m primary metal mirror which was given the form birefringence values measured as part of Milestone #3.

In all three cases contrast was calculated and compared to show how polarization reflectivity variations across a large primary mirror affects contrast. This part of the Milestone # 2 work was 100% successful. The planned and budgeted software consulting needed by our team from JPL engineers was not available during the period we needed it and we could not optimize the polarization aberrated HabEx optical system for contrast using the JPL baseline Falco process.

We delivered to the GSFC LUVOIR team: cumulative Jones exit pupil maps for the wavefront reflecting from an isotropically coated segmented primary mirror to the exit pupil plane just before the image plane where the VV6 is located. This was completed for the mirror coating recipes provided by Goddard. The LUVOIR team at GSFC processed these further.

As part of the original award, NASA HQ awarded $26K directly to JPL to support this task. The planned and budgeted software consulting needed by our team from JPL engineers was not available during the period we needed it and we were unable to optimize the polarization aberrated HabEx optical system for contrast using the JPL baseline FALCO process and compare results.

However, we did successfully calculate and compare contrast estimates under three optical system conditions for the HabEx design: 1. All mirror coatings are perfectly isotropic metal, 2. Each mirror surface introduces no polarization and 3. The primary mirror exhibits polarization reflectivity anisotropy characteristic of that measured for the 3.75-m test mirror. We conclude that the uncorrected form birefringence we discovered on the primary mirror will reduce contrast at all working angles across the field by a factor of 10 to 50.

We conclude that optimized terrestrial exoplanet telescope/coronagraph systems require development of large aperture, and thus large surface area optical highly reflecting thin films.

1.2   PUBLICATIONS AND DISSERTATIONS THAT SUMMARIZE WORK FUNDED BY THIS TASK

1.   J. B. Breckinridge, J. E. Harvey, R. Irvin, R. Chipman, M. Kupinski, J. Davis, D-W Kim, D. S. Ewen, C. F. Lillie and T. Hull (2019) *ExoPlanet Optics: conceptual design process for stealth telescopes*, Proc. SPIE 11115-17

2.   James E. Harvey, James B. Breckinridge, Ryan G Irvin, Richard N. Pfister, (2018) *Novel Designs for minimizing diffraction effects in large segmented mirror telescopes*, SPIE 10745 -0L

3.   Richard N. Pfister, James E. Harvey, James B. Breckinridge (2018) The role of narrow-angle forward surface scatter and particulate scatter in exoplanet exploration, SPIE 10698-5F

4.   Jeffrey Davis, Meredith K. Kupinski, Russell A. Chipman, and James B. Breckinridge (2018) *HabEx Polarization Ray Trace and Aberration Analysis* SPIE 10698-3H

5.   J. B. Breckinridge, M. Kupinski, J. Davis, B. Daugherty and R. A. Chipman (2018) *Terrestrial exoplanet coronagraph image quality polarization aberrations in HabEx*. SPIE 10698-1D

6.   J. E. Harvey, R. G. Irvin, K. Crabtree and J. B. Breckinridge (2018) *Diffraction analysis of large segmented mirror concepts for exoplanet exploration* SPIE 10698-1Q

7.   J. B. Breckinridge, J. E. Harvey, K. Crabtree, et. Al. (2018) *ExoPlanet telescope diffracted light minimized: the pinwheel pupil solution*, SPIE Proc 10698-1P

8.   J. B. Breckinridge (2018) The Pinwheel pupil Discovery: exoplanet science and improved processing with segmented telescopes, Paper 439.04 presented at Amer. Ast. Soc. 231st meeting Washington DC 8-12 Jan.

9.   Lillie, C. F. and J. B. Breckinridge (2016) Prime focus architectures for large space telescopes: reduce surfaces to save cost, Proc SPIE 9904 – 4K

10.   PhD dissertations from the Wyant College of Optical Sciences, University of Arizona, Tucson AZ.:

- •   Jeffrey Davis (2019) *Polarization aberrations in coronagraphs*, 227 pages

- •   Brian J. Daugherty (2019) *Advances in Polarization Engineering- chapter 1 titled Form Birefringence of a 3.75-m Aluminum Mirror* pp 15-60.

1.3   PAPERS SUBMITTED OR IN PREPARATION REPORTING RESULTS FUNDED BY THIS CONTRACT

11.   J. B. Breckinridge, J. E. Harvey, M. Kupinski (2020) *The role of internal polarization and system diffraction in exoplanet science*, JATIS - in preparation.

1.4 EARLIER (2004–2016) WORK THAT REVEALED THE IMPORTANCE OF INSTRUMENT POLARIZATION TO CORONAGRAPH IMAGE FORMATION AND CONTRAST LEVELS TO ACHIEVE TERRESTRIAL EXOPLANET SCIENCE

12. J. B. Breckinridge and R. A. Chipman (2016) Telescope polarization and image quality: Lyot coronagraph performance SPIE Proc 9904-1C

13. Russell A. Chipman, Wai Sze T. Lam and James B. Breckinridge Polarization Aberration in Astronomical Telescopes, Proc. SPIE 9613-16, Polarization Science and Remote Sensing VII , San Diego, CA 2015

14. James B. Breckinridge, Wai Sze T. Lam and Russell A. Chipman, Polarization Aberrations in Astronomical Telescopes: The Point Spread Function, Publications of the Astronomical Society of the Pacific (PASP), 127**:445–468** May 2015

15. James B. Breckinridge, Self-induced polarization anisoplanatism, SPIE 8860-39, 2013.

16. N. Clark & Breckinridge, J. Polarization compensation of Fresnel aberrations in telescopes. 2011 SPIE 8146 # 81460O

17. James B. Breckinridge, Challenges to optimizing a telescope system to detect and characterize exo-solar planetary systems. SPIE 5875-08 (2005)

18. J. B. Breckinridge, Image Formation in High Contrast Optical Systems: The role of polarization. SPIE proceedings 5487 page 1337-1345.

19. J. B. Breckinridge and B. Oppenheimer, Polarization Effects in Reflecting Coronagraphs for White Light Applications in Astronomy, Astrophysical Journal, 600, pp 1091 – 1098. January 10, 2004

1.5 SUGGESTED FUTURE WORK

1. Complete a comprehensive investigation of the contrast-degradation caused by the fabrication-induced, measured form-birefringence that is modeled on the 4-m HabEx primary mirror and fully evaluate the ability of A/O to correct for this deficiency, using current state of the art modeling tools such as Falco and knowledge of the construction of physical A/O devices.

2. Investigate the stability of system contrast estimates determined by the use of different computational platforms & methods using realistic digital model representations of optical surfaces and devices in coronagraphs and suggest mitigation strategies.

3. Investigate the effects on contrast of coating (metal and dielectric) polarization anisotropies present on optical devices that are used in coronagraphs, such as VV6 masks, dichroic mirrors, A/O mirrors, large apertures (monolithic & segmented), fold flats and powered optical elements.

4. For the purpose of providing structure and guidance to the technology program: Perform the end-to-end optical system analysis of a point-design for a terrestrial exoplanet coronagraph/spectrometer system to identify subsystem functional requirements for each technology device in the system whose technology readiness level (TRL) is less than

acceptable for flight. Flow these subsystem functional requirements to engineering performance requirements and identify needed sub-subsystem technology developments that will meet the engineering performance requirements. Examples of devices are: A/O (metrology, sensing and actuation), coatings, beam-splitters, polarizers, dispersing elements, and occulting plane masks.

5.   Investigate the role of narrow angle forward scattered light given by real-world mirrors on terrestrial exoplanet contrast and the performance of A/O. Suggest mitigation strategies if narrow angle forward scatter have a deleterious effect on exoplanet contrast or the performance of the A/O.

6.   Investigate innovative large aperture pupil topologies that will increase exoplanet yield, reduce diffraction and scattered light at reduced schedule and cost, such as the pinwheel pupil. Insert Lyot coronagraph into a pinwheel aperture and investigate its effects on contrast and dynamic range. For example: replace the primary of LUVOIR with the pinwheel pupil and compare the performance of the two. Investigate the relationship between segment curvatures, diffraction, contrast, fabrication cost, and system transmission, including signal-to-noise ratio (SNR) and compatibility with a spectrometer, optimized for exoplanet spectroscopy.

7.   Investigate materials, coatings and their processing methods and space-optics compatibility to minimize polarization aberrations, maximize system transmittance, and minimize narrow angle forward scatter for terrestrial exoplanet coronagraph optical systems to be integrated into either a pinwheel or hex segment primary mirror aperture topology.

8.   J. Breckinridge and N. Clark (Polarization compensation of Fresnel aberrations in telescopes. 109 2011 SPIE 8146 # 81460O) suggested the implementation of a spatially variable retardance plate (SVRP) to correct polarization aberrations in telescopes and instruments, including terrestrial exoplanet coronagraphs. Investigate the utility of using the SVRP device to improve terrestrial exoplanet optical system performance.

9.   Investigate the fabrication of the pinwheel aperture, including deployment, back-up structure, and opto-mechanical deformation issues and compare with those for a hex segment aperture, such as James Webb Space Telescope (JWST) and LUVOIR.

10. Current operations models require that the in-space telescope be rolled along the boresight axis. This increases spacecraft mission operations and data processing cost in addition to increasing integration time and thus the total number of objects available to observe during a mission flight life time. Investigate innovative optical designs for the end-to-end telescope coronagraph system that will mitigate this need and therefore increase mission yield.

11. Vector diffraction from secondary support structures and segment gaps cause unwanted variations in background electric field across the telescope/coronagraph image plane. Investigate the source of these variations to assess the extent to which A/O can correct for them. For example: by adjusting the pair of deformable mirrors (DM) that form the optical cavity in the coronagraph is it possible to shift the final image plane background electric field around the image plane to maximize local contrast. Quantitatively compare hex and pinwheel segment diffraction patterns and define metrics for two different situations: reconnaissance of exoplanet systems of unknown content, and follow-up of known exoplanets.

12. Dichroic filters are typically used in astronomical instruments to separate wavebands to enable imaging the same object at several wavelengths simultaneously. The HabEx optical system contains a dichroic filter used to separate wavelengths into different coronagraphs. Currently, dichroic filters are modeled as dummy planes with no optical power, index or polarization properties. However, this is wrong! Dichroics use the wavelength dependent polarization properties of optical thin films to separate wavebands. Investigate to determine if these properties are responsible for changes in contrast at the coronagraph image plane and recommend mitigation strategies.

13. Laboratory coronagraph systems exhibit a decrease in contrast as wavelength bandpass increases. Investigate the source of this phenomena, believed to be chromatic aberration in the polarization aberrations and develop technology to achromatize terrestrial exoplanet coronagraphs to enable observations of fainter exoplanets.

1.6   MISSION DESIGN COMMENTS

Some guidelines for telescope/coronagraph mission design derived from our work here are:

1. Minimize the number of optical surfaces, windows and filters in the optical path.

2. Minimize the angle of incidence, consistent with space-craft packaging constraints, and thus the angles of reflection of all optical beams in the path.

3. Maximize the F/# on powered optical elements, consistent with space-craft packaging constraints, to reduce the marginal ray angle of deviation.

4. Mount optical elements so the surfaces that reflect or transmit light can be easily cleaned.

5. Eliminate or minimize all obstructions that cause the aperture and the exit pupil to appear to be discontinuous surfaces.

6. Investigate optical system architectures and processing methodologies to minimize the need for boresight roll of the space-flight telescope system.

7. Investigate and develop performance test methodologies and system hardware approaches that will enable accurate prediction of the on-orbit end-to-end optical system performance prior to launch, including scientific calibration of contrast and field of view performance. That is, investigate what do we need to build into the system before the Preliminary Design Review (PDR) that will enable accurate scientific calibration.

1.7   LESSONS LEARNED

1. Polarization aberrations play a critical role in the design and implementation of terrestrial exoplanet coronagraphs. Telescope/coronagraph system contrast depends on the control of polarization. These aberrations are caused by optical anisotropies within windows, and filters and metal thin film coatings on the mirrors required to maintain the high transmittance and throughput necessary to image the faint terrestrial exoplanets and to control unwanted scattered light. For example, form birefringence, introduced during the fabrication of a large aperture (4-m) reflecting surface may reduce contrast by a factor of 100.

2. Polarization aberrations are mitigated in several ways: (1) Implement an opto-mechanical layout that minimizes angles of incidence on flat mirrors and minimizes the number of compound angles in the layout, (2) Use powered optical elements with high F/#, (3) Use isotropic mirror coatings, (4) Minimize the use of dielectric coatings on mirrors and filters, and (5). Implement a spatially variable retardance plate (SVRP).

3. Large aperture telescopes that are segmented by tiling the aperture with hexagonally shaped mirrors may not be optimum for the detection and characterization of exoplanets. Segmenting the aperture using a spiral or pinwheel pattern appears to produce a more efficient diffraction pattern for exoplanet science.

4. The role of optical surface scatter and narrow angle forward scattered light has not been investigated for terrestrial exoplanet coronagraphy. A literature search and preliminary calculations indicate this source of scatter may be a limiting factor if left uncontrolled.

5. Decrease our dependence on timely availability of NASA technology.

2   INTRODUCTION

The research activity described here is part of our larger effort to precision-model the end-to-end (fore-optic telescope through internal starlight suppression systems to detector) optical system performance for space-based coronagraph systems. Precision models are obtained using the analysis tools of geometric optics, E & M vector-wave propagation, diffraction, and statistical optics (coherence theory), along with materials science characterization, vibration-mitigation analysis, and testbed metrology.

This report summarizes the research activities carried out at the College of Optical Sciences of the University of Arizona on the role of optical system polarization in the detection and characterization of exoplanets at optical wavelengths. This analysis was performed using a unique, highly capable computer program, Polaris-M, which performs both geometric and polarization (vector) aberration raytracing. This software is written on a Mathematica platform and enables a unique understanding of the scope of polarization aberrations in telescope-coronagraph systems that function in broadband, incoherent thermal radiation characteristic of light from stars and their exoplanets.

Additional analysis was performed using Fraunhofer and Fresnel diffraction theory with FRED design software in a discussion of large-aperture segmented-mirror topology, and its effects on terrestrial exoplanet characterization.

Polarization aberration analysis[1] is performed on optical systems that have been designed for conditions near zero geometric aberrations[2] in order to preserve the polarization state of the source, thus enabling precision photo-polarimetry. In addition high acuity image quality depends on instrument polarization. The highest quality images, like those required for terrestrial exoplanet coronagraphy require balancing and mitigation of polarization polychromatic aberrations.

We were asked to compare our output from Polaris-M with the better-known CODE V computer-aided design (CAD) software in those areas where a comparison is possible. JPL had performed a limited polarization analysis for the WFIRST-CGI,[3] and we agreed to set-up and run this telescope-coronagraph optical system in Polaris-M to compare the outputs of the two codes. A summary of this comparison is given in Section 4, Milestone 1.

We analyzed two optical systems, HabEx[4] and LUVOIR,[5] in detail. The JPL HabEx team delivered a complete end-to-end optical prescription optimized to minimize geometric wavefront aberrations for the telescope through coronagraph to detector system. We analyzed the complete end-to-end HabEx optical system in detail to provide the comprehensive study presented in Section 5, Milestone 2a.

The GSFC LUVOIR team provided the optical prescriptions for two segmented telescope fore-optic systems: 8-meter and 15-meter. These were polarization ray-traced to the telescope focal plane and the results delivered to GSFC. These results are presented in Section 5.2, Milestone 2b. Our team requested the optical design for a coronagraph system designed to operate with the LUVOIR fore-optics from GSFC, but it was not available. Therefore, we polarization analyzed only the fore-optics or telescope optics of LUVOIR system and provided these results to GSFC for their additional processing.

- As a result of our analysis of LUVOIR, we observed that segmenting the primary mirror with hexagonal segments results in an image-plane diffraction pattern that can possibly confuse imaging exoplanets. We developed an alternative segmentation pattern that we call a pinwheel. The pinwheel exhibits advantages in mirror manufacture, test, and assembly. Coronagraph performance and polarization aberrations remain to be analyzed.

- To acquire the needed astronomical measurement, the LUVOIR telescope, as designed, requires these steps: expose for several days, bore-sight roll the telescope, and expose the same field for several days. The pinwheel aperture offers the opportunity to eliminate the bore-sight roll stage and the following exposure, thus doubling the telescope efficiency.

All exoplanet telescope-coronagraph systems use a large primary mirror to collect and focus light from the exoplanet system. These mirrors range in size between ~1.5 meters for the segmented LUVOIR, to 4-m for the HabEx. Large area primary mirrors show changes in the reflectivity across the surface of the mirror, caused in part by form birefringence, which is a physical property of the thin-film metal coating placed on the mirror substrate to obtain high reflectivity. Form birefringence produces spatially dependent polarization reflectivity changes across the mirror surface. Measurements and analysis of this phenomenon were made at the University of Arizona mirror lab of a 3.8-meter astronomical telescope primary. Details of the measurement and data reduction are presented in a PhD dissertation by Dr. Brian Daugherty, supported by this research grant.[6] These measurements yielded a complex (amplitude & phase) digital map, which was then re-scaled and draped over the HabEx 4-m primary in a calculation led by Dr. Jeff Davis to provide an estimate of the contrast that one might achieve in the presence of real-world current technology coatings on the primary. These data provide engineers with processing tolerances for the manufacture of large-aperture primary mirror substrates and coatings planned for use in terrestrial exoplanet coronagraphy.

All telescope-instrument systems imprint their unique signatures onto the image, which may mask important scientific information. Minimizing these signatures will maximize the scientific usefulness of the telescope-instrument system, and in this case will enable direct imaging and spectroscopy of terrestrial exoplanet surfaces and atmospheres.

- **Dynamic signature sources** are those that arise from events that cause time-dependent changes to the end-to-end optical system performance during the long integration times necessary to record signals from the very faint exoplanets. Examples are spacecraft vibration, pointing & control, thermal expansion, contraction of the structure, and time-changing optical contamination and radiation damage. Dynamic signatures are examined in detail elsewhere.[7]

- **Static signature sources** include absorption of light by mirrors, lenses, and filters; diffraction of light by segments and secondary support structure and the edge of the entrance aperture; and polarization aberrations and geometric aberrations and scattered light (specular and small angle). In this report, we will examine three static signature sources: (1) unnecessary optical surfaces, (2) scalar diffraction, and (3) polarization aberration.

- **Both dynamic and static signatures** contribute to degradation in contrast. A perfectly stable observing platform, with no motion induced into the star/planet object is a necessary but not sufficient condition for the system to image a terrestrial exoplanet. Likewise, a

perfect coronagraph that controls unwanted radiation by almost 100% is a necessary, but not sufficient, condition for the system to image a terrestrial exoplanet. Both must be satisfied simultaneously.

- This effort examines static signatures in HabEx and LUVOIR.

C. F. Lillie and J. B. Breckinridge[8] show that for 10-meter class telescopes, the cost impact of adding one additional optical surface is between 100 and 500 million dollars. This calculation includes the cost to increase the aperture to compensate for absorption loss, the cost to fabricate the optical surface, the cost to hold the optic to the needed tolerance, and the labor to manufacture, align and integrate the surface into the optical system.

Adding one additional optical surface means that the tolerances (surface figure and mechanical support and stability) on all of the other surfaces need to increase. The tolerance then becomes more difficult to achieve, and thus more expensive. Consider the example of a diffraction-limited system with four surfaces where the root mean square (rms) geometric wavefront error is the same on each, say 4.5 nm. Then, if a fifth mirror is added to the system, the allowable rms geometric wavefront error on the surfaces and the mechanical stability in terms of tip, tilt, and piston of each of these five mirrors is decreased by 12%. Opto-mechanical tolerances have become tighter and more expensive, if achievable at all. The geometric wavefront errors introduced by adding additional surfaces are corrected in part using adaptive optics (A/O), but not all is recovered.

In addition, the system transmittance is decreased from 0.97^4 to 0.97^5 and the aperture size should be increased to compensate for loss in the SNR. All of this adds cost and adds to the length of the schedule to the program and to the flight mission phase in order to retain the required system requirement.

Improved designs that reduce cost and increase efficiency should be considered during the concept design phase.

Primary threats to success imposed by polarization effects

To discuss this topic, we need a clear definition of success and without a systems analysis approach to lead a technology development program it is difficult to quantify success within the terms of the performance of discreet technologies and how they interact.

Success is the ability of the space optical system to characterize terrestrial exoplanet systems. Characterization can be divided into two areas: 1. Celestial mechanics for the exo-planet system and 2. Physical properties of the planet and its star. Celestial mechanics includes: orbital elements, rotation rate, spin axis inclination, and motion through the galaxy. Physical properties include: atmosphere of the parent star, planet atmospheric content with temperature & pressure profiles and chemistry, surface geography with chemistry & temperature; light scattered or excited by radiation from the parent star. We define success as the ability of a space optical system to record the measurements necessary to retrieve both the celestial mechanics, and the physical properties exoplanetary systems.

Over the past 20 years we have discovered that exoplanet systems become more diverse and numerous the further away from earth they are. But the further away they are the more difficult it is to characterize them successfully based on our technical abilities to build large telescopes and the length of time it takes to integrate on the very faint light from the exoplanet.

Our only contact with exoplanetary systems is through electromagnetic (E&M) radiation. The aspects of E&M that we measure are intensities that carry these signals: spatial (images), wavelength, polarization, time, and radiometry.

Reviewers asked that the threats imposed by polarization on telescope architecture features be discussed in terms of these parameters & trade-offs:

Segmented vs monolithic telescopes,

We presume the reviewers are talking about hexagonally segmented mirrors, which create grating slits across the primary and diffraction grating orders across the image plane. As long as the gap between segments, which is set by the need to safely mechanically deploy the segmented mirror, exceeds about 10,000 wavelengths of light, this is not dominate source of polarization that will affect either instrument contrast or polarization metrology retrieval. Five-mm gaps are common and at 500 nm wavelength, this is 10^6 waves. But, to some very small level the sharp edge of the hex segment will, itself introduce a partially polarized wavefront. But this PI believes this level will be too small to be detectable.

Clearly a monolithic (continuous) aperture is preferred to minimize the unwanted diffraction structure across the image plane which can mask exoplanets. Segmented telescopes are not filled-aperture telescopes.

Polarization aberrations are introduced into the system: 1. when rays intersect surfaces at non-normal incidence 2. When reflections occur from non-isotropic volume metals, 3. When wavefronts pass through dielectric substrates like windows and glass filters, and 4. Diffraction gratings and prisms, for example those used to disperse light for spectral analysis.

Consider two telescopes of the same aperture, F/#, coating (metal and dielectric) processes and optical power on the secondary. And let one primary aperture be monolithic and the other segmented: there is no fundamental difference between the two in the amount of the polarization that appears at the first focus of each. If the mirror coating processes are different because one is segmented and the other is not, then further investigation is required.

Off-axis vs on-axis telescopes,

Normal incidence from an isotropic reflecting surface has minimum polarization aberrations. Polarization aberrations increase with angle-of-incidence angle-of-reflection so a general rule of thumb would be high F/# for the primary. The higher the F/# the longer the mechanical distance between the primary and secondary and the longer the structure. However, this, in general, conflicts with a space-craft structural-control requirement that the distance between the primary and the secondary mirror be short to increase the structural frequency for better spacecraft control.

But the telescope and instrument polarization aberrations need to be optimized together. One cannot isolate the telescope polarization aberrations and those introduced by the instrument. The polarization aberrations of the instrument are designed to compensate for the polarization aberrations of the telescope.

However, the amount of scattered light across the image plane that masks exoplanets is cumulative, increasing with each optical surface in the system. If, in order to meet space-craft mechanical, structural, and packaging needs, more surfaces are needed for one or the other configuration, then an optical system engineering trade-off is needed.

Dilute vs filled aperture telescopes,

Optical/IR coronagraphs are designed to image high contrast objects by rejecting light from a very bright object from that of a very faint close-by exoplanet. However, after starlight suppression, and at the detector for imaging TERRESTRIAL exoplanets, the difference in flux between the unresolved exoplanet and its background is small and therefore of LOW CONTRAST.

Breckinridge, et. al. [9] showed that dilute/sparse aperture telescopes limit the low contrast object space features, such as a terrestrial exoplanet imbedded within the scattered light from a primary star. These authors concluded that for a sparse aperture telescope system designed for low contrast, complicated-scene astronomy and planetary observations, the sparse-aperture fill factor must be very large—at least 30% to enable imaging of 20% contrast scenes, 40% for 10% contrast imagery, and 50% for 5% contrast imagery. Also, for the typical non-redundant configurations they examined, they found that very high full-well levels and long exposure times are required. There is also a tradeoff between fill factor and full-well. If fill factor is reduced then the required full-well must increase to hold a constant signal-to-noise ratio (SNR). The full-well capacity of the detector and the permissible exposure time will exceed reasonable values if the fill factor is too small.

Highly dilute apertures, sometimes called interferometry, have been demonstrated to be useful for positional (astrometric) astronomy and are also used to determine unambiguous orbital mechanics for some of exoplanetary systems[10].

Fringe contrast and thus image plane contrast depends on the polarization content of the interfering beams. Therefore, polarization aberrations will play a role im a systems analysis trade-off between dilute and filled apertures.

Clearly, the more dilute the aperture the more difficult will be image restoration. And thus TERRESTRIAL exoplanet direct imaging will be very difficult, if not impossible using an interferometer.

Therefore, to image an exoplanet for spectroscopy a filled aperture will be the most cost effective, although with large resources, sparse apertures may be a possible solution if filled apertures are impossible. This trade-off remains to be done quantitatively with test beds, although some preliminary work was performed and published in 1987 by Ribak, Roddier, Roddier and Breckinridge[11] (1987)

IR vs Vis diffraction limited telescopes

The wavelength trades (IR vs. Visible) depends on many factors. Clearly if the science measurement objective is to record data that will reveal the atomic nature of the exoplanet atmosphere, then IR cannot be used. Angular resolution is higher in the UV, but the optical mechanical tolerances are more stringent. This discussion depends on the details of "mission success".

3   BACKGROUND

3.1   ROLE OF POLARIZATION IN EXOPLANET SCIENCE

Polarization plays an important role in three aspects of exoplanet characterization: (1) measurement of the intrinsic polarization properties of the source, (2) image quality, and (3) coronagraph contrast. These three are not independent. For example, image quality and coronagraph contrast depend in part on the intrinsic polarization properties of both the source and the instrument.

The physical properties of a planet's atmosphere, surface (solid or liquid), aerosol and dust particle size, and orbital elements can be estimated using polarimetry. These polarimetric measurements are used with theoretical models of planetary system formation to provide insight into planetary system evolution.

Modeling by Stam, Hovenier, and Waters,[12] and measurements reported by Tomasko and Doose,[13] West et al.,[14] and Gehrels, Herman and Owen[15] using data from the imaging photopolarimeters on Pioneers 10 and 11 and the Voyagers suggest that Jupiter-like exoplanets could exhibit degrees of polarization (DoP) as high as 50% at a planetary phase angles near 90°. Stam[16] showed that polarization measurements of the planet's radiation in the presence of light scattered from the parent star reveals the presence of exoplanetary objects, and provides important information on their nature. Since the first report by Berdyugina[17] of the detection of polarized scattered light from an exoplanet (HD 189733b) atmosphere, several theoretical models have been developed. de Kok, Stam, and Karalidi[18] showed that the DoP changes with wavelength across the ultraviolet (UV), visible, and near-infrared(IR) band-passes to reveal the structure of the exoplanet's atmosphere. Recent modeling by Stolker et al.[19] has demonstrated the sensitivity of polarimetry to asymmetric cloud cover. Ginski[20,] has recently directly detected a polarized companion outside a resolved circum-binary disk around CS. Chamaeleonis[20] and Karalidi, Stam, and Hovenier[21] showed that polarization measurements are of value in exoplanet and climate studies. Madhusudhan and Burrows[22] and Fluri and Berdyugina[23] showed that orbital parameters (inclination, position angle of the ascending node, and eccentricity) could be retrieved from precision polarimetric measurements. Graham, Kalas, and Matthews[24] have shown that a polarization signature of primordial grain growth within the AU Microscopii debris disk provides clues to planetary formation. Perrin et. al.[25] shows that imaging polarimetry provides important constraints for the analysis of circumstellar disks.

3.2   PHYSICAL OPTICS BACKGROUND

Two physical optics phenomena associated with image formation contribute to modify the incident vector complex electromagnetic field, and degrade image quality. These are both caused by the interaction of light and matter: **polarization** induced by mirrors, windows, and stops and **diffraction** produced by masks and stops. Here we report on the effects of polarization introduced by the vector electromagnetic wave (light) reflecting from dielectric and metal reflecting surfaces and absorption. These cause both amplitude and phase changes across wavefronts to affect image quality.

The three-dimensional electric field from exoplanets is thermal white-light broadband, either reflected from the planetary system's parent star, emission from the planet, or a mixture of both. The electric fields associated with the star and the planet are both spatially and spectrally incoherent[26,27,28] at the source. This radiation travels through space, enters the telescope-coronagraph system, and reflects from several mirrors to strike the stop at an image plane. The field is partially coherent at this stop. The coronagraph occulting mask is located at this image-plane stop. The occulting mask must block almost all of the incident electric field from the star while passing through as much as possible of the exoplanet field. The light then passes a Lyot (pupil) stop at an image of the entrance pupil and reflects off the surfaces of several mirrors to the focal plane. By the time this complex field reaches the focal plane, it is partially coherent. The detector records the modulus squared of this complex electric field. An accurate model of this intensity distribution requires a complex vector representation of the electromagnetic field as it passes through the optical system.

This intensity distribution, recorded by the detector, contains information about the characteristics of the exoplanet as viewed through the "filter" of the wavelength-dependent telescope-coronagraph complex-vector transfer function.

3.3   DIFFRACTION POINT-SPREAD FUNCTION: DEFINITION AND IMPORTANCE

The point-spread function (PSF) is defined as the two-dimensional intensity as a function of position across the image plane for a point source (star) in object space. In electrical engineering terms, it is the system impulse response. In optical science terms, it provides the spatial frequency impulse response of the optical system. The PSF carries information on the angular resolution of the telescope-instrument system.

The role of polarization in image formation has been studied for many years.[29,30] We can understand the important role of polarization to image formation by considering the following qualitative example:

A thought experiment using linear orthogonal polarizers and a telescope shows the role of vector waves in image formation and the effects of polarization on contrast. **Figure 3-1** shows the effects of adding unwanted polarizers to an optical system that has zero geometric wavefront aberration: Top left shows an open, unmasked exit pupil of a telescope. Top right shows the shape of the PSF recorded with the perfect telescope aperture on the top left. Bottom left shows the same telescope pupil as that shown in the upper left, but with two linear polarizers over the top; one aligned orthogonally to the other. Horizontally polarized light is admitted to the top half of the pupil and vertically polarized light is admitted to the lower half of the pupil. The bottom right shows the PSF recorded using the pupil on the bottom left. Note that with no polarizer (top
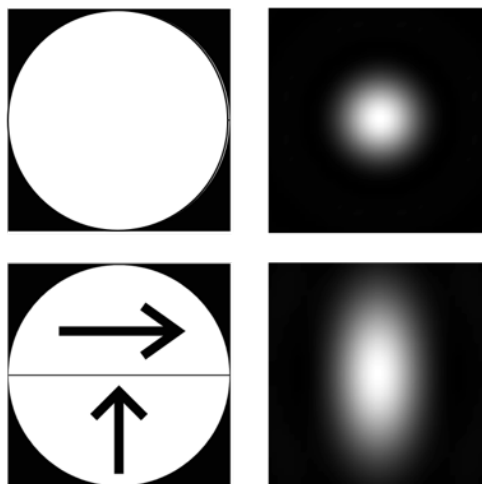
Figure 3-1: PSFs shown for a telescope with zero geometric wavefront aberration without (upper) and with (lower) polarizers. The shape of the PSF changes, and thus the shape of the occulting mask at the image plane needed to attenuate the radiation changes.

row), the angular resolution is not position-angle dependent; however, with the polarizers (bottom row), the angular resolution is position-angle dependent. Astronomers define position angle as the rotation angle in the plane of the sky, or in this case, the plane of object space. That is, the upper right image in **Figure 3-1** shows that the angular resolution is the same in all directions from the axis, whereas the lower right image in **Figure 3-1** shows that the angular resolution is not the same for all angles from the system axis. Angular resolution in the horizontal direction exceeds that in the vertical direction for the PSF shown in the lower right.

Why does this happen? Orthogonally polarized white light does not interfere to create a fringe which is a small element of an image. In **Figure 3-1**, the lower left image of the exit pupil, the polarized radiation from the lower or bottom portion of the exit pupil does not interfere with the orthogonally polarized radiation from the top or upper portion of the exit pupil. Therefore, the PSF is elongated in the vertical direction. In this case the PSF is the scalar sum (linear superposition) of two images of the sidewise "D" shaped aperture, not the vector sum across the circular aperture shown in the upper right panel in **Figure 3-1**. The radiation that is incoherent, that is does NOT interfere creates background light or "noise". The inner working angle is smaller in the horizontal direction than it is for the vertical direction. This means that a coronagraph mask positioned at the image plane that is designed using scalar theory and applied to a system with polarization aberrations would leak large amounts of light around the occulting mask to flood the coronagraph and block light from exoplanets. This may reduce exoplanet yield to the level of uselessness.

This is a rather dramatic example, and no one would intentionally place orthogonal linear polarizers over their telescope pupil. However, this does show that any source of polarization change across the exit pupil will result in distortion of the PSF at some level and result in light leakage around those occulting masks that are designed using scalar theory only.

To maximize transmittance and contrast, and to maximize SNR, the coronagraph mask and the Lyot filter need to pair-wise "impedance" match the complex amplitude (amplitude and phase) electromagnetic field from the star-planet system. The telescope collects the electric field from the star-exoplanet pair. The telescope focuses (concentrates) the radiation onto an occulting mask. The process of focusing or concentrating this electric field not only changes the dimensions of the field, but also alters the field strength and changes or distorts the polarization content of the radiation. An optimized occulting mask, required to observe terrestrial exoplanets, is needed for maximum absorption of the light from the star and maximum transmission of terrestrial exoplanet light.

3.4   PHYSICAL SOURCE OF POLARIZATION ABERRATIONS

The source of polarization in telescope-coronagraph systems is the metal thin films coated on curved and flat optically figured mirrors with transparent dielectric over-coatings. In our initial treatment, we assume that all metal thin films are perfectly isotropic. Other sources include windows, colored glass filters, and dichroics. In Section 7, below we show that large-aperture thin films, in general are not isotropic and that this anisotropy exhibits itself by changing the shape of the PSF to reduce contrast.

A-J Fresnel in 1823 described the theory for interactions of electromagnetic radiation with dielectrics and metals. These relationships were developed further[31] and are, today the basis of the large commercial industry of ellipsometry.[32]

Figure 3-2 defines the commonly used coordinate system. In **Figure 3-2**, incoming incoherent white-light is shown decomposed into two polarization co-propagating states: s and p. These co-propagating orthogonal polarization states reflect from a metal thin film at angle θ_0 from the normal. A portion of the incident light penetrates into the metal at angle θ_1 to the normal and is absorbed a few nm beneath the surface. Light reflects at angle θ_0 from the normal, in the plane of incidence (by Snell's law). The

Figure 3-2: Light is incident from the upper left onto a metal mirror and reflects to the upper right.

absorption is not the same for light polarized in the p-direction as it is for light polarized in the s-direction. The phase of one of the two co-propagating waves is retarded by angle ψ relative to the other. Thus, the reflected starlight is co-propagating and partially polarized, as shown in **Figure 3-2**.

For light incident at angle θ_0, onto a metal mirror, which has a wavelength-dependent complex index, $N_1(\lambda) = n_1(\lambda) + ik_1(\lambda)$; the Eigenstates of reflection are the s- and p-polarized components. A portion of the beam reflects at the incidence angle θ_0 (Snell's law) and another portion (the damped evanescent wave) penetrates a short distance into the metal at the complex refraction angle of θ_1 given by Snell's law[33] and is absorbed to heat the metal. The angle the beam penetrates into the metal θ is given by: $\theta_1 = \arccos\left\{ \left(\sqrt{N_1^2 - N_0^2 \sin\theta_0^2} \right) / N_1 \right\}$

The complex reflectivities for light in the p and s polarizations are given by $r_p = \tan(\theta_0 - \theta_1)/\tan(\theta_0 + \theta_1)$ and $r_s = -\sin(\theta_0 - \theta_1)/\sin(\theta_0 + \theta_1)$. Two polarization effects occur: 1) There is a phase shift between the reflected waves associated with each of the two polarizations. We use ψ, called retardance, which is given by $\tan\psi = \tan(\phi_s - \phi_p) = |r_s|/|r_p|$. 2) The amplitudes of the electromagnetic waves for the s and the p wave decrease upon reflection. The phase change is not the same for both the p and the s wave. Absorption is polarization dependent and therefore the amplitudes of the respective waves are not the same.

The intensity reflectivity is polarization dependent, with the result that reflection acts as a partial polarizer with the diattenuation, $D = \left\{ |r_s|^2 - |r_p|^2 \right\} / \left\{ |r_s|^2 + |r_p|^2 \right\}$ where r is **complex** reflectivity. Metallic reflection acts as a weak polarizer, and D varies from zero (nonpolarizing) to one for ideal polarizers.

Where does mirror reflection occur?

Based on physical optics, not geometrical optics, reflection of light from a metal surface takes place at a small depth below that surface,[34] which is defined by the air-solid material interface. The intensity of a normally incident plane wave onto anisotropic conductor drops exponentially with penetration distance d from the air-material interface into an isotropic conductor. The relationship is given by

$$I(d) = \exp\left[\frac{-4\pi k d}{\lambda}\right],$$

where k is the imaginary part of the complex index of refraction of the metal, d is depth, and λ is the wavelength of light. For aluminum at 500 nm wavelength, we find $d \simeq 6.8 \cdot 10^{-9} m$, or 6,800 pm. By the time the 500 nm light has penetrated ~6.8 nanometers into the isotropic metal (aluminum), the light is reflecting back. This depth is often referred to as skin depth in microwave antenna theory and radio science. The location of the skin depth depends on the porosity of the thin metal film.[35] The contents of Ch 7 in this document presents laboratory measurements of a 3.75-m mirror, the discovery of form birefringence across this typical mirror and a discussion of the effects on contrast of this anisotropic coating phenomenon

If the optical wave enters into the metal at non-normal incidence, the reflected and transmitted (if any) optical waves are polarized and the complex electric fields are given by the Fresnel equations.[36] Others[37,38] have examined in detail the role of vector-waves in the performance assessment and image quality analysis of terrestrial exoplanet telescope-coronagraph systems that use **perfectly isotropic** conducting metal mirrors coated or deposited on an optical substrate (glass, fused silica, ZERODUR, etc.). Shaklan and Green (2006) report that to achieve 10^{-10} contrast, the wavefront error cannot exceed 10 to 100 pm on the reflected wavefront. Therefore, the variation of porosity of the thin film cannot exceed one part in ~200 over an entire 1- to 4-meter primary mirror aperture area. This provides an optical system requirement on allowable thin film anisotropy if one were to achieve 10^{-10} contrast in the manner shown by Shaklan and Green.

3.5   IMAGE FORMATION IN POLARIZED LIGHT

The polarization aberration of an optical system is described by a spatially varying (across the exit pupil) Jones matrix for the ray paths, called the Jones pupil. We write this shorthand for the complex field after reflection:

<div align="right">**Equation 3-1**</div>

On the left-hand side (LHS) of **Equation 3-1**, $A_{XX}(x, y)$ is amplitude at point x, y on the surface, and $\phi_{XX}(x, y)$ is phase at point x, y for each of the four component waves in an arbitrarily selected X,Y basis. Subscript XX refers to the complex field exiting polarized in X resulting from the incident field with X polarization, as matrix multiplication would imply. Subscript YY refers to the complex field exiting polarized in Y resulting from the incident field with Y polarization, as matrix multiplication would imply. This convention extends to the subscripts YX and XY, where XY and YX are called cross-product terms. Ideally, the Jones pupil would be the identity matrix for

all ray paths and no undesired polarization change would occur.[39] During image formation with incoherent light, none of these four Jones pupil components form interference fringes with each other.[40,41] Each is diffracted independently, and we use scalar diffraction theory to calculate each of the four components of the amplitude response matrix, which is the generalization of the amplitude response function of diffraction theory.[42]

The telescope-coronagraph system complex transmittance across the exit pupil is vector dependent. The complex electric field at the image plane $u_3(x,y)$, for an on-axis star of unit brightness is given by:

$$u_3(x,y) =$$
$$u_3(x,y)_{XX} + u_3(x,y)_{YY} + u_3(x,y)_{XY} + u_3(x,y)_{YX} =$$
$$K\left\{ \int_{-\infty}^{+\infty}\int_{-\infty}^{+\infty} \begin{bmatrix} J_{XX} & J_{YX} \\ J_{XY} & J_{YY} \end{bmatrix} \exp\left(-\frac{2\pi}{\lambda f}(x_3\xi_2 + y_3\eta_2)\right) \right\}$$

Equation 3-2

where K is a constant, and we assume that the optical power of the system is not vector (polarization) dependent. Under the conditions of white-light, incoherent image formation from either unpolarized or polarized thermal sources, the image plane intensity is the sum of these four point-spread function components $I_{XX} + I_{XY} + I_{YX} + I_{YY}$.

Details on the role of polarization in image formation for exoplanet science is given in Breckinridge, Lam, and Chipman;[43] Chipman, Lam, and Breckinridge;[44] Davis, Kupinski, Chipman, and Breckinridge;[45] and Breckinridge, Kupinski, Davis, Daugherty, and Chipman.[46] Techniques to mitigate these polarization aberrations are presented in Clark and Breckinridge[47] and Lam and Chipman.[48]

3.6   POLARIZATION REFLECTIVITY ANISOTROPY—FORM BIREFRINGENCE

Krist, et al. (2019)[49] calculate that the 10^{-10} contrast level, needed for terrestrial exoplanets, cannot deviate by more than ~20 picometers, which is 0.3% of the optical depth (6,800 pm) of the wave incident on an aluminized mirror.

All large area metal thin films[50] are deposited with spatially varying density due to the non-uniform, statistical growth of a columnar microstructure. This causes spatial variations in the complex refractive index[51,52] across the face of the film. Complex (amplitude and phase) reflectivity variations across the surface of the wavefront, which are caused by these thin-film non-uniformities, affects coronagraph contrast.[53] Geometric aberrations are polarization independent.

Polarization aberrations depend on the polarization state of the wavefront. They are co-propagating, separable only by inserting polarizers and additional light-absorbing mirrors. The polarization aberrations are unlike the typical geometric aberration, which could be corrected using

an ideal A/O subsystem. Geometric and polarization optical path difference changes across the beam contribute to speckle around the PSF.[54]

A large area mirror substrate could be fabricated to a required surface accuracy of $\lambda/1000$ rms but the white-light reflected wavefront appear distorted by $\lambda/100$ because of thin-film irregularities. Polaris-M uses these fabrication irregularities to compute detailed structure in the PSF, which may affect exoplanet measurements. The value of making a measurement of the form birefringence and how birefringence affects HabEx performance is assessed in Section 5.

3.7   POLARIZATION RAY TRACING (PRT)

Polarization ray tracing (PRT) is a technique for calculating the polarization matrices for ray paths through optical systems.[55,56,57,58,59,60] Polaris-M[61] was built from the ground up to calculate polarization effects in optical systems. It is based on a 3x3 polarization ray-tracing calculus.[49] Diffraction image formation of polarization aberration (PolAb) beams is then handled by vector extensions to diffraction theory.[62,63,64,65] The polarization point-spread matrix and the optical transfer matrix are described in detail in the 2019 book by Chipman, Lam, and Young, *Polarized Light and Optical Systems*, from CRC Press.

3.8   POLARIZATION ABERRATION THEORY (POLABT)

Polarization aberration theory (PolAbT) describes the polarization effects of diattenuation, retardance, and apodization in a series expansion. A cascade of terms separate mathematically the largest effects from smaller effects, and associate these polarization-related image defects with constructional parameters and coating performance metrics.[66,67] For example, the term "retardance tilt" is strongly associated with fold mirrors and causes the XX and YY image components to shift with respect to each other, making the PSF slightly elliptical. The term "retardance-defocus" causes astigmatism from primary and secondary mirrors, which is polarization dependent. The orientation of the retardance rotates with the orientation of an incident linear polarization.[68]

PRT generates very large files of numbers, at least eight times more than a conventional ray trace, leaving the designer with managing a substantial data interpretation task of the aberrations represented in a higher dimensional polarization space. PolAbT is more difficult analytically than PRT, but it simplifies the ray-tracing results into a small number of terms, which are understood and addressed in an uncoupled manner. This enables us to manage polarization aberrations in more complex systems.

A distinction between the two is seen in the comparison between classical geometric aberration ray trace (analogue to PRT) and the structural aberration coefficients[69] (analogue to PolAbT) used by advanced designers to arrive quickly at near-optimized designs. Thus, using PolAbT together with PRT is far more powerful than using either method alone.

3.9   POLARIS-M POLARIZATION ANALYSIS MODELING SOFTWARE

Most commercial optical design and analysis software has at least some polarization modeling capability. A few software packages model the polarization effects of standard thin-film

coatings, but little else. Some software has the ability to trace birefringent materials either approximately or accurately. Many commercial software products claim wide-ranging capabilities, but do not state how the computations are done and which algorithms are used, leading to questions about accuracy. Accuracy is particularly important for all telescope-coronagraph systems, if we are to demonstrate the control of unwanted radiation with high certainty to levels of 1 part in 10^{10} or better in order to characterize terrestrial exoplanets.

Polaris-M is an optical analysis program that specializes in sophisticated polarization modeling. The core program and many of its modules are written in Mathematica. It includes standard features such as polarization from metal and dielectric surface coatings, and realistic models of the on- and off-axis characteristics of dielectric stacks on metals and crystal polarizers. In addition, it provides accurate modeling of thin-film coatings on birefringent elements and delivers accurate modeling of spatially varying birefringent elements and metal mirrors. The software has the ability to use spatially or angularly resolved measured polarization data, and many other features. For modeling the WFIRST system, these capabilities will allow us to accurately calculate the system polarization effects on system transmittance, mask design and engineering, and image quality in addition to a full polarization aberration analysis including chromatic aberrations. Polaris-M's unique capability is to provide output data and intermediate surface maps of value for the optical scientist to correct and manipulate polarization aberrations and control system transmittance.

3.10   HOW POLARIS-M WORKS

The output of a CAD ray-trace computer program is combined with Fourier optics to calculate point-spread functions and system contrast. **Figure 3-3** shows a side view of a typical optical system with a fan of rays originating from a point on the object and passing through an optical system with k surfaces to the system exit pupil. Each ray strikes a real physical surface at a known angle of incidence (no paraxial approximation). The program is written in Mathematica and is implemented in a global coordinate system, which simplifies the understanding of system polarization.
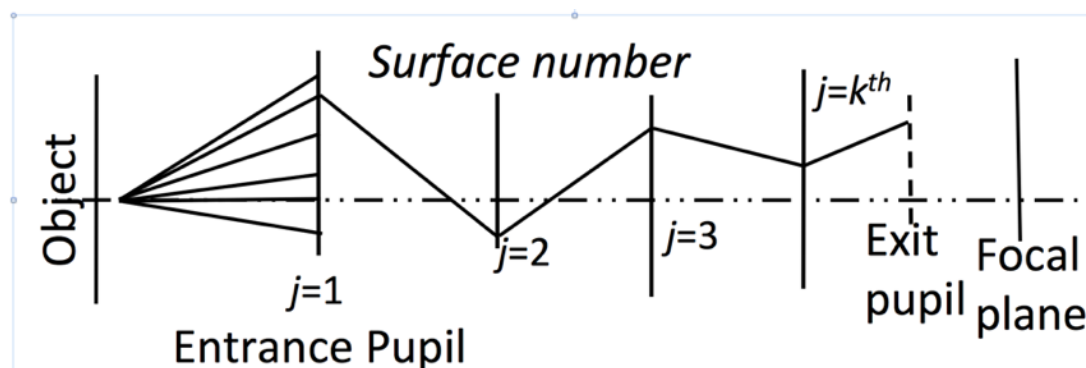
Figure 3-3: A fan of rays is shown passing from the object plane through an optical system with k surfaces before the exit pupil. For descriptive purposes, a fan of rays is shown traced to surface number j=1 and then a general single ray continues on to the exit pupil at surface number j=k+1. The focal plane is at surface j=k+2.

We know the physical and material properties of each surface. Each surface in an optical system is either a reflecting metal or a dielectric. Using the Fresnel equations, we calculate values for each of the four complex entries in **Equation 3-2**, for each ray intercept through the system. We

compute the multiplicative amplitude and cumulative phases for both perpendicular and parallel light and map these point by point (x,y) into four arrays of complex numbers across the exit pupil. We then take a digital fast Fourier transform (FFT) of each set of these four arrays of complex-field points to calculate the four PSFs at the image plane. In the case of a Lyot coronagraph, these four PSFs are superposed onto the occulting mask. The complex occulting mask operates on these four fields to block light from the star and pass radiation from the exoplanet to a spectrometer or imaging system that records, using a charge-coupled device (CCD) for example, the modulus squared of the four electromagnetic fields.

3.11   ACTIVITIES

The input required for detailed polarization analysis is a diffraction-limited geometric ray-trace model of the optical prescription with minimum geometrical aberration. The correct optical surface separations, surface shapes, indices, tilts, angles, and coatings are needed for input to Polaris-M. We converted the NASA/JPL provided 5 Sept 2017 version of the end-to-end optimized optical prescription for HabEx into the University of Arizona Polaris-M polarization ray-trace code. This provides a numerical model of the propagation of phase and amplitude through an engineered system. We developed a vector-wave model of HabEx and calculated the effects of the telescope-instrument polarization on image quality and thus contrast. We use this vector-wave model to determine the effects of each surface and device separately as well as cumulatively.

We combine the optical design tools of geometric ray-trace, diffraction theory, Fourier optics, vector-waves (polarization), and the interactions between light and matter to predict the performance of terrestrial exoplanet optical systems and to develop optical engineering strategies to maximize their performance. In the next three sections (4, 5, and 6), we review the three milestones for this contract and describe our results in detail. In Section 7, Dr. Daugherty describes how he measured and interpreted the data to determine the form birefringence for a 3.75-m aperture aluminized spherical mirror. In Appendix B, we report additional discoveries.

4   MILESTONE 1: COMPARE POLARIS-M WITH CODE V USING WFIRST-CGI

4.1   INTRODUCTION

The WFIRST space flight system incorporates a technology demonstration of an exoplanet coronagraph. The name of the instrument is abbreviated as CGI for coronagraph instrument. The polarization properties of CGI were calculated by JPL engineers using the commercially available general-purpose ray-trace code, CODE V. These data were made available to this research task for the purpose of comparing the Polaris-M polarization results with those generated by CODE V.

4.2   BACKGROUND

Polaris-M polarization ray-trace code has not been used to model spaceflight optical systems. It is a code new to NASA aerospace engineers. The commercial optical design software CODE V was used to design, specify, and tolerance the WFIRST-CGI spaceflight optical system. CODE V, which is a design and optimization code, is not usually used to analyze the polarization properties of optical systems. Although it does have that capability, it is not the most efficient. JPL used CODE V to analyze the polarization performance of WFIRST-CGI from the primary mirror to the exit pupil as viewed looking toward object space from the occulting-mask image plane. CODE V is a design program that is primarily used to vary curvatures and separations of optical elements to optimize opto-mechanical layout designs to minimize geometric (ray-path length) errors.

CODE V performs its optical system ray trace in the local coordinate system of the Poynting vector. This is useful for modeling geometric aberrations and to represent wavefront errors introduced by surface deformations and refractive index variations within the transmissive solids used for filters and windows. Polaris-M performs its ray trace in a global coordinate system to account for how the polarization state changes upon reflection from each surface in the three-dimensional space of the folded and packaged optical system. The global coordinate system is much simpler for polarization calculations.

At the James C. Wyant College of Optical Sciences we used Polaris-M and analyzed the polarization performance of WFIRST-CGI from the primary mirror to the exit pupil associated with the occulting mask. Polaris-M is an analysis program, which accepts an opto-mechanical layout with separations, curvatures, and coatings specified and calculates the polarization aberrations in a global coordinate system.

We converted the CODE V optical prescription into Polaris-M. The results of these two independent computations, one using CODE V and the other using Polaris-M, are described, and results compared in Section 4.3.

4.3   COMPARISON OF CODE V AND POLARIS-M ANALYSES OF WFIRST-CGI

Ray intercepts and angles on surfaces (curved or flat) in the optical system calculated by CODE V should be identical to those obtained by running Polaris-M. **Table 4-1** identifies the 20 optical surfaces from the primary mirror to the mirror just in front of the occulting-mask image

plane for WFIRST-CGI. A table containing the ray intercept heights for the CODE V run was compared to the ray intercept heights calculated by Polaris-M. Column one is the descriptive name of the surface, and columns two, three, and four are the ray intercept height differences (CODE V minus Polaris-M) ΔX, ΔY, and ΔZ, respectively, on each surface in units of mm. Data in the table show that the ray intercepts differ by less than 3×10^{-7} mm. The two ray-trace codes have therefore been shown to deliver the same geometric answer to within a very small "rounding" error.

Ray intercepts differences between CODE V and Polaris-M appear to grow systematically with mirror-count number. **Figure 4-1** shows the CODE V – Polaris-M intercept point differences as a function of mirror count, in order of ray propagation from the WFIRST primary mirror to the final mirror before the occulting mask in CGI.

Table 4-1: Shows that there is no significant difference between the CODE V and the Polaris-M ray-trace values. Data in the table show that the ray intercepts differ by less than 4×10^{-7} mm, well within the rounding errors of the computation and much less than the 3% value required in Milestone 1.

Ray Intercept Difference, CODE V – Polaris-M	ΔX (mm)	ΔY (mm)	ΔZ (mm)
Primary (1)	-1.4E-08	-6.0E-09	2.3E-09
Secondary (2)	-1.4E-08	-6.0E-09	2.1E-09
COR F1, Flat (3)	-7.7E-08	-3.3E-08	1.2E.08
COR F2, Flat (4)	-7.8E-08	-1.7E-08	3.3E-08
M3, Conic (5)	-1.1E-07	-8.3E-09	4.7E-08
COL F1, Flat (6)	2.7E-08	1.2E-09	-1.2E-08
M4, Conic (7)	9.4E-08	1.1E-09	-4.1E-08
COL F2, Flat (8)	3.8E-08	8.0E-09	-1.6E-08
FSM (9)	-4.7E-08	-1.1E-08	2.2E-08
R1 OAP1 (10)	-1.6E-07	1.2E-08	7.6E-08
Focusing Mirror, Flat (11)	-1.5E-07	1.6E-08	6.9E-08
R1 OAP2 (12)	-1.5E-07	2.0E-08	6.7E-08
DM1 (13)	-1.9E-09	2.4E-10	-4.7E-10
DM2 (14)	2.5E-07	1.4E-08	-1.1E-07
R2 OAP1 (15)	3.3E-07	2.5E-08	-1.5E-07
FM, Flat (16)	3.0E-07	6.5E-09	-1.3E-07
R2 OAP2 (17)	2.3E-07	-7.1E-09	-1.0E-07
SP-Mask/HLC_FM, Flat (18)	-2.6E-10	-3.5E-11	7.2E-10
R3 OAP1 (19)	-3.0E-07	1.0E-08	1.3E-07
FPM (20)	-3.8E-07	4.9E-09	1.7E-07
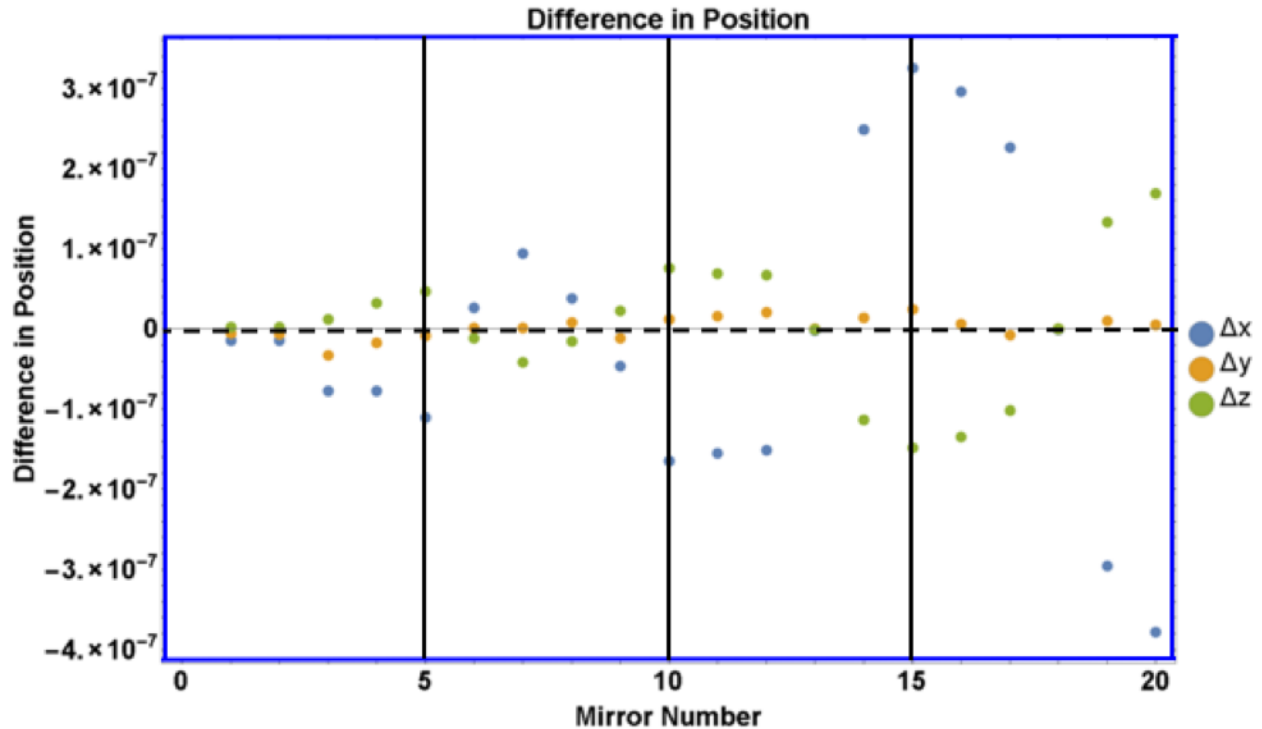
Figure 4-1: Difference in position as a function of mirror count for CODE V minus Polaris M calculated ray intercepts for the first 20 optical elements in WFIRST-CGI. The difference grows systematically from < 1x10-7 mm for the first 10 reflections expanding to <4x10-7 mm at the 20th mirror. This growth is insignificant.

From **Figure 4-1**, we conclude that the Polaris-M geometrical ray trace through the WFIRST-CGI system is very close to the geometrical ray trace through the same system.

Milestone 1 referenced the WFIRST design and requested that we validate the WFIRST CAD ray trace using Polaris-M software. Milestone 1 included no coronagraph design, and therefore our optical design work terminated at the focal plane of the WFIRST-CGI system fore-optics. This is stated in our report. These differences probably depend on the hardware platform the software in running on and not related to the software. However, further investigation is needed.

There is a clear need for calculations of the expected effect of ray intercept errors on coronagraph contrast for future actual optical designs, including build tolerances, alignment tolerances, and environmental effects. However, the calculation of contrast was not part of any of the Milestones. The sensitivity of contrast to "typical" opto-mechanical deformations driven by fabrication, alignment, and environment effects should be part of the design effort as part of the PDR to accept the design. Detailed tolerancing efforts are usually performed as part of the detailed opto-mechanical tolerancing performed as part of the optical system flight build after the Critical Design Review (CDR).

The milestone as written and accepted by both the technology office and the WFIRST-CGI project office did not include calculation of system contrast in the presence of polarization aberrations. We requested the optical prescription for the WFIRST-CGI coronagraph so we could polarization ray-trace the entire end-to-end optical system and report a contrast value for the polarization aberrated system, but none was provided. Therefore Milestone # 1 was successfully completed as agreed to by both the technology program and the WFIRST-CGI project.
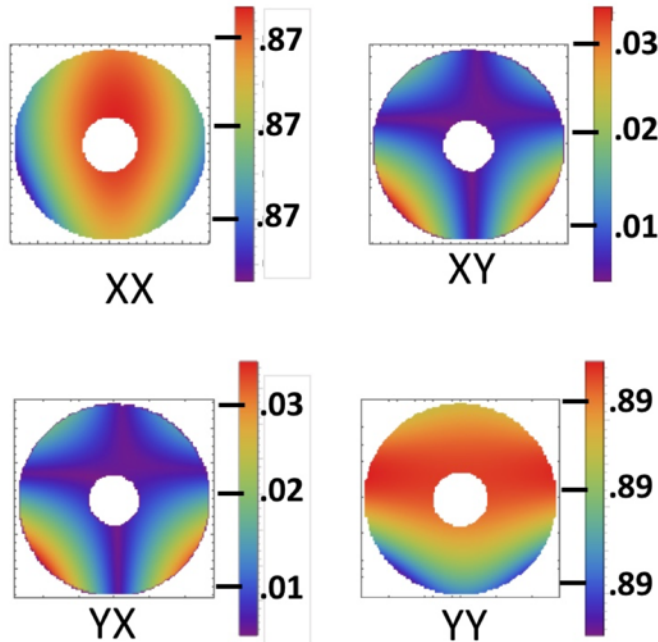
Figure 4-2: Shows the cumulative amplitude part of the Jones pupil for the first 20 optical elements in WFIRST-CGI Cassegrain telescope system.

Figure 4-3: Shows the phase part of the Jones pupil for the first 20 optical elements in WFIRST-CGI.

4.4   POLARIS-M JONES PUPIL FOR WFIRST-CGI

The Jones pupil for the occulting-mask image plane is shown in **Figure 4-2** (for the amplitude terms) and in **Figure 4-3** (for the phase terms).

In **Figure 4-2** upper left, we see a map across the exit pupil of the amplitude reflectivity for X polarized light in and X polarized light out. The amplitude reflectivity is found to be almost uniform after 20 reflections at 0.87. The intensity transmittance is found by squaring this to give 75%. In the lower right of this same figure, we see a map across the exit pupil of the amplitude reflectivity for Y polarized light in and Y polarized light out. The amplitude reflectivity is found to be almost uniform after 20 reflections at 0.89. The corresponding intensity reflectivity would be 79%. The reflectivity shown for the off-diagonal members of the amplitude part of the Jones pupil are too small (<.03) to cause any significant "noise" signal. The system transmission is calculated assuming ideal thin films that are perfectly isotropic in their polarization reflectivity and show no form birefringence.

The intensity values of 79% and 75% are the theoretically highest value possible intensity reflectivity based on the real and imaginary indices of refraction of the films and their dielectric overcoats. This value would be impossible to achieve in an engineering or manufacturing environment. Astronomical telescope mirror reflectivities of 97.5% per mirror have been reported by the ground-based National Science Foundation (NSF) Gemini Observatory. If each mirror in HabEx were that good, then after 20 reflections, one would expect a 66% total system, not the 77% and 79% values predicted here.

Figure 4-3 in the upper left shows a map of the phase of the Jones pupil across the exit pupil of the WFIRST-CGI in units of waves. Note there is a systematic shift in units of waves of phase across the upper left figure, that is XX in the amount of about 0.1 wave to offset the XX PSF up at the image plane by 0.1 wave. Whereas, the phase map for YY, in the lower right, shows that the centroid is systematically shifted down by about 0.1 wave. PSFs are shifted relative to each other, and the occulting mask at the image plane needs to be manufactured larger than would be needed if the centroid of I_{XX} were super-posed on the centroid of I_{YY}. The system is not quite diffraction limited, and the inner working angle is larger than it would be were the system to be diffraction limited.

4.5   CODE V PSF & POLARIS-M PSF FOR WFIRST-CGI

The point-spread function at the occulting mask was calculated for the radiation after passing across the 20 surfaces in the WFIRST-CGI, before the occulting-mask focal plane, using both CODE V and Polaris-M. Polarization ray-trace programs generate four point-spread functions, one each for a) X light in and X light out, b) X light in Y light out, c) Y light in Y light out, and d) Y light in and X light out. **Figure 4-4** displays the difference between the CODE V calculation of PSF and the Polaris-M calculation in a 2 x 2 matrix format. The center pixel in each of the four panels in Figure 4-4 is shown to be saturated which results from small sampling errors and is not significant.
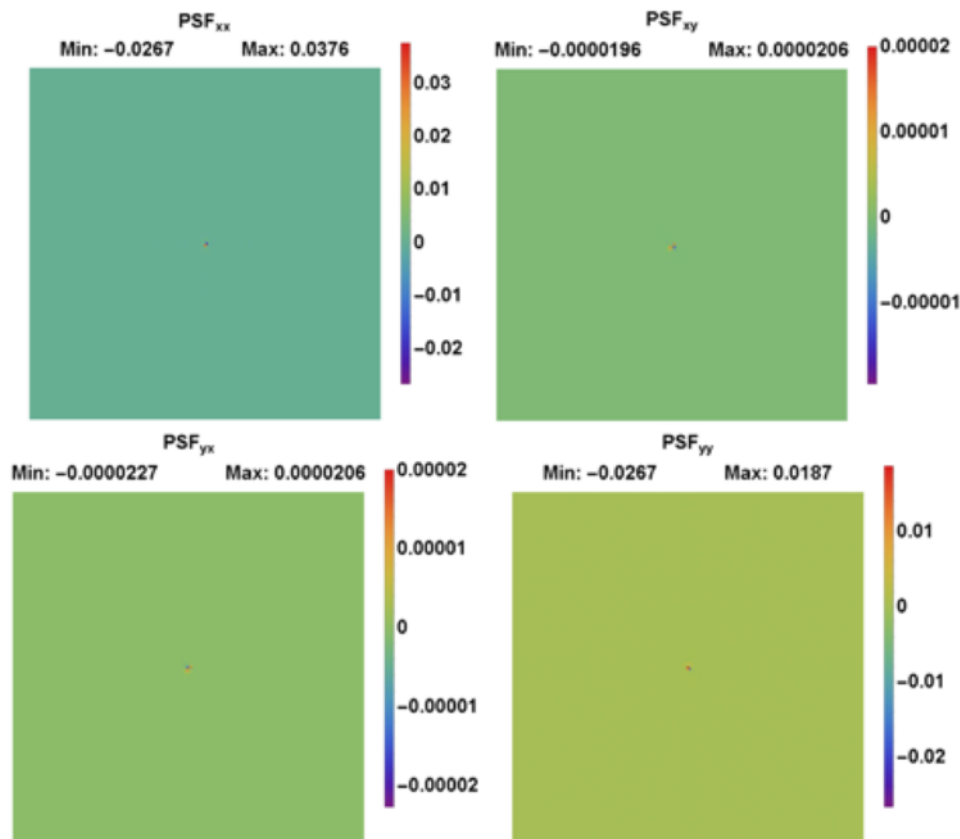
Figure 4-4: PSF calculated using CODE V minus the PSF calculated using Polaris-M for XX (upper left), YY (lower right), YX (lower left), and XY (upper right) showing that results from the two codes agree to better than 1 part in 10^{+3}.

4.6   SUMMARY OF THE WFIRST-CGI POLARIZATION ABERRATIONS & CORONAGRAPH CONTRAST

The optical prescription provided to our team included only the first 20 optical elements before the image-plane occulting mask. There was no information provided on the occulting mask or the optics that follow the occulting mask to image the star/planet onto the focal plane. In addition, there was no information provided on the size of the obscurations or the structure needed to support the secondary. We were unable to take into consideration diffraction caused by obscurations and shadows from these structures, since the Project provided us no information to do so.

Insufficient information was provided to estimate the change in contrast caused by polarization aberrations from either the complex occulting mask or the secondary support structure that casts shadows across the primary mirror. The technology milestone was to show that the polarization aberration calculated by Polaris-M and CODE V agrees with each other for the 20 reflecting surfaces of the WFIRST-CGI fore-optics. The WFIRST-CGI has been designed, up to the occulting mask, with low intrinsic polarization.

In conclusion, the polarization calculated by CODE V is identical to that calculated by Polaris-M. And we can say nothing about contrast calculations.

5   MILESTONE 2: HABEX AND LUVOIR OPTICS

5.1   INTRODUCTION

The optical system for the NASA Habitable Exoplanet Observatory is designed to characterize terrestrial exoplanets using the largest unobscured clear aperture telescope (4-meters) that NASA believes can be manufactured, packaged, and launched over the next decade. The opto-mechanical and thin-film architecture assignment was performed by Stefan Martin[70] of JPL to give a geometric-aberration diffraction-limited performance, and we were assigned the task to polarization ray trace this design to obtain a detailed performance assessment that included polarization and vector-wave propagation analysis.

1.1.1   *HABEX CORONAGRAPH DESIGN PARAMETERS*

Table 5-1 gives the HabEx coronagraph instrument parameters. Column one shows the instrument parameter, column two shows the value for that parameter in the "Blue" channel, column three shows the value for that parameter for the "Red" channel, and column four gives the value of the parameter for the IR channel.

Table 5-1: HabEx Coronagraph Instrument parameters copied from Martin et. al. (2017)[71.]

	"Blue" Channel	**"Red" Channel**	**IR Channel**
FOV	2.3"	2.3"	3.0"
Wavelength Bands	450 nm – 550 nm	672 nm – 821 nm	950 nm – 1800 nm
	550 nm – 672 nm	821 nm – 1000 nm	
Pixel Resolution	11.6 mas	17.3 mas	24.5 mas
Telescope Resolution	23 mas	35 mas	49 mas
IWA (2.5 λ/D)	58 mas	87 mas	123 mas
OWA (as)	0.74	1.11	1.57
Detector (camera)	1x1 CCD97	1x1 CCD97	1x1 LMAPD
Array Width	512	512	256x320
Spectrometer Resolution λ/$\Delta\lambda$	140	140	140
Spectrometer Type	IFS	IFS	Slit
Detector	1/4 CCD282 (EMCCD)	1/4 CCD282 (EMCCD)	1x1 LMAPD
Array Width (pixels)	2048	2048	256x320
Deformable Mirror	64x64 0.4 mm pitch	64x64 0.4 mm pitch	64x64 0.4 mm pitch

1.1.2   *HABEX OPTO-MECHANICAL LAYOUT*

The Zemax optical prescription for HabEx, including the opto-mechanical layout of the packaged flight hardware, was provided on 5 September 2017 along with a description of the mirror coatings.

The optical ray trace design includes no windows or optical filters, which are represented in the design package as surfaces with zero power and no aberrations. The four wavelength bands in the "Blue" and "Red" channels shown in **Table 5-1**, above. are separated using optical dichroic filters. These optical dichroic filters introduce an unknown amount of polarization and wavefront errors into the optical path. No one has ever measured the polarization transmissivity and reflectivity as a function of wavelength for an optical dichroic and therefore there is no data to insert into our models.

The next three figures show the end-to-end optical path for the star and exoplanet light traversing through the telescope fore-optics and through the coronagraph instrument to the detector plane.

Figure 5-1 shows the first four optical elements in the telescope-coronagraph system. Light from the star and exoplanet enter the system from the lower left and reflect from mirror M1, which is the primary. The beam is converging to a focus when it strikes M2, M3, and M4. **Figure 5-2** shows where the light goes after striking the small mirror M4 and continues through M14 of the system. The occulting-mask focal plane (OCMFP) is shown. The function of the two deformable mirrors (DMs) is to create a stable dark hole, using the Talbot effect to image block out unwanted light.

Figure 5-3 shows the 4-reflection optical path after it leaves the occulting mask, passes through a field mask, and an optical colored filter to strike the detector. This is a relay module mirror group that relays the image plane through optical filters after the occulting mask onto the detector.

HabEx is designed to operate at 5 optical wavelengths as shown in **Table 5-1**. These are 450–550 nm, 551–672 nm, 672–821 nm, 821–1000 nm, and 950–1800 nm. We selected the 450 to 550 nm bandwidth to model the polarization properties and image-forming performance of HabEx. Our experience shows that coatings and image quality performance is most stressed at shorter wavelengths.
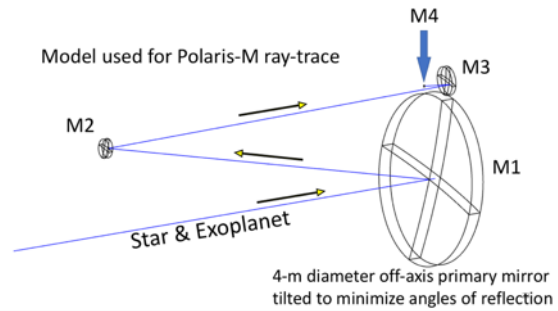
Figure 5-1: The HabEx primary mirror is a 4-meter off-axis asphere that is tilted relative to is to its axis to minimize angles of incidence on the primary and thus minimize the polarization aberrations attributable to the primary. Light reflected from the primary reflects from mirrors M2, M3 and M4. **Figure 5-2** below shows where the light goes after striking the small mirror M4.
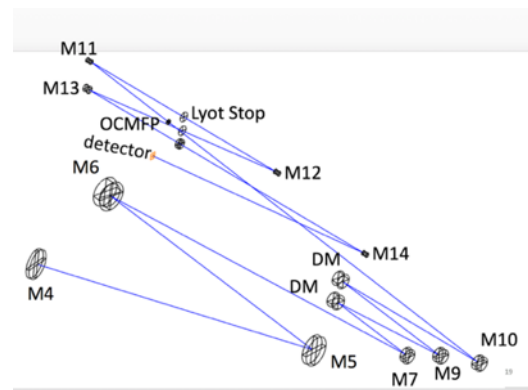
Figure 5-2: The HabEx telescope-coronagraph system is shown from mirror M4 through to the detector.
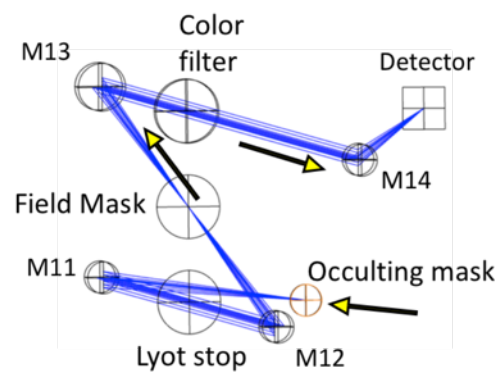
Figure 5-3: Optical path, shown in blue of the light after it leaves the occulting mask, passes through a field mask and an optical colored filter to strike the detector.

1.1.3   *COATINGS ANALYSIS*

The highly reflective metal thin films over the curved mirrors, A/O elements, and flat surfaces have a dielectric overcoat to protect them from oxidation and to maintain high reflectivity during assembly, test, system integration, and the flight operation phase of the mission.

The coating on the first two HabEx mirrors, the 4-meter primary and the secondary, is aluminum (Al) with an overcoat of 25-nm MgF_2. The polarization aberrations for the remaining mirrors in the complete HabEx optical system are calculated here for two coating recipes: A) Al+25nm MgF_2 (that is the same coating as on the primary & secondary) and B) silver (Ag) overcoated with FSS99. We report on the spatial distribution of the diattenuation across the primary mirror and the cumulative diattenuation across the exit pupil to the occulting mask and across the exit pupil to the detector, without the occulting mask in the system. Depending on how the occulting mask is fabricated, the polarization properties of the wavefront at the detector may change significantly from those calculated here. Sections 1.1.4 and 1.1.5 show maps of the diattenuation and the retardance across the wavefront as it propagates through the HabEx optical system.

We also show a detailed polarization map of the PSF, which reveals changes in the vector wavefront content across the PSF. The role these changes make in system contrast and exoplanet characterization is being investigated.

In addition, we present laboratory measurements of the form birefringence across a large (3.75-m) mirror with a "typical" astronomical coating in Section 6. This coating was made following the processes and procedures used at KPNO to coat the 4-meter Mayall telescope as described in Appendix A to this document. Maps showing changes in retardance and changes in diattenuation across the mirror are given in Section 6.

1.1.4   *DIATTENUATION MAPS*

This section shows how the diattenuation changes across the wavefront for a 500 nm wavelength at three different wavefront surfaces within HabEx: (1) the 4-m off-axis, tilted primary mirror, (2) the cumulative wavefront at the exit pupil to the occulting-mask focal plane, and (3) the cumulative wavefront at the exit pupil to the coronagraph detector plane. In all of the diattenuation figures, the orientation of the tick marks across the face of the mirror show the preferred polarization vector direction of the reflected light, and the length of the tick mark shows the magnitude of the diattenuation.

We created diattenuation maps for two sets of coatings at a 500 nm wavelength. We compare, quantitatively, the diattenuation performance of HabEx for two complete sets of highly reflective metal coatings (aluminum and silver) with dielectric overcoats.

Figure 5-4 shows a map of the diattenuation at a 500-nm wavelength across the 4-m HabEx primary mirror coated with Al + 25-nm MgF_2.

Figure 5-5 shows the cumulative diattenuation maps for two coating recipes on the 11 mirrors just before the exit pupil for the occulting mask. The map on the left is for all 11 mirrors coated with aluminum + 25-nm MgF_2, and the map on the right shows the diattenuation calculated under the conditions that mirrors 1 and 2 are coated with Al+25nm and the remaining nine mirrors

to the exit pupil are coated with Ag+FSS99. These maps are important because they provide an indication of the polarization content of the PSF and enable the thin-film engineer to see where on the mirrors the coatings can be changed to optimize the shape of the occulting mask to maximize attenuation. We see that by using the Ag+FSS99 coating, we have reduced the diattenuation by a factor of ~2.

The detector plane exit pupil map of the cumulative diattenuation is calculated assuming there is no occulting mask. The purpose of this section is to show that the image quality at the detector depends on the attenuation properties of both the occulting mask and the mirrors after the occulting mask.
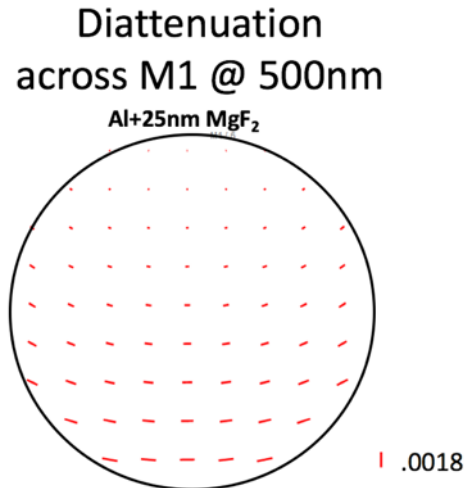
Figure 5-4: Diattenuation map across the primary mirror (M1) of HabEx, calculated at 500 nm wavelength, assuming an ideal, isotropic thin-film reflective coating of evaporated aluminum overcoated with a dielectric of 25 nm thick MgF$_2$. The length of the line in the lower right hand of the figure corresponds to a diattenuation magnitude of 0.0018. The optical axis of the system intercepts the continuation of the surface, just off the top of the mirror. Diattenuation is minimum at the top of the mirror, because the angles of incidence of these rays are almost normal. The lower portion of the mirror is tilted forward in this off-axis optical system. Rays that strike this lower portion reflect at larger angles than do those that reflect from the top portion of the mirror.
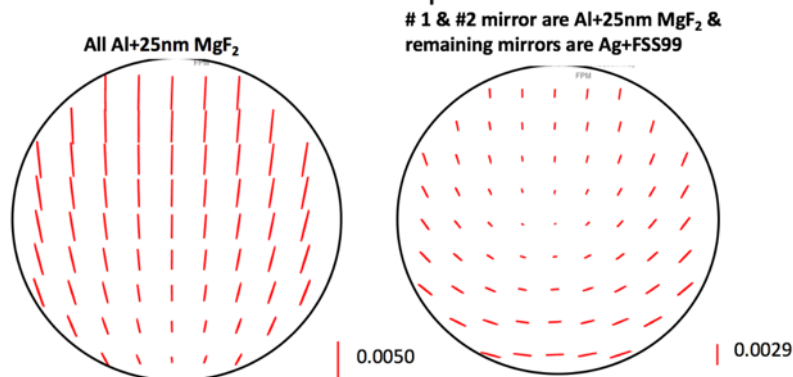
Figure 5-5: Diattenuation map across the last mirror before the coronagraph occulting focal plane mask in HabEx. This was calculated at 500 nm wavelength, assuming an ideal thin-film reflective coating of evaporated aluminum, overcoated with a dielectric of 25 nm thick MgF$_2$ on mirrors 1 and 2. The mirrors between #2 and that mirror just before the focal plane mask are assumed to be coated with silver (Ag) and overcoated with a dielectric of FSS99. The orientation of the tick marks across the face of the mirror show the preferred polarization vector direction of the reflected light, and the length of the tick mark shows the magnitude of the diattenuation. In this case, it is 0.0050 for a system where all mirrors are coated with Al+25nm of MgF$_2$, and the diattenuation is 0.0029 for the case where the first and second mirrors are coated with Al+25nm of MgF$_2$ and the remaining mirrors are coated with Ag+FSS99.

For each ray that is mapped through the optical system by the ray trace program, Polaris-M calculates the diattenuation added by each surface to that ray. The orientation of the tick mark shows the orientation of the vector direction maximum after the ray strikes the surface. And its length is proportional to the magnitude of the diattenuation . This feature of the program is used by optical engineers who use the tilt angles of reflecting surfaces and thin film physics to balance and control system diattenuation. Diattenuation contributed by each surface adds linearly and we show the cumulative calculation in figures 5-4 through 5-6. This analysis tool is used to balance and minimize spatially varying diattenuation in high fidelity (diffraction limited) imaging systems used with radiometric precision.

Cumulative diattenuation at detector across the last mirror before the detector – no occulting mask
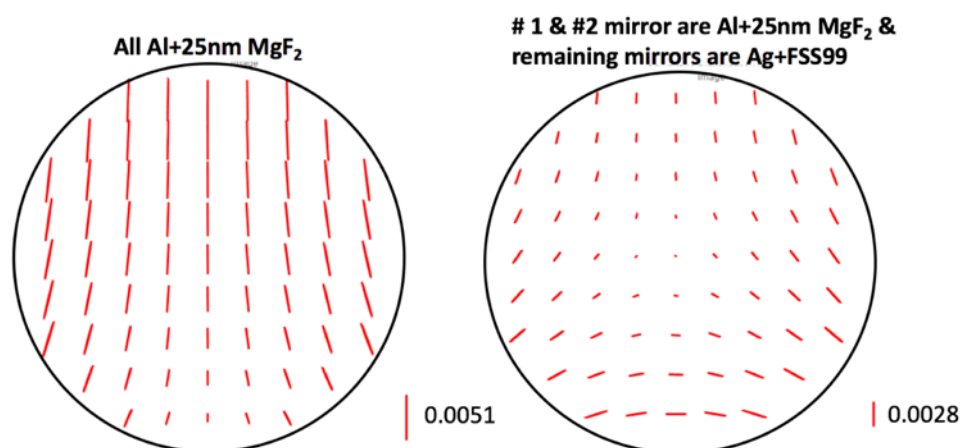
Figure 5-6: Diattenuation map across the last mirror before the detector in HabEx, calculated assuming an ideal transparent occulting mask. The map on the left was calculated at 500 nm wavelength, assuming a thin-film reflective coating of evaporated aluminum, overcoated with a dielectric of 25 nm thick MgF_2 on all mirrors (left image). The mirrors between #2 and that mirror just before the focal plane mask are assumed to be coated with silver (Ag) overcoated with a dielectric of FSS99. The orientation of the tick marks across the face of the mirror show the preferred polarization vector direction of the reflected light, and the length of the tick mark shows the magnitude of the diattenuation. In this case, it is 0.0050 for a system where all mirrors are coated with Al+25nm of MgF_2, and the diattenuation is 0.0029 for the case where the first and second mirrors are coated with Al+25nm of MgF_2 and the remaining mirrors are coated with Ag+FSS99.

1.1.5   RETARDANCE MAPS

This section examines the values of the cumulative retardance across the wavefront at three different surfaces: (1) the 4-m off axis tilted primary mirror, (2) the retardance for the cumulative wavefront at the exit pupil to the occulting mask focal plane, and (3) the retardance for the cumulative wavefront at the exit pupil to the coronagraph detector plane. In all of these retardance maps, the orientation of the tick marks across the face of the mirror or wavefront show the fast axis of the reflected light, and the length of the tick mark shows the magnitude of the retardance.

For each ray that is mapped through the optical system by the ray trace program, Polaris-M calculates the retardance added by each surface to that ray. The orientation of the tick mark shows the orientation of the fast axis direction after the ray strikes the surface. And its length is proportional to the magnitude of the retardance. This feature of the program is used by optical engineers who use the tilt angles of reflecting surfaces and thin film physics to balance and control system retardation. Retardation contributed by each surface adds linearly and we show the cumulative calculation in figures 5-7 through 5-9. This analysis tool is used to balance and minimize spatially varying retardance in high fidelity (diffraction limited) imaging systems used with radiometric precision.

A comparison of the two mirror coatings, A) all Al+25nm MgF$_2$ and B) mirrors 1 and 2 coated with Al+25nm MgF$_2$ with the remaining mirrors Ag + FSS99, indicates that coating system B shows lower diattenuation and lower birefringence than does coating system A. Our ability to vary these diattenuation and birefringence values across the HabEx wavefronts to maximize contrast with in the domain of physically realizable optical metal and dielectric materials is being investigated now in preparation for the 2021 proposal season.

Figure 5-7, below, shows a face on view of HabEx tilted off-axis asphere mirror number one with a map of the retardance changes across the surface. Polarization apodization is revealed by the retardance change between the top and bottom of 4 milli-waves at 500 nm wavelength.

Retardance changes across M1
All Al+25nm MgF$_2$

| 0.0266

0.0266 radians = 0.004 waves
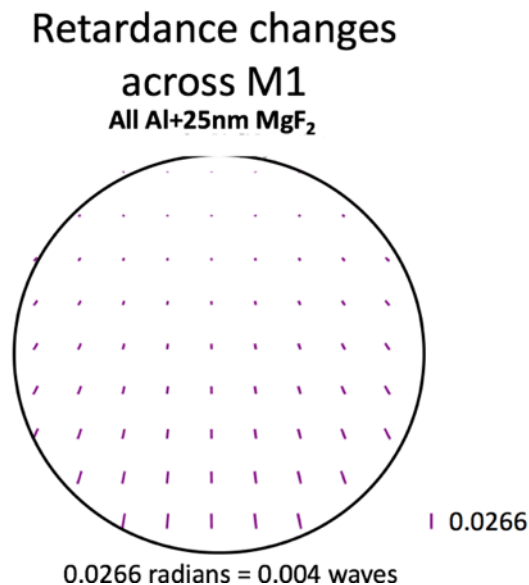
Figure 5-7: Map of the retardance changes across the HabEx 4-m primary mirror (mirror M1), which is a tilted off-axis aspheric mirror with its axis perpendicular to the plane of the paper, just off of the top. This calculation assumes an ideal thin film of Al + 25-nm MgF$_2$. The retardance changes from the top to the bottom by 0.004 waves at 500-nm wavelength. Retardance is minimum at the top of the mirror, because the angles of incidence of these rays are almost normal to the reflecting surface. The lower portion of the mirror is tilted forward in this off-axis optical system, and therefore the retardance is larger across the lower portion of the mirror because on this lower portion of the mirror the surface normal is tilted to the incident ray.

Figure 5-8 shows an image of the exit pupil as viewed looking back through the optical system toward the primary from the focal plane mask in the coronagraph. These cumulative retardance maps are shown for two cases: 1. On the left, all HabEx mirrors coated with Al+25nm MgF_2 2. On the right, the primary and secondary mirrors are AlMgF2 and the remaining mirrors are highly reflective silver (Ag+FSS99).
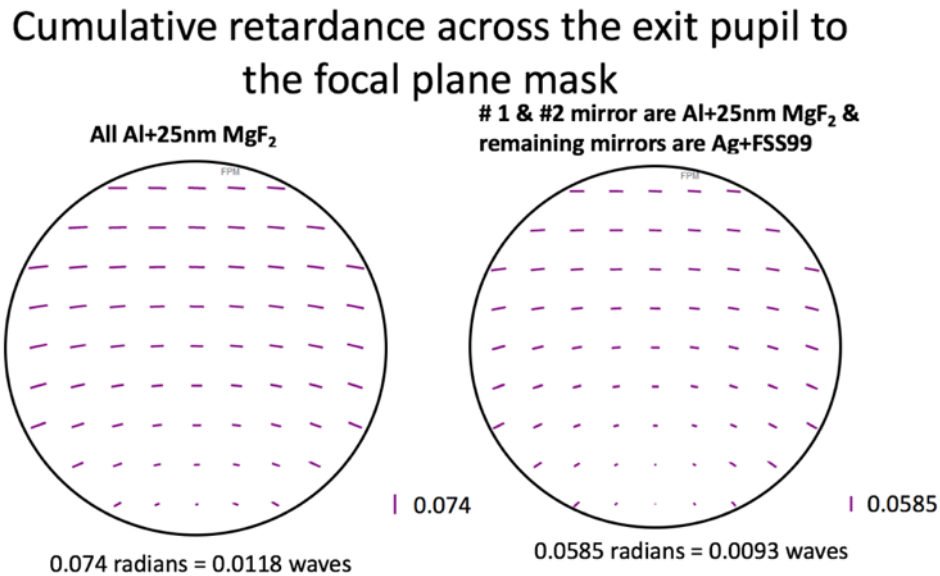
Figure 5-8: Cumulative retardance across the exit pupil to the focal plane mask for the all HabEx mirrors coated with an ideal aluminum plus 25 nm MgF_2 (left) and for HabEx mirrors 1 & 2 with an ideal aluminum plus 25 nm MgF_2 and the remaining mirrors silver overcoated with FSS99 (right). Calculated for 500 nm.
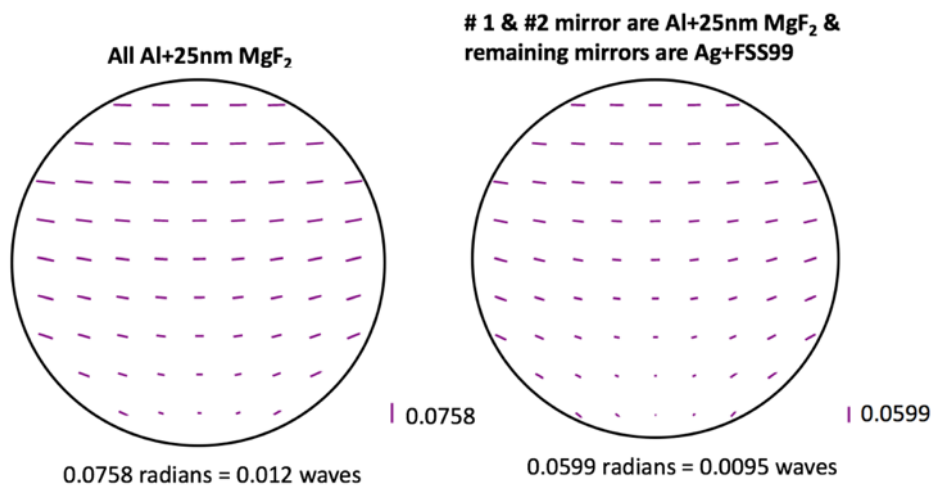
Figure 5-9: Cumulative retardance across the exit pupil to the detector is shown with no occulting mask in the system.

1.1.6   *HABEX JONES PUPIL*

We calculated the Jones pupils for the HabEx assuming that the primary and secondary mirrors were coated with the metal/dielectric stack: aluminum (Al) with an overcoat of 25-nm MgF_2. This coating accommodates other instruments in the system that require high reflectivity in the ultraviolet. The remaining optical elements in the coronagraph are assumed to be coated with the metal/dielectric silver (Ag) and overcoated with FSS99 to maximize system transmission.

Figure 5-10 through **Figure 5-13** below show amplitude and phase of the real and complex terms in the Jones pupil for the HabEx optical system for the wavefront as it reflects from the primary mirror and passes all the way through the optical system up to the occulting mask located at an image plane. These figures show the Jones exit pupil as viewed looking back out of the system toward object space from the occulting-mask focal plane.

We began an investigation of how contrast changes with optical bandwidth by examining chromatic effects. **Figure 5-10** and **Figure 5-11** show the Jones amplitude and phase pupils as they appear with radiation at 450 nm wavelength. **Figure 5-12** and **Figure 5-13** show the Jones amplitude and phase pupils as they appear with radiation at 550 nm wavelength.

For the XY and the YX matrix elements of the Jones pupil, we see a dark band from top to bottom that bends to the left at the top. This dark band shows the zero line of the phase as it changes sign from the right side to the left side of the Jones pupil matrix element for these cross-product terms. The general orientation (clocking) of the dark band depends on the orientation of the flat mirrors[72] in the optical system, and the amount of curvature in the dark band depends on the relative orientation of the off-axis parabolas in the optical system.
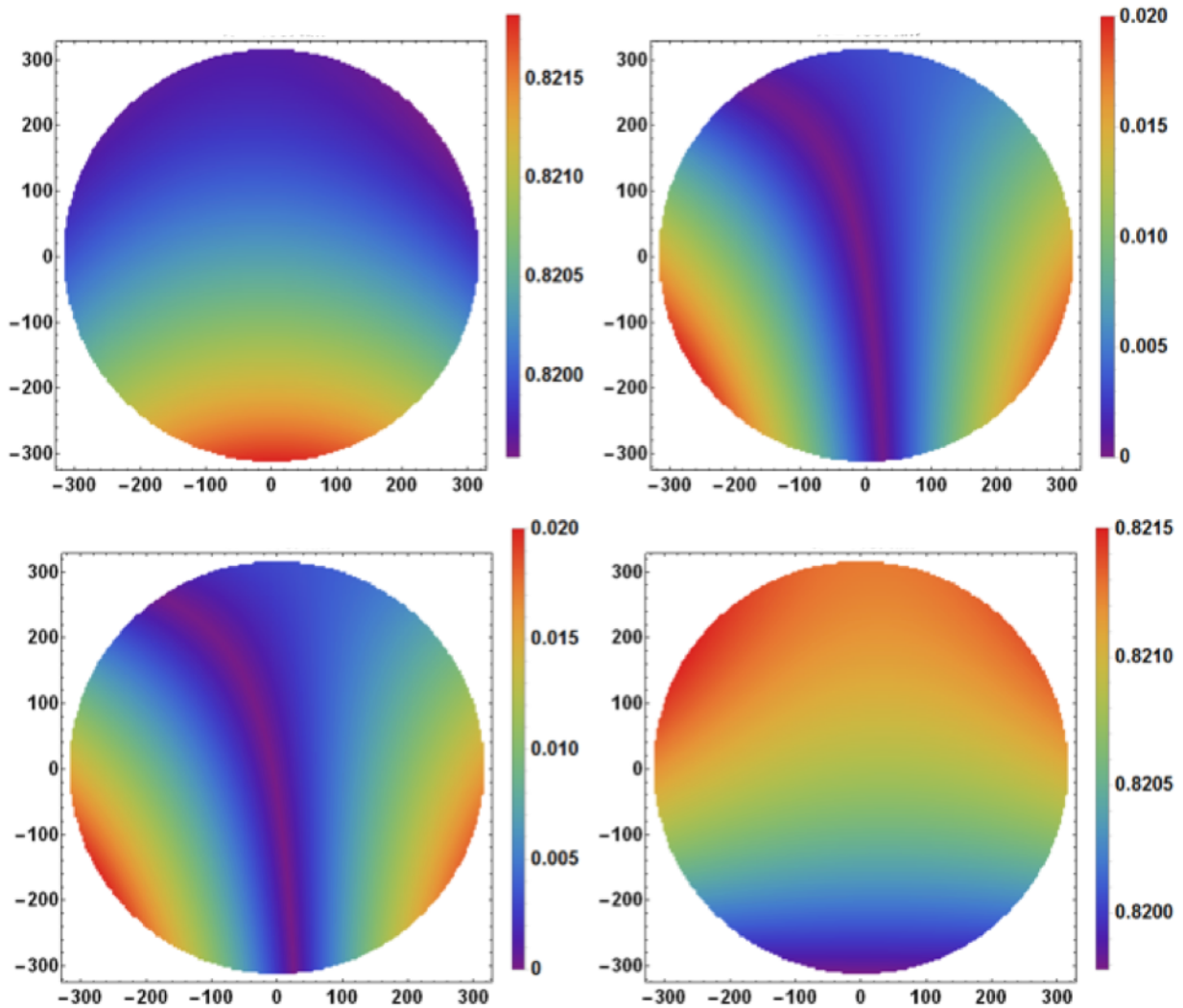
Figure 5-10: Jones exit pupil amplitude as observed from the occulting mask for the HabEx at 450-nm wavelength. Pixel numbers vary from -300 to +300 in both the x and y directions across each of the four pupil images. Color scale shows amplitude reflectivity as a function of position across the exit pupil. Amplitude reflectivity in XX varies by 0.2% top to bottom and YY varies by 0.2% bottom to top.

The following figures show the amplitude and phase of the Jones pupil for HabEx as it appears across the exit pupil to the occulting mask at wavelengths 450 and 550 nm.
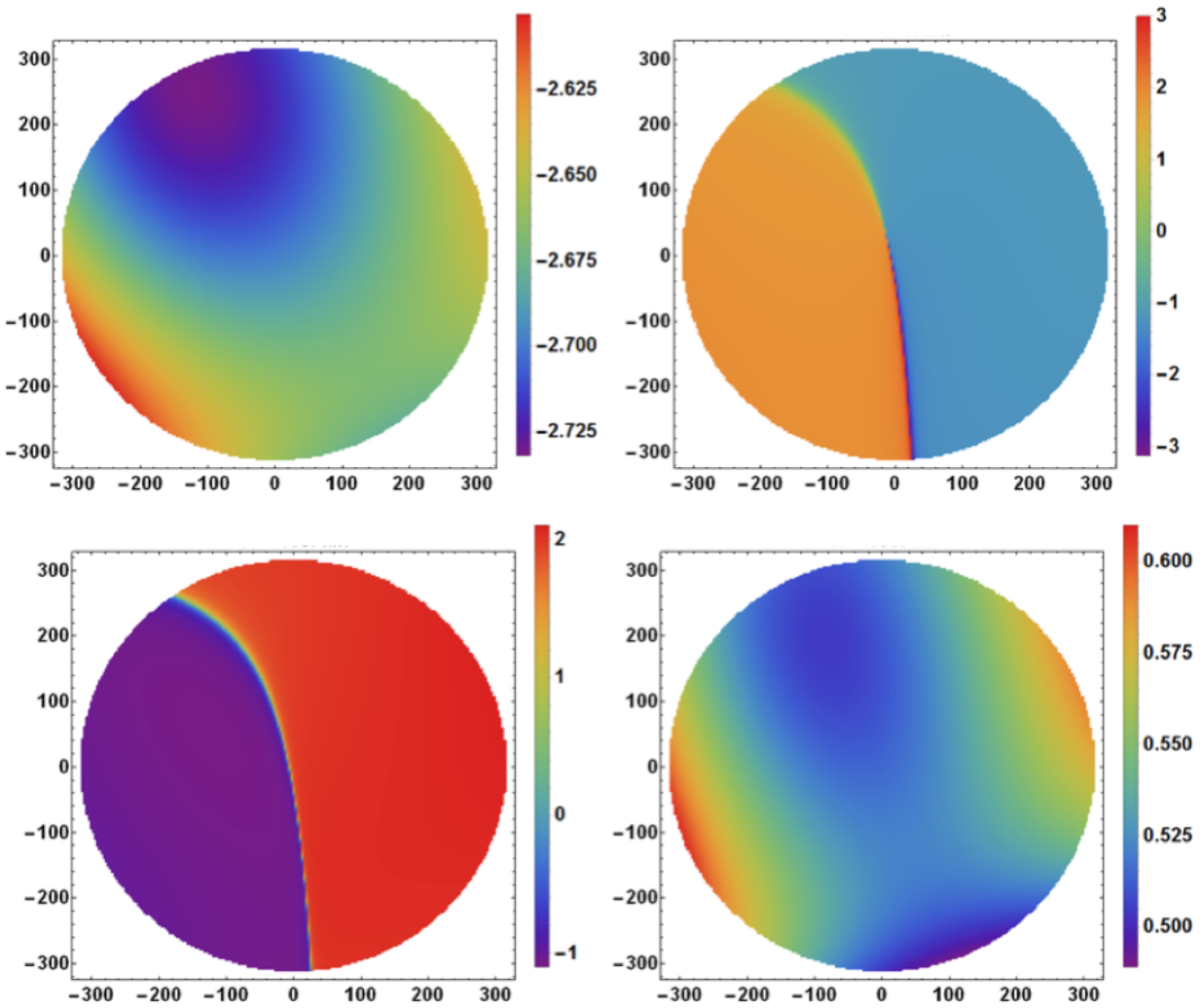
Figure 5-11: Phase changes across the occulting-mask Jones exit pupil as viewed from the occulting-mask focal plane for the HabEx at 450-nm wavelength. Pixel numbers vary from -300 to +300 in both the x and y directions. Color scale shows the phase in units of radians of the amplitude reflectivity as a function of position across the exit pupil. The off-diagonal elements show discontinuities that slice the phase changes by π at the line across the center.
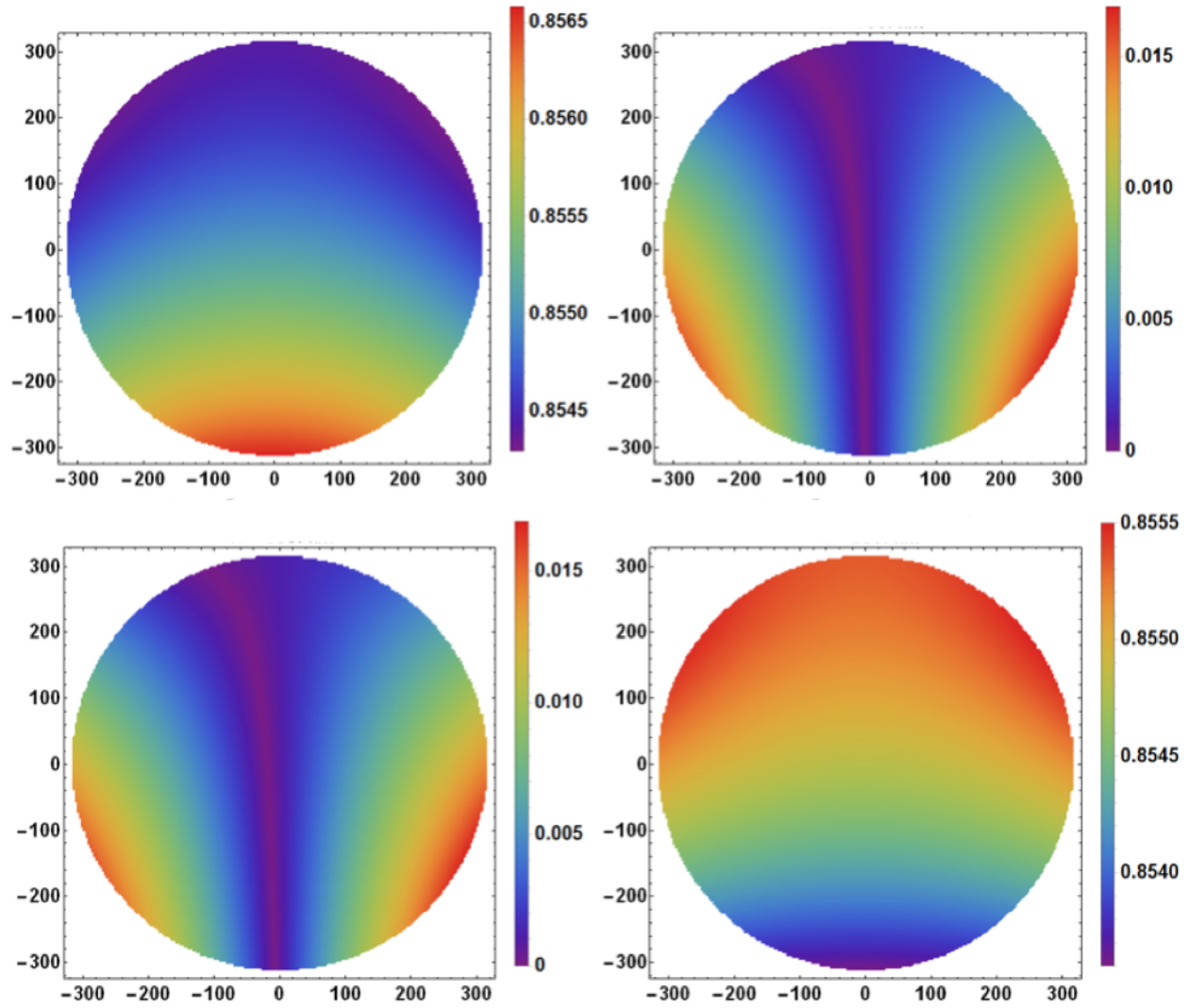
Figure 5-12: Amplitude of the occulting-mask Jones pupil for the HabEx at 550-nm wavelength. Pixel numbers vary from -300 to +300 in both the x and y directions. Color scale shows amplitude reflectivity as a function of position across the exit pupil.
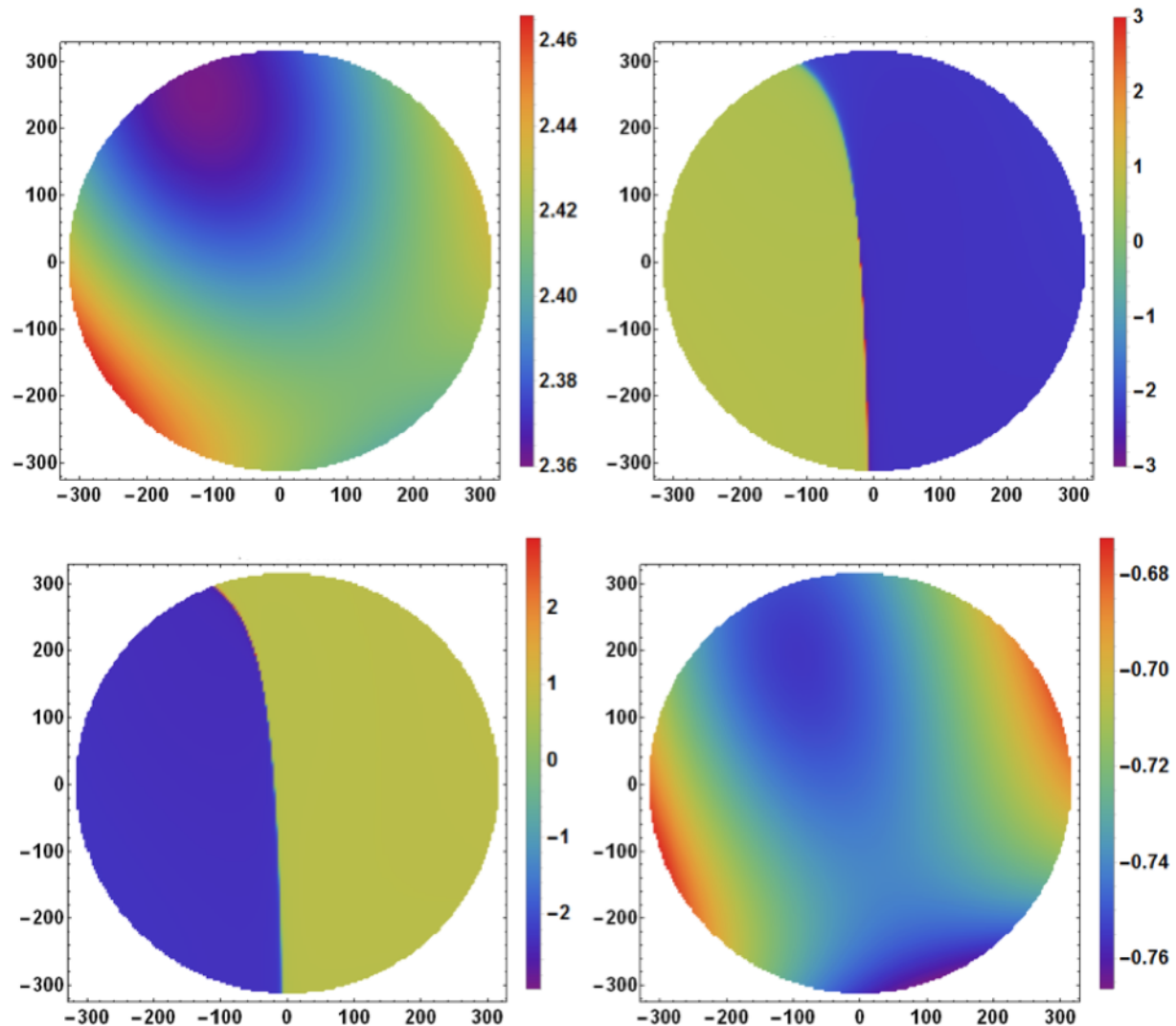
Figure 5-13: Phase changes across the occulting-mask Jones pupil for the HabEx at 550-nm wavelength. Pixel numbers vary from -300 to +300 in both the x and y directions. Color scale shows the phase in units of radians of the phase of the reflectivity as a function of position across the exit pupil. The off-diagonal elements show discontinuities that slice the phase changes by π at the line across the center.

The effect of the chromatic terms is not apparent looking at these figures. The complex indices of refraction for the highly reflective metals (aluminum or silver) are wavelength dependent, as are the dielectric overcoats. The polarization aberrations are therefore wavelength dependent.

Exoplanet testbeds show that contrast worsens as the optical bandwidth is increased, to decrease the magnitude limit of observable exoplanets. In turn, this limits our ability to characterize terrestrial exoplanets, which are significantly fainter than giant exoplanets. Hence, we performed calculations of the Jones pupil at multiple wavelengths to find clues to the origin of this phenomena in anticipation of discovering potential ways to better achromatize the telescope-coronagraph end-to-end optical system.
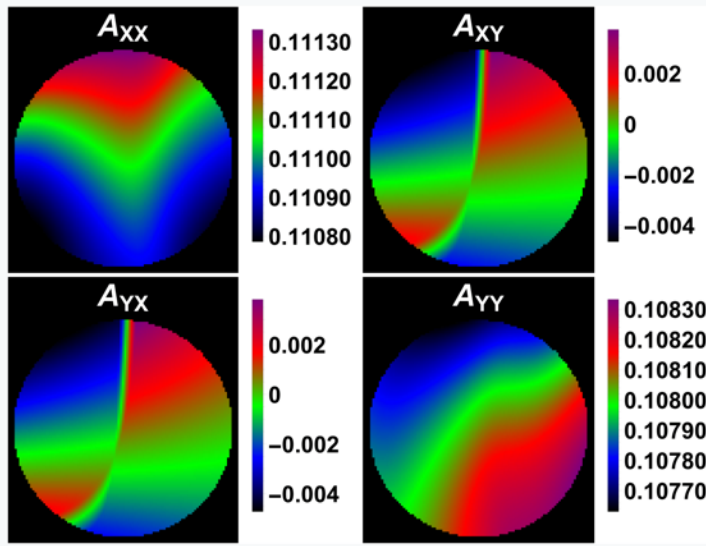
Figure 5-14: Shows the amplitude reflectivity difference terms $\Delta\mathbf{A}(x, y)$ in the Jones matrix. The off-diagonal elements, A_{YX} and A_{XY} are negligible and can be ignored. We see there is an amplitude reflectivity gradient of 0.0005 for $\Delta A_{XX}(x, y)$ and an amplitude reflectivity gradient of 0.00060 for $\Delta A_{YY}(x, y)$.

The complex index of refractions of the thin-film metals (Al, Ag, Au) used in astronomical telescopes are wavelength dependent and therefore, so is the Jones pupil. The calculations here for the HabEx system assumed that mirrors 1 and 2 are coated with Al+25nm MgF$_2$ and that the remaining mirrors are coated with Ag + FSS99.

To more clearly reveal how the wavelength-dependent Jones pupil affects the change in the shape of the wavefront at the exit pupil for the occulting mask as we move from 450 to 550 nm, we performed the difference calculation,

$$\Delta\mathbf{J}(x, y) = \mathbf{J}_{550}(x, y) - \mathbf{J}_{450}(x, y) \qquad \textbf{Equation 5-1}$$

where $\mathbf{J}_{550}(x, y)$ is the Jones pupil shown here in **Figure 5-12** and **Figure 5-13**, which were calculated for 550 nm, and where $\mathbf{J}_{450}(x, y)$ is the Jones pupil shown here in Figures 5-10 and 5-11, which were calculated for 450 nm. We can separate the amplitude and phase matrix differences to write $\Delta\mathbf{J}(x, y) = \Delta\mathbf{A}(x, y) + \Delta\phi(x, y)$.

We show the 2 x 2 matrix for amplitude $\Delta\mathbf{A}(x, y)$ and the 2 x 2 matrix for $\Delta\phi(x, y)$ in **Figure 5-14** and **Figure 5-15**, respectively.

We conclude that changes in <u>amplitude reflectivity</u> with wavelength across the Jones exit pupil to the image plane at the occulting mask is insignificant and will probably not affect the system contrast. This figure references the Jones exit pupil to the image plane directly in front of the coronagraph occulting mask after the wavefront has passed through the 22 optical elements in the HabEx. There is no coronagraph in this system.

Figure 5-15 shows the phase $\Delta\phi(x, y)$ difference in the sense of phase across the exit pupil at 550 nm minus phase across the exit pupil at 450 nm for XX (upper left) and for YY (lower right). This figure references the Jones exit pupil to the image plane directly in front of the coronagraph occulting mask after the wavefront has passed through the 22 optical elements in the HabEx. There is no coronagraph in this system.

Figure 5-15: Shows the phase reflectivity difference terms in the Jones matrix for the exit pupil.. We see there is a gradient of 0.025 radians for $\Delta\phi_{XX}(x,y)$ shown upper left and 0.025 radians for $\Delta\phi_{YY}(x,y)$, shown lower right. The off-diagonal terms YX and XY are noise and can be neglected.

Figure 5-15 shows that the dominate chromatic term is a cylinder, followed by a small tilt. The extent to which this cylinder term affects contrast should be the subject of another investigation. The question of whether polarization aberrations introduced by metal mirrors can be corrected by creating an achromat is an interesting one, and depends on the optical bandwidth over which correction is needed. Unlike in the visible region of the spectrum where crown and flint optical glasses (dielectrics) exist to create an achromat or even an apochromat, the equivalent metal materials remain to be developed. Highly reflecting mirrors are limited to aluminum and silver.

Figure 5-16 shows the phase difference at 550 nm minus the phase difference at 450 nm. These results reveal that a very small opto-mechanical alignment change will need to be made to the system if very precise measurements of object diattenuation are to be made. The instrument may need to be realigned between the two linear polarization measurements, or careful calibration of the system will be needed.

1.1.7 HABEX POINT-SPREAD FUNCTIONS

The complex PSF that interacts with the occulting mask was calculated and shown in **Figure 5-17**. At the focal-plane mask, the DoP changes by 6%. It is slightly less at the detector plane, where it was found to be at 2%. Fine structure is seen. Maximum impact on coronagraph system contrast from this change in DoP across the PSF is unknown and is work for the future. To achieve maximum contrast, it may be necessary to place a complex profile across the occulting mask or the exit pupil to control the DoP. This is a complex mask. Its parameters depend on how well the VV6 is manufactured and the electric field
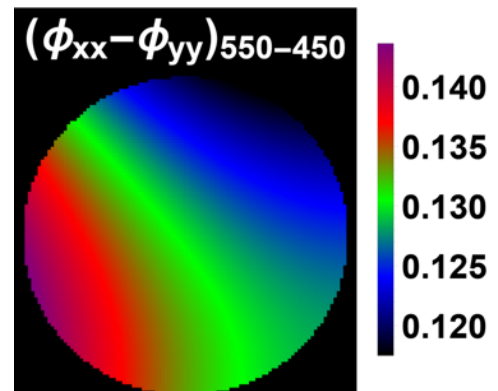
Figure 5-16: Phase difference at 550 nm minus the phase difference at 450 nm is shown to be 20 milliradians.

environment it sits within. A similar mask, called a spatially variable retardance plate (SVRP) is discussed in detail in Clark and Breckinridge[73].
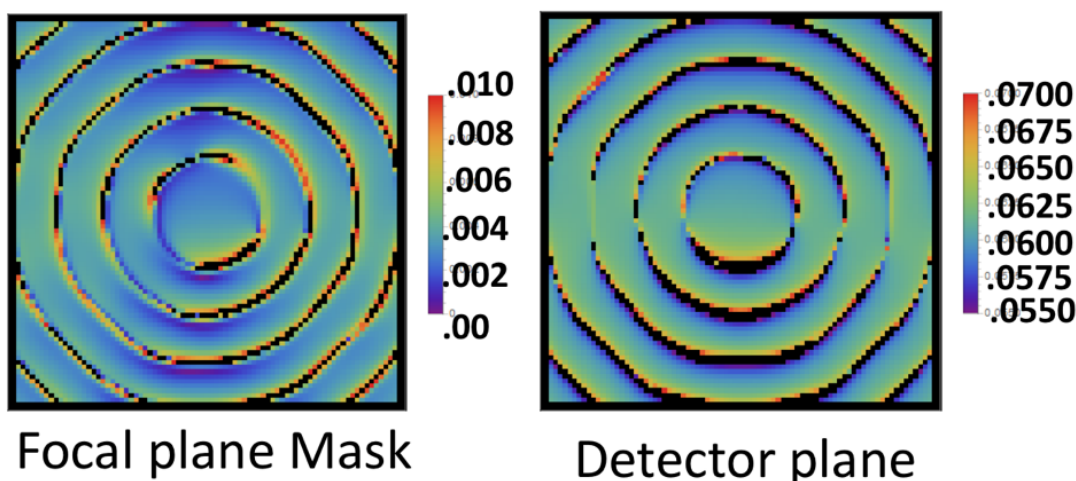
Figure 5-17: Changes in the DoP at 500 nm across the point-spread function of HabEx is shown at the occulting-plane focal mask (left) and at the detector plane under the conditions that the focal plane mask is removed.

The presence of a vector vortex mask at the image plane causes the image to be non-isoplanatic. That is, the image of the exoplanet is not shift invariant across the focal plane of the coronagraph.

The vortex mask sits in the focal plane where the "objects" are diffraction-limited images of stars. The shape of the PSF is not invariant across the image plane in the vicinity of the "center" of the vector vortex mask. If there are point-like objects off the axis of the vortex mask (beyond λ/D), then the vortex masks acts somewhat like a prism, imposing a nonuniform phase across each diffracted star. For example, consider a planet at $20f(\lambda/D)$, where f is system focal length, D is the aperture diameter, and λ is wavelength. The separation between the vortex center (with Airy disk diameter $2f(\lambda/D)$ will subtend an angle: $\tan(\theta) = 2/20 => \theta \simeq 0.1$. The two sides of the Airy disk, along a radius, will have a phase difference that may be quite significant. Note that there is no phase difference across a perpendicular line through the Airy disk, so that one may expect the final image of the exoplanet to be distorted in shape.

We calculated the exoplanet PSF at the final image plane for HabEx using Polaris-M polarization ray tracing for different off-axis planet separations: 60, 100, and 200 milliarc seconds in object space, using broadband light (450 to 550 nm), and calculated the centroid shift at the image plane in the radial direction with and without the VV6 mask.

Table 5-2 shows the results of the calculations performed by Polaris-M for 3 on-sky separations: 60, 100, and 200 msec, with and without the VV6 coronagraph mask.

Table 5-2: Shift variance in the presence of a VV6 mask at the focal plane of the HabEx coronagraph. The HabEx optical system exhibits a small amount of the classic geometric 3rd order aberration: field distortion.

On Sky Separation in m-arc-sec	Image Plane Separation w/o VV6	Image Plane Separation with VV6	Difference m-arc-sec
60	63.79	60.80	2.9870
100	102.38	101.71	0.6730
200	203.03	202.91	0.1137

These changes in the peak of the PSF for different separation angles can be attributed to the non-symmetric variations that the VV6 applies to an off-axis image of an exoplanet. This shift may appear insignificant. However, the exoplanet E & M field must be closely masked to achieve maximum planet signal at the spectrometer designed to be used to record the spectrum of a close-in exoplanet and may be an important system design parameter. For maximum performance, the coronagraph complex mask and the complex stop must impedance match the incoming electric field from the planet/star system.

5.2   COLLABORATE WITH LUVOIR TEAMS TO SUPPORT POLARIZATION ANALYSIS

The optical prescription for the large LUVOIR 8-meter telescope without a coronagraph instrument was delivered to us from GSFC. We polarization ray-traced the optical system from the primary mirror to the image plane where a coronagraph mask will be placed. Digital polarization maps across the exit pupil [Jones Pupil] to the coronagraph mask were delivered to GSFC for their further analysis.

We polarization ray traced the LUVOIR 8-m telescope system through the coronagraph instrument relay optics up to the coronagraph mask and calculated the amplitude and phase component of the Jones exit pupil. The LUVOIR is a large aperture mirror tessellated into an ensemble of regular hexagons. To enable in-space autonomous deployment of the primary mirror these segments are separated 4 to 8-mm depending on the selected deployment design. The LUVOIR primary mirror assembly introduces polarization to the reflected wavefront in two ways: (1) The Fresnel aberrations[74] caused by the double-curved characteristic shape of the ensemble of hexagonal segments, and (2) The gaps between segments form slits which are known to polarize light[75] and the straight line edges of the gaps which are also known to polarize light, but are much weaker. Note the primary mirror is assumed to be continuous and not segmented.

The dominant source of polarization from the LUVOIR primary will be the Fresnel aberrations, which are introduced because the non-paraxial rays intercept the primary mirror at non-normal incidence and reflect with a characteristic polarization footprint. Polarization caused by a 4-mm wide segment gap slit by about a meter in length will be minimum at 500 nm wavelength. At 500 nm wavelength, the 4-mm wide slit has ~0.8 million standing waves across it and optical polarization will be undetectable. Therefore, it is probably not necessary to digitally segment the primary to analyze the LUVOIR polarization aberrations introduced by the primary.

Figure 5-18 shows the four terms for the Jones exit pupil amplitude map for the LUVOIR as viewed from the image plane where the coronagraph mask is located. Units are system amplitude transmittance.

Figure 5-19 shows the four terms for the Jones exit pupil phase map for the LUVOIR as viewed from the image plane where the coronagraph mask is located. Units are system phase in radians.

The data in **Figure 5-18** and **Figure 5-19** show that the LUVOIR 8-m optical system is well corrected for polarization aberrations up to the coronagraph occulting mask.
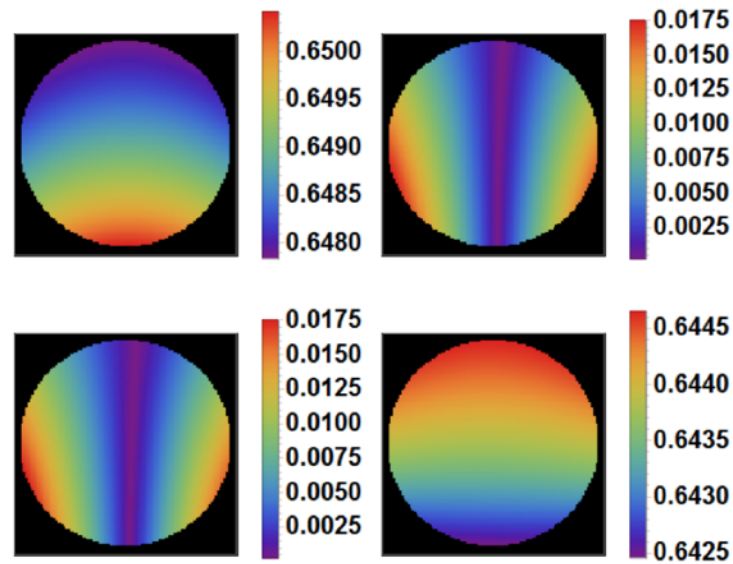
Figure 5-18: Jones exit pupil map as viewed from the coronagraph mask of the amplitude reflectivity terms for the LUVOIR primary mirror (without the HexSegment gap pattern) for the 8-m version. The near-equality of the on-diagonal terms show that the DoP is very small. The average intensity surface reflectance for XX light is about $(0.649)^2$ and varies plus-minus 0.001. The average surface reflectance for YY light is about $(0.645)^2$ and varies plus-minus 0.001, which is excellent. The cross-product terms XY and YX are negligibly small.
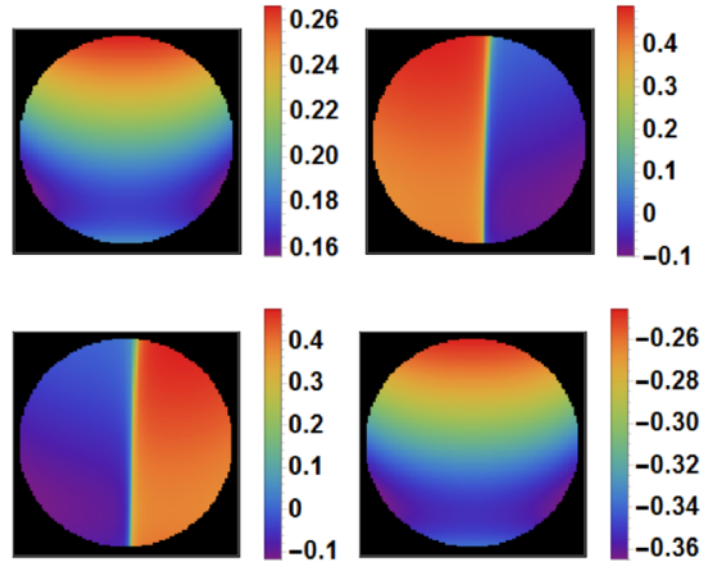
Figure 5-19: Jones pupil of the phase reflectivity terms for the LUVOIR primary mirror (without the HexSegment gap pattern) for the 8-m version. Color shows radians of phase. Note that the on-diagonal elements show these to be a phase wedge across the pupil. This phase wedge will result in a lateral translation of the whole image (all parts simultaneously) at the focal plane. The XX image is separated from the YY image. This can be corrected. To first order, this will not affect coronagraph image quality if the amplitude/phase occulting mask is properly positioned.

6   MILESTONE 3: LARGE-APERTURE MIRROR REFLECTANCE ANISOTROPY: FORM BIREFRINGENCE OF A 3.75-M ALUMINIZED ASTRONOMICAL TELESCOPE SPHERICAL MIRROR

6.1   INTRODUCTION AND RATIONALE

In Section 1, we saw that polarization, introduced into a wavefront by the electromagnetic vector-wave interaction of light and matter, affects the shape of the point-spread function and the distribution of the complex electric field within it. Every surface within all telescope-coronagraph systems interacts in a complex manner with the propagating E&M wave that contains the star/exoplanet image and spectral information.

In 2004, Breckinridge[76] provided an optical testing method to measure the polarization reflectivity as a function of position across a large aperture telescope mirror. This method was implemented along with new, innovative sensing and data processing technique developed by Dr. Brian Daugherty to provide the precision data presented here.

6.2   FORM BIREFRINGENCE

Form birefringence refers to the refractive index anisotropy that occurs in organized structures with feature sizes smaller than the wavelength of light but much larger that the constituent atoms or molecules. Form birefringent structures can have strong polarization properties, and are used for a number of polarization-specific applications. They also occur incidentally during thin-film deposition, which commonly results in subwavelength columnar structure.[77] **Figure 6-1** shows a scanning electron microscope (SEM) micrograph of four types of metal films deposited with different substrate rotations.[78]
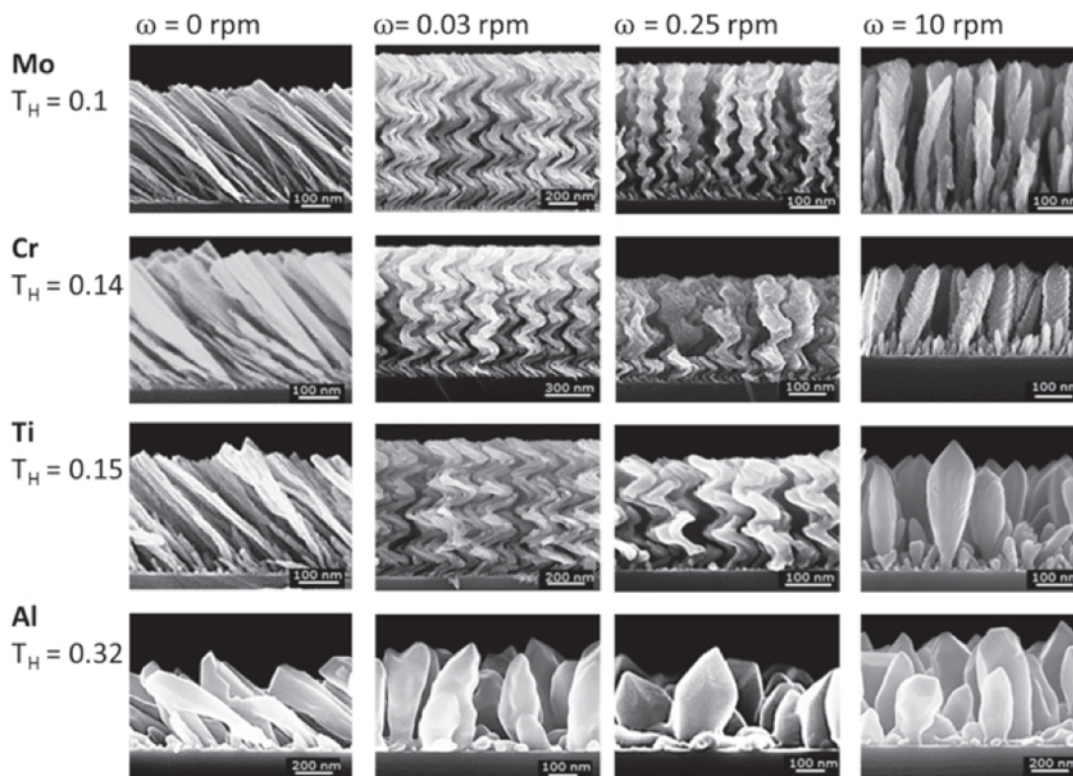
Figure 6-1: SEM micrograph of four metal coatings, molybdenum, chromium, titanium and aluminum, applied at room temperature with a deposition angle of 84° and the substrate rotating with a frequency ω[79]

The wide applicability of form birefringent devices has led to considerable research into new fabrication techniques and better control processes for existing techniques.[80,81,82,83,84,85,86,87,88] Early research demonstrated a relationship between the angle of the columnar nanostructure and the coating deposition angle. Measurements of coatings with tilted columnar nanostructure displayed retardance and diattenuation at normal incidence. Much of the research into fabrication processes focused on oblique angle deposition (OAD) and has led to considerable control over the growth of nanostructure films and the resulting polarization properties.

An area that has not received significant attention is the form birefringence in large astronomical mirrors.[89,90,91] Research into OAD films has demonstrated what coating deposition techniques and conditions promote or reduce columnar growth. Normal incidence deposition in high vacuum reduces contaminants and shadowing effects and produces the most amorphous films. Coating processes for small optical components closely approximate the optimal configuration by arranging the components such that individual components subtend a small angle when viewed from the source. This arrangement requires that at least one dimension of the chamber be much larger than the part diameter and only makes sense from a cost standpoint if coating runs contain many units. It is more challenging to approximate optimal conditions for large-diameter substrates. The sources must be placed much closer to the substrate. Coating chambers equipped with multiple sources and the ability to rotate the substrate produce coatings with good thickness uniformity. However, the process clearly includes oblique deposition geometry, known to produce form birefringence.

A new class of telescopes designed for direct imaging of exoplanets have extremely tight contrast requirements.[92,93,94,95] Any birefringence in the primary mirror will impact the PSF. Adaptive

optics cannot correct for birefringence since all 4 matrix elements of the Jones pupil are co-propagating, and A/O modulate all four optical path lengths (OPLs) simultaneously. It is important to understand the risk associated with form birefringence in large-diameter mirrors. Previously, the form birefringence of large mirrors had not been measured. In view of this, a polarimeter was developed and employed to measure the form birefringence of a 3.75-m diameter aluminum mirror.

6.3   COATING-INDUCED FORM BIREFRINGENCE OF LARGE MIRROR

In order to understand the impact that coating microstructure could have on astronomical telescopes, the form birefringence of a 3.75-m, aluminum-coated mirror were measured. The mirror was found to be weakly polarizing, with low levels of retardance and diattenuation detected. Measurements were performed at several wavelengths. At 450 nm, the maximum retardance measured was 0.002 radians or 3×10^{-4} waves and the maximum diattenuation measured was 0.025%.

This is the first published measurement of form birefringence over a large-diameter mirror. The magnitude of retardance and diattenuation in normal incidence reflection from such mirrors was previously unknown, and the results presented here may or may not be typical of astronomical mirrors and other large reflective optics. The mirror discussed in this work is the fold mirror sphere used in the interferometer for testing Giant Magellan Telescope mirror segments. It was coated at Kitt Peak National Observatory using methods typical of astronomical mirrors in the same chamber and with the same process as that used for the Mayall 4-m ground-based telescope primary mirror and other telescope mirrors in Southern Arizona. This suggests similar levels of form birefringence could be possible in a wide range of astronomical telescope mirrors. See Appendix A for details on the coating process. Most astronomical measurements will not be affected by form birefringence on any of the mirrors.

Although 0.002 radians (6.88-arc minutes) of retardance and 0.025% diattenuation sound very small, they may have a meaningful effect for applications that require 10^{-10} or 0.1 ppb contrast within a few Airy diffraction rings of the center of the PSF. These levels are needed for the direct imaging and spectroscopy of terrestrial exoplanets. The effects of form birefringence cannot be completely corrected with standard adaptive optics wavefront control methods because retardance introduces a different phase shift in each co-propagating polarization wave; adaptive optics only modulate the optical path lengths of the combined wavefront. Further measurement of astronomical mirrors would help assess the risk associated with form birefringence for high-contrast imaging systems.

6.4   EXPERIMENT DESIGN CONSIDERATIONS

This section develops the basic concepts for the apparatus, procedures, and analysis necessary to measure form birefringence of a large mirror. The small value of the form birefringence drives the polarimeter concept. The primary measurement requirement is to isolate form birefringence from other effects
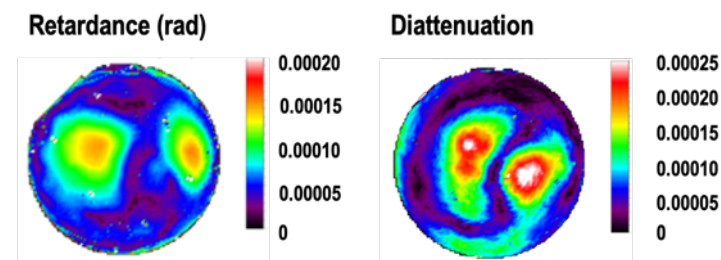
Figure 6-2: Retardance (L) and diattenuation map (R) shown for 450 nm wavelength for the 3.75-m low-expansion glass spherical mirror thin film coated with Al using the process described in Appendix A, which is identical to that of the 4-m Mayall primary mirror at Kitt Peak National Observatory.

such as (1) polarization aberrations, (2) polarizer non-uniformity, (3) polarizer angle dependence, or (4) mirror reflectance variation. The polarimeter concept ensures the retardance and diattenuation are associated with the mirror, by taking repeated measurements as the entire form birefringent polarimeter rotates about the axis. Any polarimeter polarization artifacts will rotate with the polarimeter. Mirror polarization will rotate within the images from frame to frame. These requirements restrict the type of polarization components used in the polarimeter.

6.5   ISOLATING FORM BIREFRINGENCE FROM POLARIZATION ABERRATIONS

In addition to form birefringence, polarization aberrations will affect the mirrors polarization properties. Polarization aberrations are the well-understood polarization dependence found in oblique reflection or transmission at interfaces.[96,97,98,99] The form birefringence polarimeter needs to perform its form birefringence measurements using a method that will not mistakenly include polarization aberrations.

Basic ellipsometry technology applies to the design of the form birefringence polarimeter: (1) ellipsometers measure relevant polarization properties, which is discussed further in the polarimetry section, and (2) specifically polarization properties caused by oblique incidence, the source of polarization the form birefringence polarimeter needs to be suppressed. Ellipsometers' approach to polarization analysis offers multiple methods that should be considered, and the measurement configuration provides a clear example to avoid. Ellipsometers measure the change in the polarization ellipse imparted by a surface and fit the results to previously known models to determine surface properties like film thickness and refractive index.[100,101,102,103] The samples are usually isotropic, so the polarization change occurs due to s- and p-polarized reflection or transmission differences. The ellipsometer's sensitivity is increased by performing measurements in a configuration that maximizes this difference. To accomplish this, ellipsometers commonly perform measurements with large incident angles such as near Brewster's angle.

Figure 6-3 shows the reflectance and polarization properties for an Al-coated surface. The bottom row of plots shows the retardance (left) and diattenuation (right) for selected wavelengths. Both polarization properties increase with incident angle, with diattenuation having a maximum in the vicinity of maximum change in retardance and diattenuation or near Brewster's angle.

   While ellipsometers perform measurements near Brewster's angle to maximize polarization aberrations, it makes sense for the form birefringence polarimeter to perform measurements at normal incidence where polarization aberrations go to zero. Any polarization found at normal incidence will be attributed to form birefringence from anisotropic nanostructure. Due to the quadratic nature of polarization aberrations, performing near-normal incidence measurements is very effective at reducing polarization aberrations. **Figure 6-4** shows the polarization properties of reflection from an Al coating as a function of incidence angle with 6° (0.1047 rad) highlighted. Both retardance and diattenuation from polarization aberrations are reduced to the approximate order of the form birefringence found in the mirror, 3.97×10^{-3} radians and 4.5×10^{-4}, respectively. The form birefringence polarimeter is designed to operate at much smaller angles, with a maximum incident angle of about 0.11°, but this demonstrates that even not such small angles significantly reduce polarization aberrations.
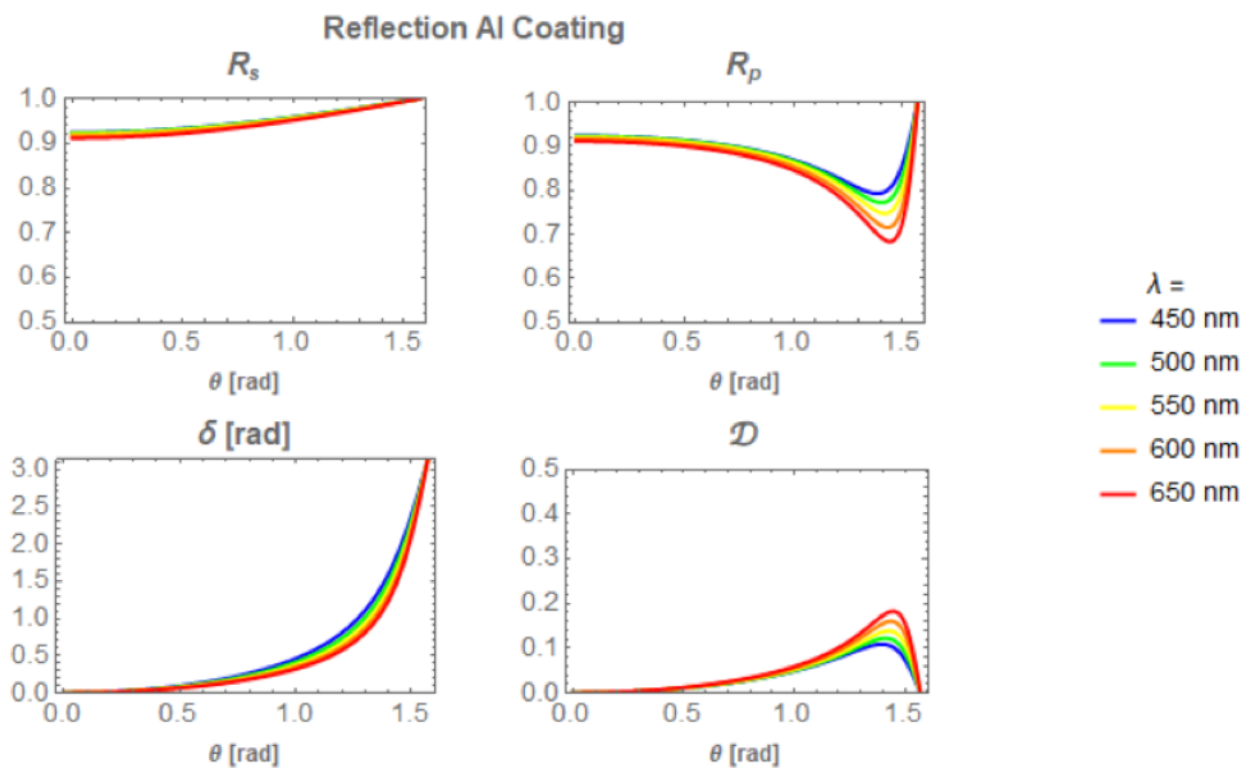
Figure 6-3: Reflection and polarization properties of Al-coated surface with increasing incident angle. Top left, s-polarized reflection, top right, p-polarized reflection, bottom left, retardance in units of radians, bottom right, diattenuation.
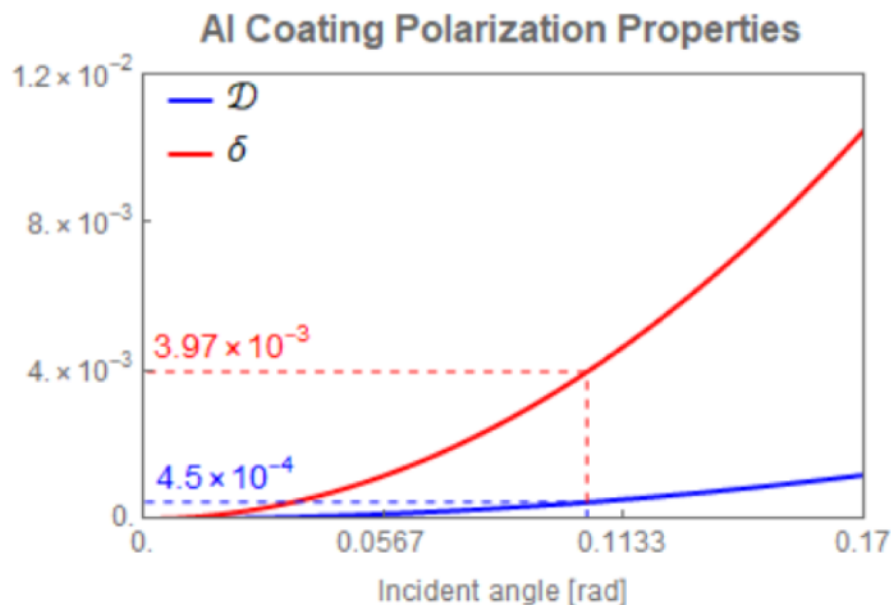
Figure 6-4: Diattenuation, D and retardance δ in reflection from Al coating vs incident angle with .113 radians (6 degrees) angle of incidence highlighted.

The near-normal incidence operation requirement is the primary driver of the overall form birefringence polarimeter layout. The concept, originally proposed by Breckinridge (2004)[90,] of placing all the polarimeter components very close to the center of curvature of a spherical mirror accomplishes both near-normal illumination and view angles over the entire mirror surface. **Figure 6-5** shows the basic layout. If the light source beam angle fills the mirror's aperture with limited overfill, the system will be extremely light efficient with almost all of the illumination reaching the detector. This measurement geometry limits the samples that the form birefringence polarimeter can measure to approximately spherical with an accessible center of curvature. The dimensions shown in **Figure 6-5** limit the maximum incident angle to about 0.002 radians corresponding to retardance and diattenuation of 1.4×10^{-6} radians and 1.6×10^{-7}, respectively.

The key technologies developed and reported here are:

1.   Processes needed to measure spatially dependent amplitude and phase reflectivity from a spherical metal-coated glass mirror from the center of curvature and how those relate to astronomical telescope measurements.

2.   Precision apparatus to make the hardware measurements to the needed precision.

3.   Algorithms to process the data.
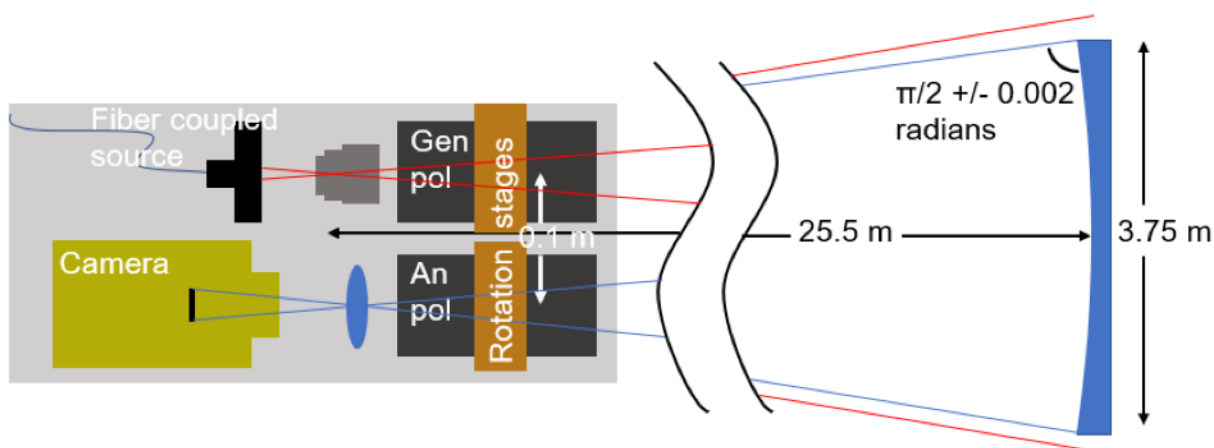
Figure 6-5: Form birefringence polarimeter basic layout and dimensions.

Figure 6-5 left shows the mirror illumination and imaging apparatus. This apparatus sits near the center of curvature of the 3.75-m test mirror shown to the right. The radius of curvature of this test mirror is 25.5 m. The illumination apparatus is shown at the top left. It consists of a fiber-coupled source whose output (left to right) beam passes through a polarizer and fills the 3.75-m mirror located 25.5 m away. This polarizer is called the generator polarizer (Genpol) and is mounted on a rotation stage. The polarized light from the source reflects from the aluminized test mirror and passes back, right to left through a polarization analyzer (Anpol) that is mounted to a second rotation stage. The returning light then passes into a camera that images the 3.75-m mirror that is illuminated in polarized light, onto a CCD enabling us to analyze the spatial dependence of polarization reflectivity across the mirror.

6.6   MEASUREMENT ENVIRONMENT–RELATED CALIBRATION LIMITATIONS

Polarimeters reduce a set of intensity modulations into polarization information. Calibration is the process of determining the relationship of the intensities to Stokes or Mueller parameters. In Mueller matrix polarimetry, the mathematical description of a measurement is,

$$\mathbf{D=AMG} \hspace{4cm} \text{Equation 6-1}$$

where **D** is a vector of detected intensities, **A** contains all of the analyzer vectors describing how the polarimeter responds to any Stokes vector leaving the sample, **M** is the Mueller matrix of the sample, and **G** contains generator vectors defining the illumination side of the polarimeter. This equation assumes a linear detector response. The calibration process determines **A** and **G** so that once **D** is measured, **M** can be calculated. One method for determining **A** and **G** is to use a priori knowledge of the polarization elements to model the instrument. The model parameters are determined by performing one or more calibration measurements on known samples, and **A** and **G** are calculated based on the model.[104,105,106,107,108] The other category of calibration techniques determines **A** and **G** without using a priori knowledge of the polarimeter by performing calibration measurements on known samples until **A** and **G** are overdetermined.[109]

Both techniques assume that the system configuration during calibration is the same as the configuration during measurements, except for the sample. The system must remain stable and

repeatable between calibration and measurement. Both methods require measurements to be performed with reference samples. For logistics reasons, this form birefringence experiment will not meet any of these requirements and repeated calibration was necessary.

In preparation for this measurement, the form birefringence polarimeter was constructed and tested in Professor Chipman's Polarization Laboratory at the University of Arizona and then transported across the street to the Richard F. Caris Mirror Lab for the measurement. Measurements were performed after hours or on weekends with the form birefringence polarimeter stored out of the way during business hours to avoid interfering with work on the Giant Magellan Telescope. This necessitated moving and aligning the experiment prior to each measurement, therefore maintaining a high degree of repeatability was difficult. Additionally, since the apparatus illuminates and views the sample from the center of curvature, there is no straightforward way to replace the sample with a known calibration standard. These calibration issues result in a requirement that the measurement procedure and data reduction determine the form birefringence using only data collected during one measurement cycle.

6.7   POLARIMETRY OVERVIEW

The form birefringence polarimeter, developed for this effort, measures linear retardance and linear diattenuation. The engineering description is provided in Section 7. The experiment is performed so that, for weakly polarizing samples, the retardance can be calculated from the minimum transmission between two polarizers and the diattenuation can be calculated from the relative orientation of the polarizers that results in minimum transmission. This approach does not require calibration, but the diattenuation calculation requires significant modeling and assumptions due to hardware limitations. This section explains the polarimetry using Mueller calculus.

Weak retarders expressed in radians and weak diattenuators expressed in dimensionless diattenuation cause the same level of leakage between crossed polarizers by different mechanisms. **Figure 6-6** shows the evolution of horizontally polarized light incident on various linear retarders. Each circle represents a different retarder orientation with the circle's rotation axis intersecting the retarder's fast and slow axis coordinates on the Poincaré sphere. The circle represents the output polarization as the retardance varies from 0 radians to 2π radians. All of the circles are tangential when $\delta = 0$ and move with trajectories from horizontal toward right circular polarization. For small linear retardances acting on linearly polarized light, the primary effect is to induce a circular component. In a system consisting of a linear retarder between two linear polarizers, if the retarder fast axis is not parallel or perpendicular to the first polarizer transmission axis, it will introduce a small circularly polarized component. Regardless of orientation, the second polarizer will transmit half of the circular component. This is the leakage that the form birefringence polarimeter measures at the best null position.

Figure 6-6: The circles depict how various linear retarders will modify horizontal polarized light. As the retardance changes from 0 to 2π, the polarization state travels around a circle centered on an axis through the fast and slow axis directions or the retarder.

A linear diattenuator acting on a linear polarization state causes the state to move along the sphere's equator

toward the diattenuator's transmission axis. The movement along the equator is a polarization rotation allowing a portion of the light to leak through the second polarizer. The polarization leaving the weak diattenuator remains linearly polarized, so complete extinction can still be achieved by rotating the second polarizer to the correct angle. The rotation angle depends on the magnitude of diattenuation. This is the orientation that the form birefringence polarimeter measures in order to calculate diattenuation.

The form birefringence polarimeter can separately measure weak linear retardance and linear diattenuation by using a procedure that measures linear retardance as leakage between crossed polarizers and linear diattenuation as a rotation of the polarization state. Circular retardance will also cause a polarization rotation, and circular diattenuation will cause a leakage. These effects are not distinguishable in a single measurement, but by rotating the polarizers and repeating the measurements, the leakage and orientation associated with linear polarization properties will oscillate, while leakage and orientation caused by circular polarization properties will remain constant. Circular retardance and circular diattenuation are not anticipated, and thus would not couple into the present measurements even if present.

The retardance portion of the measurement is expressed in Mueller calculus below. The Mueller matrices for a linear retarder of retardance δ and orientation θ, (see **Equation 6-2** below) and polarizers at 0° and 90° (see **Equation 6-3** and **Equation 6-4** below). The intensity transmission through the combination is calculated by cascading the matrices and multiplying by the Stokes parameters for horizontal polarized light {1,1,0,0}. The result shows that the intensity will have a sign squared dependence on retardance and depend on the sine of twice the orientation,[110]

$$\text{LR}[\delta,\theta]=$$

Equation 6-2

$$\begin{pmatrix} 1 & 0 & 0 & 0 \\ 0 & \cos\delta\sin^2(2\theta)+\cos^2(2\theta) & \sin^2(\delta/2)\sin(4\theta) & -\sin\delta\sin(2\theta) \\ 0 & \sin^2(\delta/2)\sin(4\theta) & \cos\delta\cos^2(2\theta)+\sin^2(2\theta) & \sin\delta\cos(2\theta) \\ 0 & \sin\,\delta\sin(2\theta) & \sin\,\delta(-\cos2\theta) & \cos\delta \end{pmatrix}$$

A linear polarizer oriented at zero (0°) degrees is modeled in the Stokes formalism as shown in **Equation 6-3**.

Equation 6-3

$$\text{LP}[0^o]=\begin{pmatrix} 1/2 & 1/2 & 0 & 0 \\ 1/2 & 1/2 & 0 & 0 \\ 0 & 0 & 0 & 0 \\ 0 & 0 & 0 & 0 \end{pmatrix}$$

A linear polarizer oriented at ninety (90°) degrees is modeled in the Stokes formalism as shown in **Equation 6-4**:

$$
LP\left[90^{o}\right] = \begin{pmatrix} 1/2 & -1/2 & 0 & 0 \\ -1/2 & 1/2 & 0 & 0 \\ 0 & 0 & 0 & 0 \\ 0 & 0 & 0 & 0 \end{pmatrix}
$$

Equation 6-4

Sandwiching retarder plate between two orthogonal linear polarizers gives:

$$
LP\left[90^{o}\right] \cdot LR\left[\delta,\theta\right] \cdot LP\left[0^{o}\right] =
$$

Equation 6-5

$$
\begin{pmatrix} 2\sin^2(\delta/2)\sin^2\theta\cos^2\theta & 2\sin^2(\delta/2)\sin^2\theta\cos^2\theta & 0 & 0 \\ -2\sin^2(\delta/2)\sin^2\theta\cos^2\theta & -2\sin^2(\delta/2)\sin^2\theta\cos^2\theta & 0 & 0 \\ 0 & 0 & 0 & 0 \\ 0 & 0 & 0 & 0 \end{pmatrix}
$$

To obtain the intensity, we calculate the Stokes vector out, S_{out}, to find:

Equation 6-6

$$
S_{out} = \begin{pmatrix} 2\sin^2(\delta/2)\sin^2\theta\cos^2\theta & 2\sin^2(\delta/2)\sin^2\theta\cos^2\theta & 0 & 0 \\ -2\sin^2(\delta/2)\sin^2\theta\cos^2\theta & -2\sin^2(\delta/2)\sin^2\theta\cos^2\theta & 0 & 0 \\ 0 & 0 & 0 & 0 \\ 0 & 0 & 0 & 0 \end{pmatrix} \cdot \begin{pmatrix} 1 \\ 1 \\ 0 \\ 0 \end{pmatrix} =
$$

$$
= \begin{pmatrix} \sin^2\left[\dfrac{\delta}{2}\right]\sin^2\left[\theta\right] \\ -\sin^2\left[\dfrac{\delta}{2}\right]\sin^2\left[\theta\right] \\ 0 \\ 0 \end{pmatrix}
$$

and then,

Equation 6-7

$$
I_{out} = S_{out} \cdot 1 = \sin^2\left[\frac{\delta}{2}\right]\sin^2\left[2\delta\right]
$$

Since $\delta \ll 1$, we can expand the intensity to two orders around δ to obtain a quadratic dependence on δ, to be $\left(\dfrac{\delta}{2}\right)^2 \sin^2(2\theta)$. The maximum value of $\left(\delta^2/4\right)$ occurs at sample orientations of 45° repeating every 90° of retarder rotation.

To obtain the measurable intensity, we take the modulus squared of the complex field and find:

Equation 6-8

$$I = \sin\left(\frac{\delta}{2}\right)^2 \sin(2\theta)^2$$

Since $\delta \ll 1$, we are able to expand the intensity given by the equation above to two orders around δ, resulting in a quadratic dependence on δ, $\left(\frac{\delta}{2}\right)^2 \sin^2(2\theta)$. The maximum value of $\delta^2/4$ occurs at sample orientation of 45° repeating every 90° of retarder rotation.

The effect of diattenuation is modeled using the Mueller calculus to determine the change in polarization orientation imparted on a horizontal incident state by a linear diattenuator. We model the rotation to horizontal incident polarization caused by a diattenuator with diattenuation $\mathfrak{D}$ and orientation θ. The first-order expansion gives the rotation caused by a weak diattenuator. The Mueller matrix of a linear diattenuator **LD**, with diattenuation $\mathfrak{D}$ and orientation $\boldsymbol{\theta}$ is:

Equation 6-9

$$\mathrm{LD}[\mathfrak{D},\theta] =$$

$$\begin{bmatrix}
\dfrac{1}{\mathfrak{D}+1} & \dfrac{\mathfrak{D}\cos(2\theta)}{\mathfrak{D}+1} & \dfrac{\mathfrak{D}\sin(2\theta)}{\mathfrak{D}+1} & 0 \\[2ex]
\dfrac{\mathfrak{D}\cos(2\theta)}{\mathfrak{D}+1} & \left\{\left(\sqrt{\dfrac{2}{\mathfrak{D}+1}}-1\right)\sin^2(2\theta)+\dfrac{\cos^2(2\theta)}{\mathfrak{D}+1}\right\} & \dfrac{1}{2}\left(\dfrac{1}{\mathfrak{D}+1}-\sqrt{\dfrac{2}{\mathfrak{D}+1}}-1\right)\sin(4\theta) & 0 \\[2ex]
\dfrac{\mathfrak{D}\cos(2\theta)}{\mathfrak{D}+1} & \dfrac{1}{2}\left(\dfrac{1}{\mathfrak{D}+1}-\sqrt{\dfrac{2}{\mathfrak{D}+1}}-1\right)\sin(4\theta) & \dfrac{\sin^2(2\theta)}{\mathfrak{D}+1}+\left(\sqrt{\dfrac{2}{\mathfrak{D}+1}}-1\right)\cos^2(2\theta) & 0 \\[2ex]
0 & 0 & 0 & \sqrt{\dfrac{2}{\mathfrak{D}+1}}-1
\end{bmatrix}$$

For horizontal input polarization, the output polarization state and its first-order series expansion around $\mathfrak{D}=0$ are found by calculating:

Equation 6-10

$$LD[\mathfrak{D},\theta]\cdot\begin{pmatrix}1\\1\\0\\0\end{pmatrix}=$$

$$\begin{pmatrix}\dfrac{1}{\mathfrak{D}+1}\mathfrak{D}\cos(2\theta)+1\\[2mm]\dfrac{1}{\mathfrak{D}+1}(\mathfrak{D}+1)\left[\sqrt{\dfrac{2}{\mathfrak{D}+1}}-1\right]\sin^2(2\theta)+\mathfrak{D}\cos(2\theta)+\cos^2(2\theta)\\[2mm]\dfrac{1}{2(\mathfrak{D}+1)}2\mathfrak{D}\sin(2\theta)-(\mathfrak{D}+1)\left[\sqrt{\dfrac{2}{\mathfrak{D}+1}}-1\right]\sin(4\theta)+\sin(4\theta)\\[2mm]0\end{pmatrix}=$$

$$=\begin{pmatrix}1-2\mathfrak{D}\sin^2(\theta)\\\mathfrak{D}\cos(2\theta)-\mathfrak{D}+1\\\mathfrak{D}\sin(2\theta)\\0\end{pmatrix}$$

The output polarization orientation is then found from the approximate output Stokes parameters to give:

$$\text{AoLP}=\frac{1}{2}\tan^{-1}\left[\frac{S_2}{S_1}\right]\approx\frac{1}{2}\tan^{-1}\left[\frac{\mathfrak{D}\sin(2\theta)}{\mathfrak{D}\cos(2\theta)-\mathfrak{D}+1}\right]$$

Equation 6-11

Where AoLP is the angle of linear polarization.

We want to find an orientation, AoLP, such that the diattenuation is small, or $\mathfrak{D}\approx 0$. Then, since $\mathfrak{D}\ll 1$ for small values of $\mathfrak{D}$, we can write:

Equation 6-12

$$AoLP\approx\frac{1}{2}\mathfrak{D}\sin(2\theta)$$

A weakly deattenuating sample will cause a maximum rotation in radians equal to its diattenuation. The magnitude of the rotation will depend on the diattenuator's orientation relative to the incident polarization state and will repeat every 180°.

The form birefringence polarimeter measures retardance by measuring the intensity transmission through two linear polarizers that have been aligned to minimize transmission. It measures diattenuation by measuring the angle between the polarizers at minimum transmission. As the polarizers are rotated together, the measurement can be repeated at different configurations. The leakage used to calculate retardance will modulate with 90° periodicity, and the orientation used to

calculate diattenuation will modulate with 180° periodicity. This separates the linear polarization effects of interest from circular polarization effects and depolarizer scattering.

The form birefringence polarimeter's polarimetry uses aspects from both nulling ellipsometry and photometric ellipsometry. A null ellipsometry approach would have added a quarter waveplate to the system so that full extinction could always be achieved. The relative angles of all three components are then used to determine both the retardance and diattenuation. The form birefringence polarimeter uses this concept to measure diattenuation but avoided using it for retardance. The primary reason is that motorized components in the system were not accurate enough to provide accurate absolute positions, and the near normal incidence configuration would make it difficult to calibrate the relative component orientations. More detailed discussion of the issues using orientation information can be found in the diattenuation data reduction section 7.3 Data Reduction beginning page 7-15 and section 7.7, page 7-22. The retardance measurement used a photometric ellipsometry concept by detecting the amplitude of a modulated signal. Using this approach allowed the form birefringence polarimeter to use only polarizers, which was preferable than using both retarders and linear polarizers based on the limited calibration capabilities.

7   THE FORM BIREFRINGENCE POLARIMETER
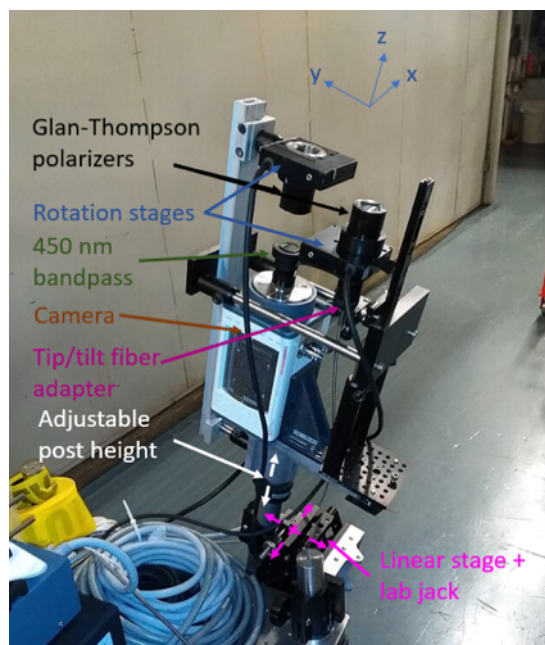
Figure 7-1: Photograph of the form birefringence polarimeter. Light travels in the z-direction toward a spherical mirror six meters above.

Figure 7-1 shows a photograph of the form birefringence polarimeter hardware with the important components labeled. This section will give additional details on the instrument including a description of the data acquisition software routine.

7.1   POLARIZATION COMPONENTS

The form birefringence polarimeter has two identical α-BBO Glan-Thompson polarizers. One polarizer placed after the source is used to generate the linear polarized illumination state. A polarizer before the camera analyzes the incoming polarization. The polarizers are Red Optronics GMP-6020; they have 20 mm clear apertures with extinction ratio specifications $< 5\times10^{-6}$ and a large field of view $>15°$. The usable field of view and the extinction ratio depend on how the polarizers are used. In the form birefringence polarimeter the useful field of view is smaller than $15°$ and the extinction ratio is better than advertised. This will be discussed in the data analysis section.

Light Source – Illumination is provided by a broadband xenon arc lamp coupled into a 1/8-m monochromator. All measurements presented here were performed at 450 nm. The output of the monochromator was fiber coupled to the instrument, and where the fiber was placed near the front focal plane of a microscope objective and slightly overfilled the mirror.

Mechanical Components – The polarizers are mounted to Newport sr50cc motorized rotation stages and controlled by a Newport 301 motion controller. The stages provide precise positioning when stepped at low speed in a single direction. The accuracy decreases due to backlash when the direction of travel is reversed. The motor's absolute accuracy limitations force some assumptions during the diattenuation data reduction. This is discussed in the diattenuation part of the data reduction section.

The alignment of the form birefringence polarimeter requires that all six degrees of freedom have some adjustability. The tip/tilt of the entire system requires coarse adjustment to aim the camera at the mirror. This is provided by moving the entire table holding the form birefringence polarimeter and adjusting the angle between the base post and the instrument axis. There is also coarse rotation of the entire instrument head about its axis. This is performed by rotating the axis post in its clamp. The source is fiber coupled to a tip-tilt adapter connected to the projection objective. This allows the source to be centered on the sample once the camera is aligned. With both camera and source aligned, the instrument head needs to be translated so that the light returned from the mirror is centered on along the analyzer axis of the form birefringence polarimeter. This requires sub-millimeter two axis positioning. A manual linear translation stage provides the entirely

horizontal movement in the x-direction and a lab jack provides movement in the y-direction. An adjustable collar on the instrument axis post allows translation along z.

Camera – The form birefringence polarimeter uses a Hamamatsu c9100-13 ImagEM Enhanced camera. The detector is 512 x 512 pixels with an area of 8.19 mm x 8.19 mm, and 16 μm square cells. It is an electron multiplying, back-thinned frame transfer CCD detector that can has usable quantum efficiency down to 300 nm. It is a 16-bit camera with 16 electron readout noise and 0.01 electron/s/pixel dark noise. It responds linearly over nearly its full dynamic range, which was verified with calibrated density filters.

7.2   CONTROL SOFTWARE

A LabVIEW based program controls the polarizer rotation stages and the camera, acquiring and storing raw images, and performing the first data reduction step and storing the reduced images. The automation is important because each measurement involves acquiring 221 raw image files. The software provides a setup screen that shows a live image from the camera and allows manual control of the polarizer rotation stages, the monochromator output wavelength, and the controls used to specify parameters for an automated measurement. Once parameters are specified and the start button is activated, the program populates an empty directory with folders with names based on the scan parameters. The program then checks for empty folders and performs the measurement specified by the first one it sees. This process continues until there are not empty folders left in the directory. When a folder is selected the program parses the folder name to determine the generator angle to use. The generator polarizer rotates to the specified angle and the analyzer rotates the generator angle plus 89 degrees. The analyzer then takes two 1° steps with an image acquired before each step and after the last step. The images are used to determine the approximate null angle to center the +/- 0.4° scan. The analyzer polarizer rotates to 85° then rotates to its starting position for the +/- 0.4° scan. The camera exposure is determined based on the signal strength and then 13 images are acquired as the analyzer steps through 0.8°. Quadratic curve fitting is used to obtain a leakage map and an orientation map for each wavelength. All of the raw data and both maps are exported and the program checks for the next empty folder.

7.3   DATA REDUCTION

The following section explains the process used to reduce the 221 images acquired for each form birefringence polarimeter data set into a retardance map and a diattenuation map showing the mirror's form birefringence. As discussed in the polarimetry section, the retardance is calculated using the minimum transmission through linear polarizers and the diattenuation is calculated from the relative orientation at which the minimum transmission occurs. This results in two distinct data reduction methods that only share the first step. This section begins with the common first step, then explains the retardance calculation followed in the diattenuation calculation.

7.4   DATA PRODUCT EXAMPLE

The form of the required final data product is shown in **Figure 7-2** and **Figure 7-3.** Here we see the both the retardance and the diattenuation maps for the 3.75-m diameter optical test sphere. We see the retardance varies between 0 and 2 milliradians. Low spatial frequency structure is

apparent, which, if this coating were to be used on HabEx, will place unwanted radiation near the foot of the PSF to mask terrestrial exoplanets.
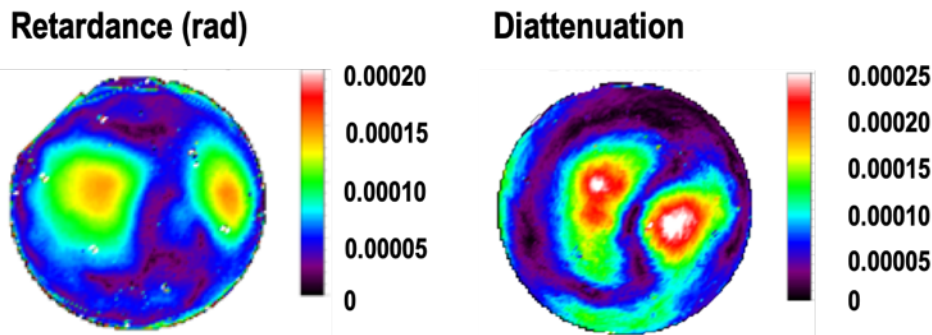
Figure 7-2: (Identical to Fig. 6-2) Retardance and diattenuation measured for the 3.75-meter sphere, aluminized in the same manner at the 4-m Mayall astronomical telescope. These are maps of the polarization reflectivity changes across the telescope aperture. Retardance varies slowly across the mirror with a peak to valley value 0 to 2 milliradians of phase at 500 nm wavelength. The dominate spatial frequency is about 1 ½ cycles across the 3.75 meter diameter mirror.
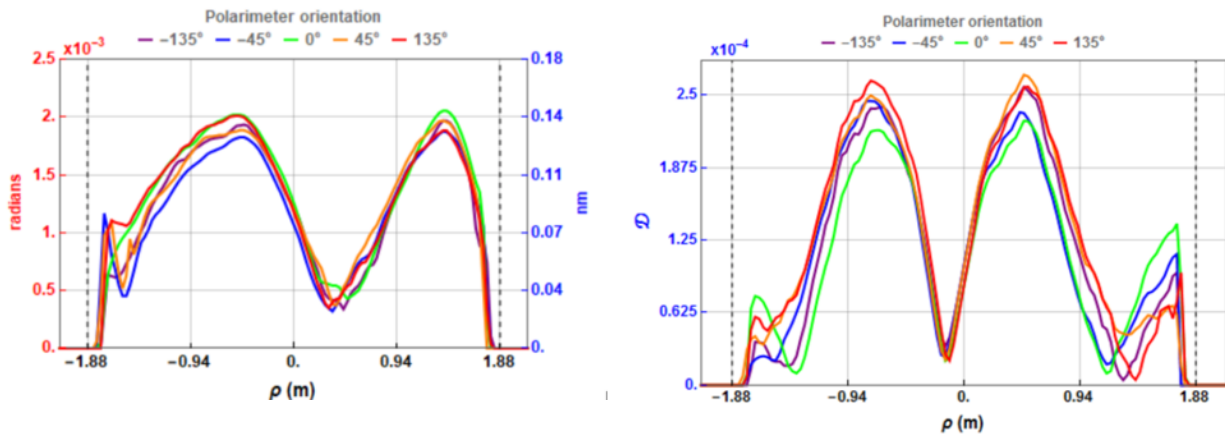
Figure 7-3: Profiles of the retardance and diattenuation as measured across the 3.75-m sphere, aluminized in the same manner at the 4-m Mayall astronomical telescope (see Appendix A). These are maps of the polarization reflectivity changes across the telescope aperture. One and a half cycles per mirror diameter is the dominate spatial frequency. Figure 7.3 (left) shows radians of phase (scale on the left) created by the birefringence property of the coating as a function of mirror position in the radial coordinate of ρ in units of meters. The scale on the right is in units of nm, calculated to compare with the OPD allowable tolerance value of ~50-pm calculated by Green and Shaklan[111]. The orientation of the scanning polarimeter across the mirror surface was stepped from -135o to +135o in units of 45o to investigate possible systematics. No significant systematic terms were found as can be seen examining the contents of Fig. 7-3 (left). Figure 7-3 (right) shows the values of diattenuation of the coating as a function of mirror position in the radial coordinate of ρ in units of meters. The scale shown on the left shows values between 0.6 and 2.5 time 10-4 and the function has two cycles over the mirror, not quite matching the structure shown in the birefringence.

7.5   DESCRIPTION OF DATA

To help clarify the various stages of data reduction this section outlines the specific data that makes up each stage of the data reduction process. A complete measurement is considered to be one retardance map and one diattenuation map showing the form birefringence of the mirror sample. In total, five complete measurements were acquired with the form birefringence polarimeter rotated

about its axis to view the mirror at different orientations. The following sections will use one of these data sets as a reference at various points. The retardance maps are calculated from a set of 17 minimum reflectance maps. The diattenuation maps are calculated from a set of 17 relative orientation maps. In both cases, the 17 maps relate to 17 orientations of the generator polarizer, 0°, 22.5°,…,360°. Individual minimum transmission maps and orientation maps are calculated from 13 images acquired as the analyzer polarizer steps through 0.8° surrounding its maximum extinction orientation.

Leakage and Orientation Maps – The first data reduction step involves analyzing the thirteen images acquired while the analyzer polarizer rotates 0.8°, from one side of the crossed-polarizer null to the other, creating two mirror maps. The first map describes the maximum leakage between crossed polarizers by determining the ratio of light reaching the detector with polarizers aligned for maximum extinction versus the light at the detector with polarizers aligned for maximum transmission. The second map gives the relative polarizer orientation value at each pixel in the first map. Retardance calculations analyze the first map and diattenuation calculations analyze the second. The transmission, T, between two linear polarizers as a function of the angle between their polarization axes θ is given by Malus's law,

$$T = \cos^2[\theta]$$

The apparatus works with a null image, where $\theta = \pi/2 + \varepsilon$, the transmission varies with ε^2 for $\varepsilon \ll 1$. The raw images are the transmission through two linear polarizers as ε varies from -0.007 to 0.007 radians in 13 steps. On a pixel by pixel basis, the relative polarizer orientations are paired with transmission readings and fit to a quadratic,

$$T = a\theta^2 + b\theta + c,$$

giving orientation θ_{Pol} and transmission T as,

$$\theta_{Pol} = \frac{-b}{2a}$$

and

$$T[\theta_{Pol}] = -\frac{b^2}{4a} + c$$

The quadratic fitting completes the process of reducing the raw images to the relative orientation maps. However, the minimum transmission maps must be referenced to the maximum transmission to provide meaningful information for calculating retardance. To maintain fully automated scan software the maximum transmission map is calculated based on the same 13 images used to calculate minimum transmission map. The maximum transmission is given by the peak amplitude of the $\sin^2$ function. Looking at the series expansion of sine squared,

$$a_0 \sin^2[a_1 x] \approx a_0 a_1 x^2$$

Since the value of a_1 is known, the maximum value of the sinusoid a_0 can be determined from the quadratic coefficient a. In the case of rotating polarizers, $a_1 = 1$ so $a_0 = a$. This allows for the referenced minimum transmission map to be calculated without any addition measurements as,

Equation 7-1

$$\frac{T_{Min}}{T_{Max}} = -\frac{b^2 - 4ac}{4a^2}$$

Figure 7-6 shows the maximum transmission calculated by this approach.

Alternatively, the maximum transmission can be obtained by rotating the analyzer polarizer 90° from the minimum orientation. This approach would result in an off-axis ray transmitting along a different region of one of the polarizers for the maximum transmission image compared to the maximum extinction image. This could lead to polarizer apodization affecting the calculated transmission ratio. Obtaining the maximum transmission image also creates issues in the data acquisition process. The form birefringence polarimeter uses long exposure times to increase the signal to noise near the null. The detector starts to saturate within 1° of the null configuration. The form birefringence polarimeter does not include a filter wheel or any other method to modulate the light source intensity and the camera exposure cannot be set to a low enough value to prevent saturation with parallel polarizers. Obtaining maximum transmission images would require human intervention regularly over the hours-long measurement. This would make the process unsuitably labor intensive and this approach was not used.

This completes the first step of the analysis and reduces the first 13 raw images to a referenced minimum transmission map and a relative polarizer orientation map. This step is repeated for each of the generator polarizer orientations (0°, 22.5°,…, 360°) resulting in 17 of each map. One complete data set is shown in **7-4.**
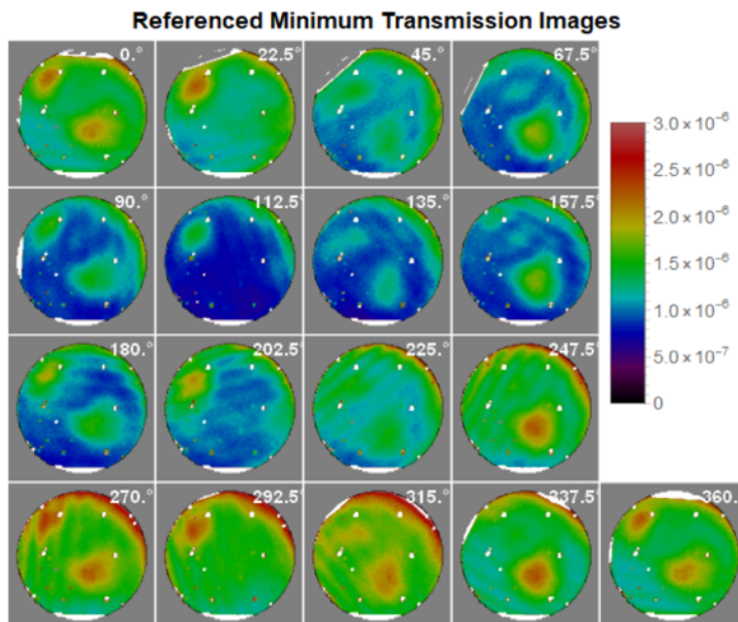
Figure 7-4: Referenced minimum leakage maps for 17 generator polarizer orientations used for instrument calibration. Transmission, shown with the color scale at the right varies from 3x10⁻⁶ down to 0. The angle in the upper right of each image gives the generator polarizer orientation. The value being plotted is the minimum transmission relative to the maximum transmission. The leakage due to retardance is expected to be 90 degree periodic so similarities along columns of the figure are important.

Figure 7-4 shows the 17 reduced minimum transmission maps for generator angles of 0°, 22.5°, … , 337.5°, 360°. Each map gives the minimum polarimeter transmittance assuming the analyzer polarizer is at the optimal extinction angle for each individual pixel. The transmission under this condition is related to linear retardance or circular diattenuation. If linear retardance were the source, the transmission would be 90° periodic in generator rotation. The maps in **Figure 7-4** are arranged so that 90° periodicity would appear as similarities in all the images in a column. This is clearly present in **Figure 7-4**, for example, the bright spot in the upper left region of each image in the second column. This data will be further reduced to determine the linear retardance.

Relative Orientation Maps (°)
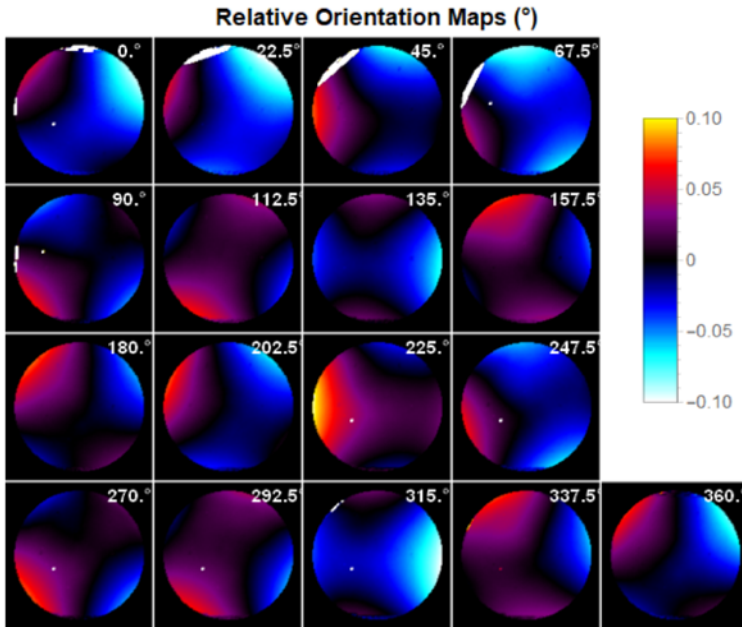
Figure 7-5: Relative orientation maps for 17 generator polarizer orientations. Units are in degrees and the average orientation has been subtracted. The value plotted is the angle in degrees at which the minimum transmission occurred with the generator angle subtracted and 90 degrees added to center the data around 0.

Maximum Transmission Images
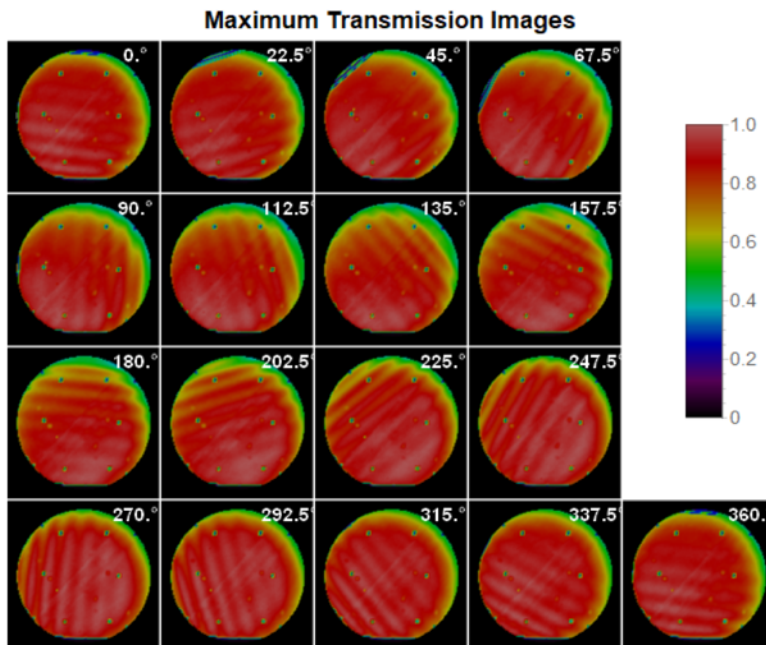
Figure 7-6: Maximum transmission image calculated from scan through extinction.

Figure 7-5 shows the complimentary orientation data to the transmission data shown in **Figure 7-6**. Each map gives the angle of the analyzer polarizer for each pixel required to produce the maps shown in **Figure 7-6**. The generator angle plus 90° has been subtracted from each map so that they can be plotted on the same scale. In the polarimetry section it was shown that this orientation was related to linear diattenuation in the sample and that the angle would modulate with a 180° period with rotation of the generator. The maps in **Figure 7-5** show that there is considerable angular information present in the data and that there is certainly a 180° periodic component, seen by observing similarities in every other image in a column. However, most of the orientation in **Figure 7-5** is caused by the field dependence of the Glan-Thompson polarizers, so very little can be ascertained without further reducing the data.

Figure 7-6 shows the maximum transmission maps. In **Figure 7-4**, the bright region on the left side of the 22.5° image, vanishes in the 67.5° image, reappears at 112.5°, and continues that pattern through the remaining images. The bright region on the right side of the 67.5° image modulates with the same frequency but different phase. The relative orientation images in **Figure 7-5** also exhibit periodic behavior. The visually apparent periodicity is caused by the rotation of the hyperbolic paraboloid-shaped field dependence found in each map. This is the expected behavior due to the field dependence of the Glan-Thompson polarizers. Any relative orientation chances caused by mirror diattenuation must be separated from this much larger

orientation signal. The following sections discuss the retardance calculation from 17 minimum transmission images and the diattenuation calculation using 17 relative orientation images.

7.6   RETARDANCE

This section explains the process to reduce the 17 images in **Figure 7-4** to a single map of the mirror's linear retardance. The polarimetry section showed that for a low polarization sample, the minimum leakage between polarizers is related to the sample's linear retardance, circular diattenuation, and retardance orientation. The dependence on retardance orientation causes the minimum transmission due to linear retardance to modulate with a period of 90° as a pair of crossed polarizers rotate. Any transmission caused by the unlikely presence of circular diattenuation is independent of polarizer orientation and doesn't modulate, and can still be separated in the data reduction process.

The discrete Fourier transform (DFT) provides a straight forward method to calculate to retardance from the minimum transmission images. The data is prepared by averaging the 0° and 360° images so that the data set runs from 0° to 337.5°. The images are then arranged into an array of dimensions 512 x 512 x 16. The DFT is performed on the 16-element list obtained by indexing the first two dimensions of the array. For a purely linearly retarding sample the Fourier transform will have three non-zero elements. The $+/-$ 4th harmonic component contains the 90° period signal and the 0th harmonic contains the DC signal that occurs because minimum leakage is always greater than 0. **Figure 7-7** shows the first five DFT coefficients of the minimum transmission maps. The black circle drawn over the maps illustrates where the mirror's edge should be. A section of the map along the upper left edge retuned retardance values much larger than the rest of the map, significantly off the color scale used in the plot. The issue occurs because those pixels saturate in some of the minimum transmission images, as can be seen in **Figure 7-4** in a number of images, 67.5° being one of the most pronounced. The saturation occurs when the angle of incidence at the Glan-Thompson's hypotenuse is too low for the ordinary mode to experience total internal reflection (TIR). For these fields, the Glan-Thompson's diattenuation drops to approximately 0 and the corresponding pixels saturate. Since the field of view depends on the angle on incidence at the hypotenuse surface, it is asymmetric about the Glan-Thompson's center axis in the plane of incidence of the hypotenuse. It is symmetric about the center axis in the plane containing the center axis and normal to the plane of incidence. The asymmetry varies with wavelength due to dispersion of the crystal and cement materials used in the Glan-Thompson. These effects can significantly reduce the useful symmetric field of view to a fraction of the full asymmetric field.

Leakage 0th–5th Frequency Components From DFT
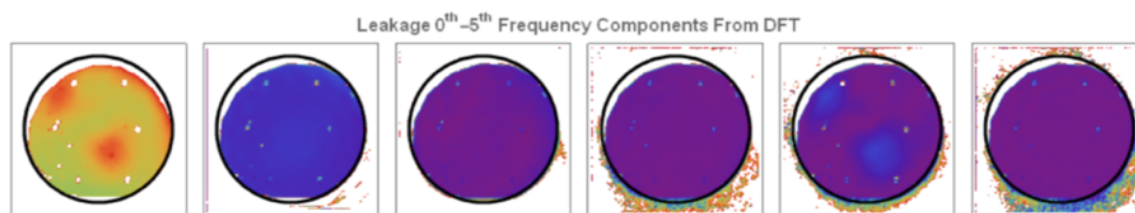
Figure 7-7: First five terms of the DFT calculated using 16 images per pixel. There is a clear spatial variation in the 4th harmonic which is repeated in the 0th harmonic due to the positive nature leakage. The other fourth harmonics look approximately uniform. The black circle shows where the mirrors edge should be. There is a fairly large region with no data in the upper left part of the mirror.

Figure 7-7 shows the first six components of the discrete Fourier transform (DFT) of the transmission images from **Figure 7-4**. Assume each pixel is indexed $p_{i,j,n}$ where i, j, and n refer to row, column, and map respectively. The DFT is performed for each row and column on the list $p_{i,j,n}$ with n = 1, 2, …, 15, 16. The 17th image has the same generator angle as the first image so it is not included. Linear retardance is expected to cause 90° periodic modulation of the transmission, so the image second from the right in **Figure 7-7** is of most interest. While most of the harmonic components are mostly uniform there is a clear spatial structure to the 4th harmonic. This will be used to calculate the linear retardance present in the mirror.
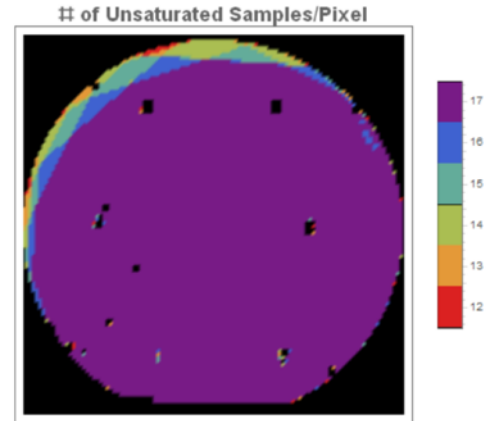
Figure 7-8: A graphical representation of the number of pixels used in the non-linear curve fitting for each pixel index. Most of the pixels are in the red level, meaning all 17 data points are available for extracting the retardance.

The wavelength of 450 nm was chosen to reduce field of view asymmetry while maintaining enough source power and detector quantum efficiency. This increases the symmetric field of view of each Glan-Thompson to slightly smaller than the angle subtended by the mirror. The polarizers are aligned so that for most generator orientations the entire mirror falls in the usable field, but limited flexibility in the polarizer fixturing made occasional saturation unavoidable. The nominal sample rate used while rotating the generator polarizer was twice the Nyquist frequency for the highest frequency of interest. As long as there are not too many saturated pixels, they can be rejected while maintaining a sufficient sample rate to reconstruct the signal. **Figure 7-8** shows the number of samples per pixel after rejecting saturated pixels. Over most of the mirror all 17 samples were unsaturated, but at the top left edge there are a small number of pixels where only 12 samples were used. Due to the non-uniform sampling caused by rejecting bad pixels, the Fourier coefficients are calculated by directly fitting the data to the sine-cosine Fourier series.

Figure 7-9 provides the same information as **Figure 7-7**. The data reduction process was altered to improve the coverage of the mirror. After saturated pixels were removed the data was no longer a regular array. For each row and column, the list of available pixels was directly fit to the Fourier series to determine the frequency components. This results in similar maps to **Figure 7-7** but with slightly better coverage of the mirror.

The retardance magnitude is calculated from the peak value of the transmission attributed to retardance. The source of transmission is determined by the frequency of the signal as the polarizers are rotated through 360°; retardance caused transmission has a 90° periodic signature. Since
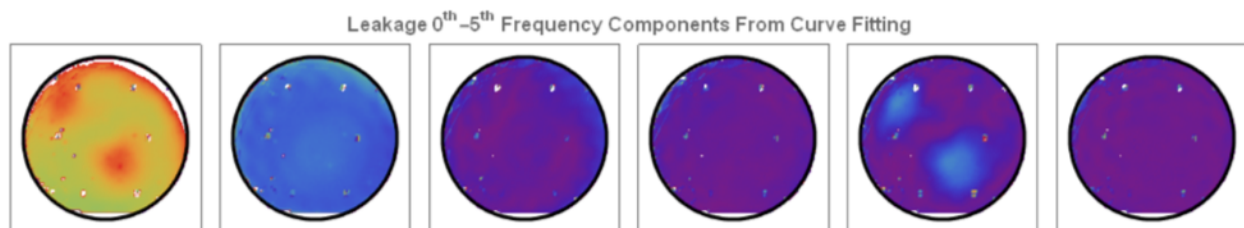
Figure 7-9: The 0th through 5th harmonics of the leakage signal. There is background leakage seen in the 0th harmonic and 90° periodic leakage in the 4th.

transmission is always greater than 0, half of the retardance leakage amplitude appears in the zero-frequency component. Recognizing that the 4th harmonic is,

$$a_4 \cos(4\theta) + b_4 \sin(4\theta)$$

Equation 7-2

we find that the retardance, $\delta,$ will be,

$$\delta = 2\sqrt{2A_4} \text{ radians where } A_4 = \sqrt{a_4^2 + b_4^2}$$

Equation 7-3

This is the same result calculated in the polarimetry section with an additional $\sqrt{2}$ to account for the amplitude appearing in the DC term.

7.7   DIATTENUATION

Calculating the diattenuation from the orientation images is considerably more involved than the retardance procedure. The orientation maps do not provide an absolute reference like the leakage maps. The polarizer rotation stages do not have the absolute accuracy to relate the orientations from one generator polarizer angle to the next. For each individual generator configuration, the polarizer motor steps through the scan and the relative orientation between the pixels can be determined more precisely. This means the data reduction process needs to estimate the average angle from one generator orientation to the next. This requires an assumption about the diattenuation at some point on the mirror. Due to these limitations the form birefringence polarimeter is insensitive to spatially uniform diattenuation at the mirror. The data reduction software also needs to separate the orientation due to diattenuation from other sources of orientation variation present in the measurements. This is challenging because the field dependence of the Glan-Thompson polarizers causes significantly more orientation variation in the maps than the diattenuation. A Glan-Thompson polarizer model was developed and fit to the data using free parameters related to the possible tilts of the polarizer.

7.8   UNIAXIAL CRYSTALS AND GLAN-THOMPSON POLARIZERS

Glan-Thompson polarizers take advantage of the birefringent nature of uniaxial crystals to separate incident light by polarization[112],[113],[114],[115]. The particular advantage of a Glan-Thompson crystal polarizer is their very high extinction ratio: 10^{-6}. **Figure 7-10** shows the basic layout of a Glan-Thompson polarizer. The polarizer is comprised of two identical wedges of α-BBO, a negative uniaxial material, cemented together such that both crystal axes are parallel to the entrance and exit faces and parallel to the diagonal face. Light entering the polarizer splits into ordinary and extraordinary modes which propagate to the cement interface. The cement and wedge angles are selected so that the ordinary ray experiences total internal reflection and the extraordinary ray transmits with minimal reflection loss. The reflected ordinary ray is usually absorbed at the top side of the prism. The extraordinary ray refracts into one ray in the isotropic cement layer, and then refracts into two modes in the second crystal. The eie mode is the intended exiting polarization state (Bass, Decusatis, & Enoch, 2009).[116]

Lam analyzed a Glan-Taylor polarizer in considerable detail, especially in the description of its field of view, mode coupling, and field dependent contrast[117]. Glan-Taylor polarizers replace the cement with an air gap making them suitable for higher power applications but reducing the field of view. While the field-of-view properties of the Glan-Taylor will not be quantitatively relevant to Glan-Thompson polarizers, Lam's qualitative observations are useful. Lam modeled the intensity in each of

Figure 7-10: Glan-Thompson polarizer. The optic axis points into the page. The large angle of incidence at the diagonal allows the o- mode to experience TIR while the E mode transmits into the cement layer and then out through a second uniaxial material.

the four modes exiting a single Glan-Taylor Prism; eie, oio, eio, and oie, and identified the eio mode as the largest undesirable mode contribution. Fortunately, the large distance between the form birefringence polarimeter's polarizers and the sample mirror ensure that any mode-coupling occurring at the polarizer hypotenuse will not reach the mirror. Of the modes identified, only oio has the potential to reduce the form birefringence polarimeter performance and can be reduced to very near zero with proper alignment. More relevant than individual mode analysis is the discussion and modeling of the Glan-Taylor's contrast[112].

Lam defines the extinction ratio as the transmittance through two perfectly aligned parallel Glan-Taylor polarizers divided by the transmittance through perfectly aligned orthogonal Glan-Taylor polarizers. Lam found a Maltese cross-shaped region of high contrast which falls off quickly with tilts about any axis other than x or y. The eieieie mode contributed the most intense leakage. The other leakage modes identified were coupled modes that would miss the detector of the form birefringence polarimeter. The leakage calculated for the eieieie mode, of 0.00035, is about 350 times larger than the maximum retardance leakage signal observed with the polarimeter. This seems to suggest the form birefringence polarimeter's polarizers perform better than the theoretical Glan-Taylor polarizers modeled by Lam. The eieieie mode only occurs in Lam's simulations for off-axis propagation. It occurs when the e mode leaving the first polarizer does not couple completely into the o mode of the second polarizer. Rotating the second polarizer to the correct angle would allow full coupling of the e mode to the o mode, with each off-axis field requiring a slightly different rotation. The form birefringence polarimeter accomplishes this by its procedure of taking images while stepping through the crossed polarizer null to determine the minimum transmission for each pixel. This also means that while this leakage mode did not impact the retardance measurement or data reduction, it causes a polarizer orientation effect that must be separated from diattenuation[112].

7.9   GLAN-THOMPSON POLARIZERS AND ORIENTATION IMAGES
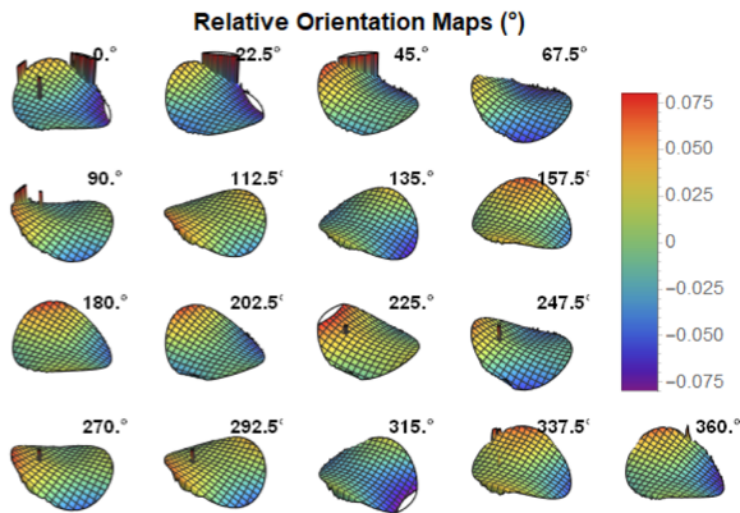
Figure 7-11: Orientation maps for one complete dataset. This is the same quantity as **Figure 7-5** which can be referred to for scale.

Figure 7-11 shows an example of the list of orientation maps that are contained in each complete dataset. The predominate feature of the orientation maps is always the same, the hyperbolic paraboloid rotating with the analyzer angle. The maps also have tilt terms with various θ dependence. There is not an absolute reference to help calibrate the data reduction process and the orientation. The limited accuracy of the rotation stage over large moves means the individual maps are only self-referenced. To deal with the stage accuracy issue it is assumed that the mirror does not have a uniform component of diattenuation. The data reduction models Glan-Thompson orientation maps and removes them from the measured orientation maps. When possible, relationships between fit parameters from one map to the next are developed to reduce the total parameters used in the Glan-Thompson model.

Figure 7-12: a. Shows intensity measurements acquired as the analyzer polarizer stepped through the cross-polarizer orientation. **b.** Polaris-M model simulation of the measurement performed at different analyzer angles. The set shows a well aligned system, i.e. no retarder tilt.

Before moving into the model, consider what is observed in the orientation maps. **Figure 7-12-a** shows raw intensity images acquired for 0° generator angle as the analyzer stepped from 89.6° to 90.4°. The image at the bottom of the stack was the first image acquired and the image at the top of the stack was the last image acquired as the analyzer rotated through extinction. The leakage image can be approximated by taking the darkest regions from each image in the stack and stitching them together. The orientation is determined by how far up the stack of images the smallest values occurs for each pixel. The quadratic curve fitting makes this discrete process continuous.

The form birefringence polarimeter was modeled in Polaris-M to create simulated intensity maps of the process of stepping the analyzer through extinction. Different tilts were applied to the model's Glan-Thompson polarizers to investigate their effects on the orientation images. The first set of simulated data, **Figure 7-12-b,** was generated using well aligned Glan-Thompson polarizers. The simulation was repeated at different initial generator and analyzer rotation angles. For the 0°

analyzer angle simulation, the bottom has nearly complete extinction at the left and right edges of the map shown by the black color. Moving up the stack the black regions move towards the center until a black "x" crosses the image. The black regions then separate and move out of the field of view at the top and bottom edges of the image. The orientation map, formed by the height in the stack at which each pixel experienced extinction, has the hyperbolic paraboloid shape seen in the measured orientation maps. The orientation of the hyperbolic paraboloid rotates with the polarizers.

Figure 7-13 shows additional simulations performed for various types of Glan-Thompson alignment errors. Beginning with the bottom simulation; moving up these stacks a dark line moves across the images from the front left of the bottom image, to the back right of the top image. The orientation map formed by these images will be dominated by a linear component. As the analyzer rotates the images structure does not, so the polarizer errors shown in this image will manifest as a constant tilt term in the orientation images.

Moving up to the middle row of **Figure 7-13** these images also result in an orientation map dominated by a linear term. But looking at the stacks from left to right, the structure in the images rotates with analyzer angle. The Glan-Thompson polarizer field dependent orientations modeled here will appear as a 360° periodic tilt term in the orientation images.
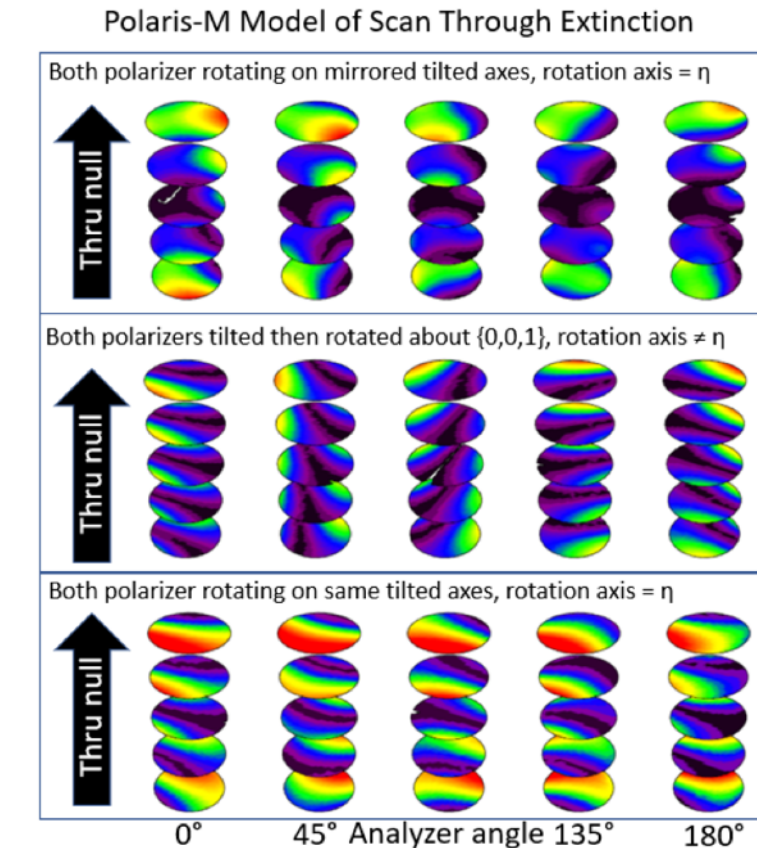
Figure 7-13: Additional simulations with different types of polarizer tilts.

The top row of **Figure 7-13** is not as clear as the first two. In the first stack of images the extinction starts at the back, right edge and moves towards the front, left edge. The orientation image has a small tilt term combined with the hyperbolic paraboloid seen in the well aligned case. Moving left to right through the images, the small tilt component rotates twice as fast as the analyzer. This can most easily be seen by looking at the extinction in the bottom image of each stack. This type of polarizer error will manifest as a 180° periodic tilt in the orientation images.

7.10   REMOVE ORIENTATIONS DUE TO GLAN-THOMPSON

To summarize the observations from the previous section; (1) the Glan-Thompson polarizers introduce a hyperbolic paraboloid shape to the orientation image, (2) this shape rotates with the polarizers, (3) tilts to the polarizer move the hyperbolic paraboloid off axis, (4) a polarizer

that's tilted relative to the rotation axis of the stage such that it wobbles, will produce a shift in the orientation image that rotates with the polarizer, (5) polarizers rotating about tilted axes will either cause a shift in the orientation that rotates with twice the polarizer orientation or a stationary shift depending on the relationship between the generator and analyzer rotation axes. All of these effects can be modeled using Zernike's polynomial terms for tilt and astigmatism. Piston is also included since the form birefringence polarimeter cannot measure constant diattenuation. The fitting will be performed directly on the orientation images.

There are 17 orientation images for each dataset and fitting them all individually increases the likelihood of losing diattenuation orientation information to one of the Zernike terms. Figure 7-14 shows the results of fitting Zernike's to 17 orientation maps using the simulation from before. The x-axes of these plots correspond to analyzer angle. At each analyzer angle the orientation image is parameterized by piston, tiltx, tilty, oblique astigmatism, and vertical astigmatism. Clearly these parameters are not independent from one analyzer angle to the next. For example, the astigmatism for the entire dataset does not require (two astigmatism parameters) x (17 images) = (34 parameters). The astigmatism term depends only on the polarizer properties and the orientation of the pair of polarizers. The amplitude of the astigmatism is constant but it switches between oblique and horizontal with twice the frequency of polarizer rotation. Over the 17 images the astigmatism can be described with just an amplitude and a phase offset if the correct modulation is built into the model. The linear components are treated similarly. Since there are three linear components from the different possible tilts, (DC, 1θ, and 2θ), this leads to six parameters to describe them resulting in eight total parameters.
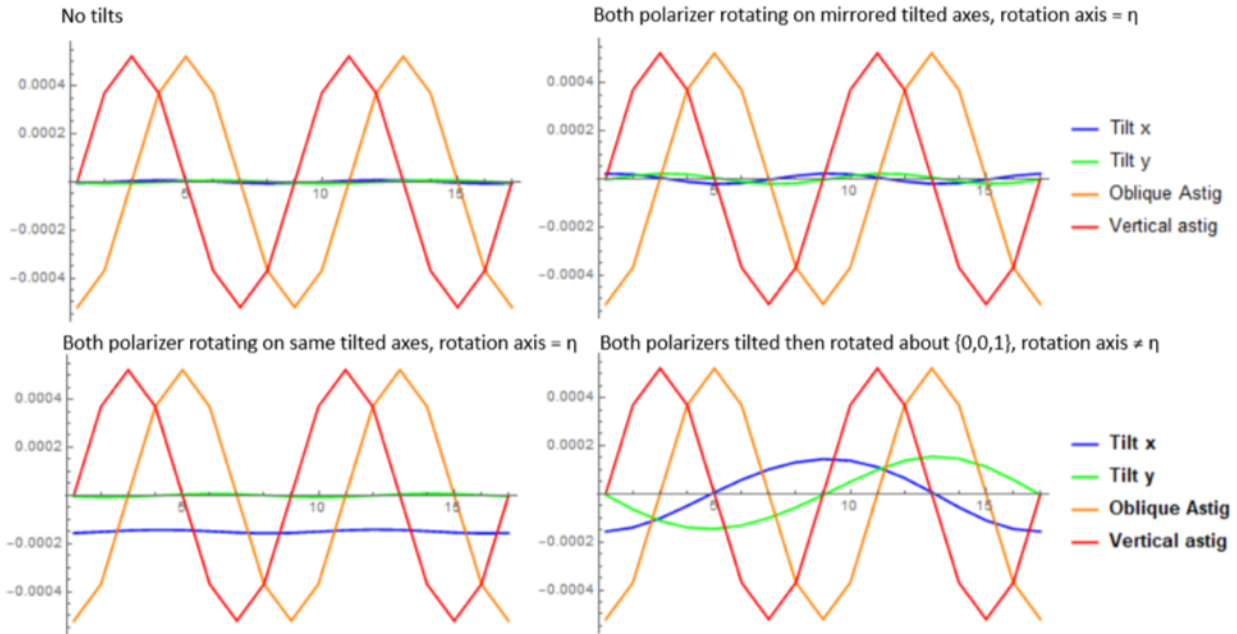
Figure 7-14: Zernike fits to the simulations for different polarizer tilts.

The set of Zernike terms are given below.

<div align="right">**Equation 7-4**</div>

$$GT\ Model = a_0 + a_1 z_1^{-1} + a_2 z_1^{1} + a_4 z_2^{-2} + a_5 z_2^{2}$$
$$a_4 = a_{astig} \cos\left(2\theta - \phi_{astig}\right)$$
$$a_5 = -a_{astig} \sin\left(2\theta - \phi_{astig}\right)$$
$$a_1 = \sum_{k=0}^{2} a_{tilt,k} \cos(k\theta - \phi_{tilt,k})$$
$$a_2 = \sum_{k=0}^{2} a_{tilt,k} \sin(k\theta - \phi_{tilt,k})$$
$$\theta = \frac{\pi}{8}n \quad n = 0,1,2,\dots,16$$

Figure 7-15 shows the results of applying the model to five complete datasets. The datasets correspond to measurements at various system orientations. The astigmatism parameter is constant across the measurement as expected. The tilts change by small amounts between measurements which is expected. The polarizers had to be adjusted for each configuration to try to optimize the field of view. The parameters will be plugged into the Glan-Thompson model to create masks for each dataset. The masks will be subtracted from their orientation images isolate possible diattenuation effects on orientation.
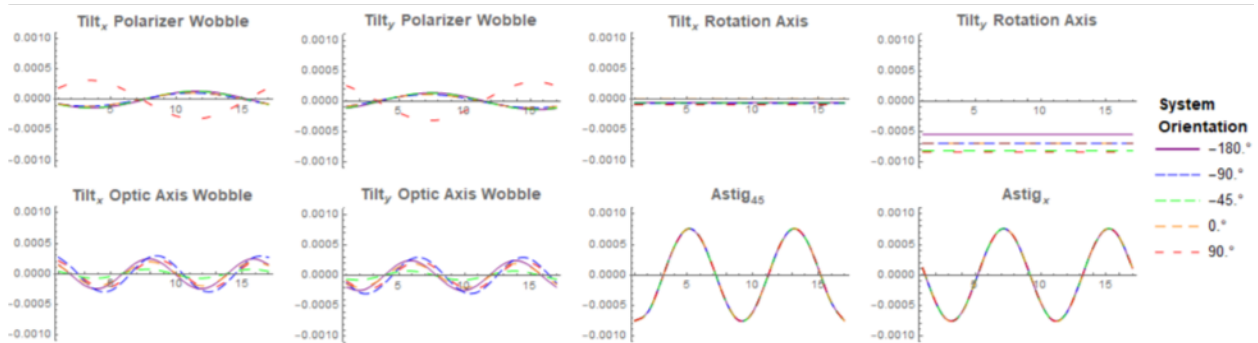
Figure 7-15: Best fit parameters for 5 complete datasets at different instrument orientations.

Diattenuation orientation will not take a tilt-like form. There is no diattenuation offset or piston-like term. All piston was removed from orientation maps prior to fitting because the rotation stage motors did not maintain enough accuracy over large motion angles to use their values finely compare orientations between different generator angles.

1.1.8 *CALCULATE DIATTENUATION*

Figure 7-16 shows the orientation images after attempting to remove the polarizer effects. The final step is to perform the harmonic analysis on the orientation images and convert the correct frequency component to diattenuation. **Figure 7-17** shows the harmonic analysis of the orientation image. The second harmonic, where we expect to find orientation due to diattenuation, shows a clear signal while all other frequency components are near zero.
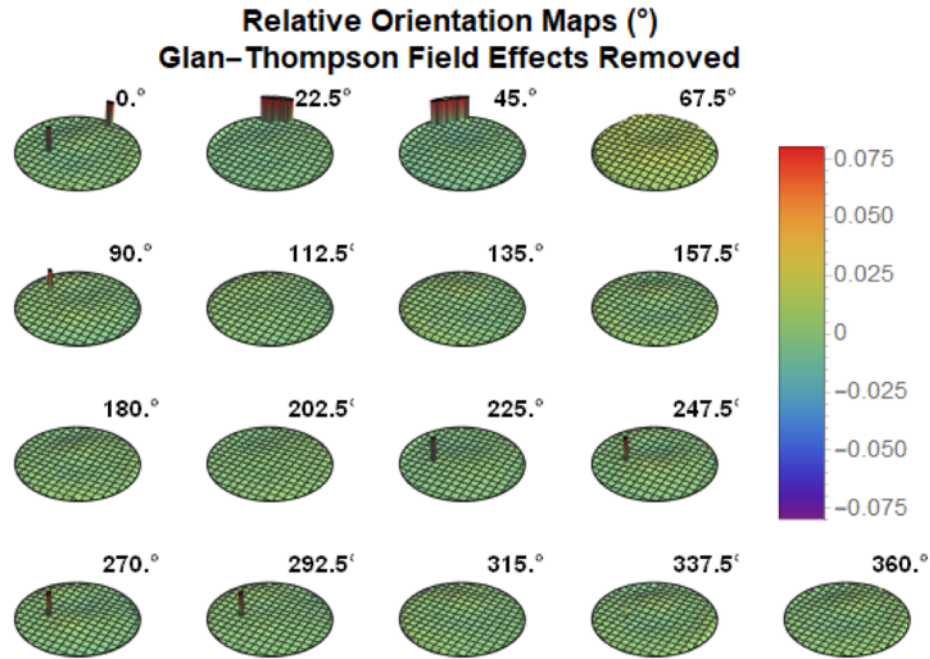
Figure 7-16: Orientation images after removing contribution from Glan-Thompson polarizers.
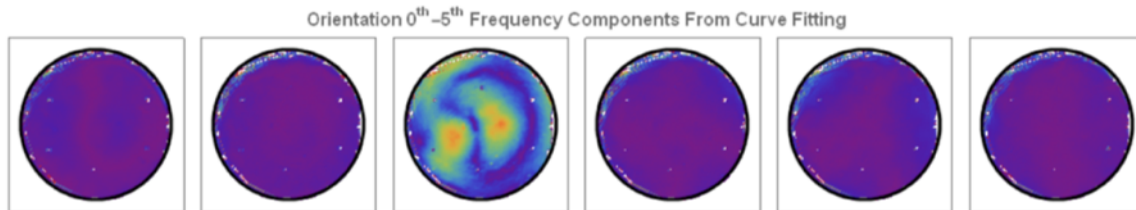
Figure 7-17: Harmonic analysis of one complete set of orientation images. The second harmonic shows a distinct pattern while all other frequency components show no signal.

1.1.9   *TEST METHOD WITH SIMULATED DATA*

Simulated orientation data was created to test this data reduction method. The simulated orientation maps were created by modeling the experiment in Polaris-M. A 2-D distribution was chosen for the diattenuation and entered into the model as pure diattenuator Jones matrices. The full sequence of measurements was simulated by running a new ray trace for each one. Curve fitting the raw images produced the leakage and orientation maps.
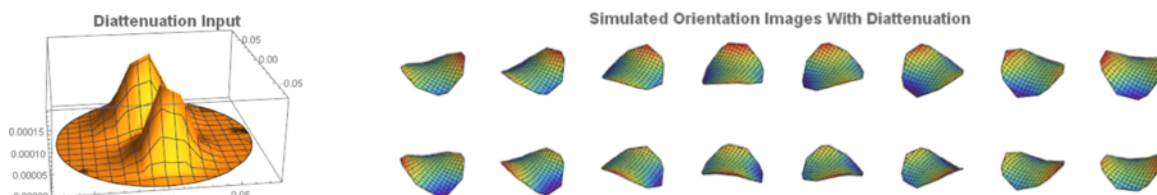
Figure 7-18: Left. The mirror diattenuation used in the simulation. **Right.** The orientation maps after the diattenuation is added. The rotation caused by diattenuation is small enough that it cannot be easily seen in the orientation maps.

Recoved vs Input Diattenuation
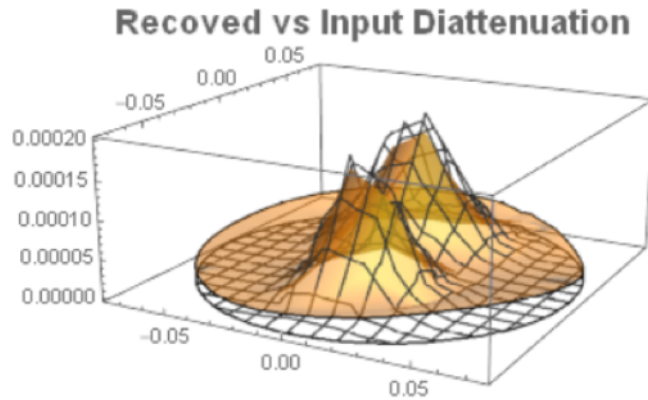
Figure 7-20: The recovered diattenuation (orange) vs the input diattenuation (mesh). There is an offset in the recovered diattenuation that is not present in the input. The recovered diattenuation also has lower peak values than the input.

Recoved vs Input Diattenuation
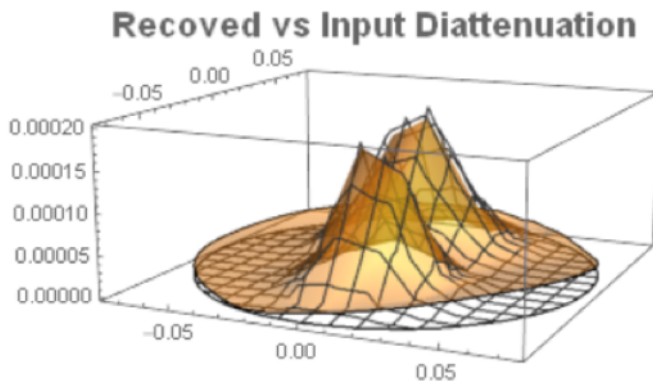
Figure 7-19: Modified data reduction approach where assumptions are made about the perimeter values of the sin and cos frequency components.

Prior to fitting the orientation maps to the model, the piston was removed from each map separately. This follows the process required for measured data due to limited rotation stage accuracy. Curve fitting is performed to find the eight parameters from the previous section. The Glan-Thompson orientation is calculated for the same fields as the simulated data and then subtracted from it. Harmonic analysis is performed on the result and the 180° periodic component is taken as the orientation due to diattenuation. **Figure 7-20** shows that the diattenuation recovered by this method generally reproduces the main features of the input map but does not return accurate values. The accuracy can be improved with a priori knowledge of the input diattenuation map. For example, **Figure 7-19** shows the results obtained by assuming the outer perimeter of the sine and cosine frequency components have zero diattenuation and shifting them appropriately prior to taking their root-sum-square. This step slightly improves the performance in this case. Without a priori knowledge of the mirror the results of the diattenuation data reduction should be taken as qualitative.

1.1.10 *SEPARATING MIRROR SIGNAL FROM SYSTEMATIC EFFECTS*

All measurements in this section were performed at 450 nm. To distinguish between properties of the mirror and potential systematic effects, multiple measurements of the same mirror were performed with the form birefringence polarimeter rotated about its axis. Artifacts caused by the form birefringence polarimeter itself will appear stationary as it rotates. Mirror properties will rotate relative to the form birefringence polarimeter detector by remaining stationary on the mirror.

Figure 7-21 and **Figure 7-22** show that the features measured are indeed stationary with physical position on the mirror even as the polarimeter rotates. The magnitude of retardance and diattenuation measured was quite small, 0.002 radians of retardance and diattenuation of 0.00025.
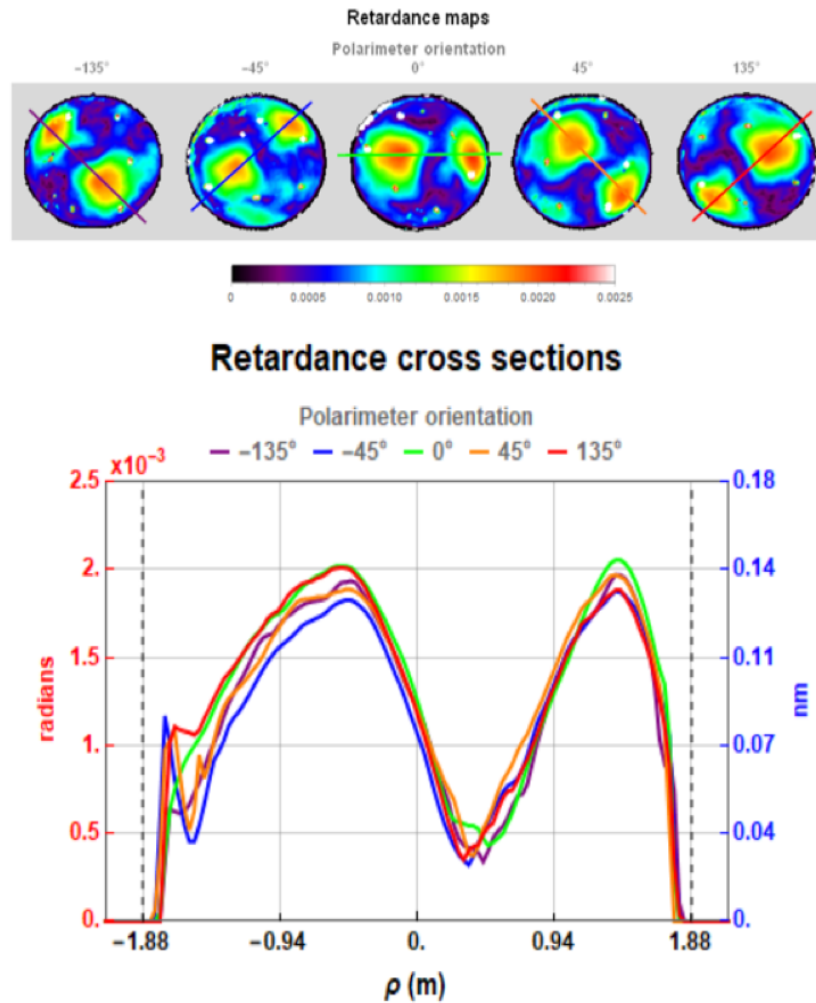
Figure 7-21: Retardance maps acquired with five different polarimeter orientations.

The figures each include the same five complete measurements. The five spatial maps show the mirror properties from the rotating reference frame of the polarimeter. Similarly placed cross sections from each measurement are plotted together also. The retardance is an order of magnitude larger than the diattenuation using the leakage between crossed polarizers metric.
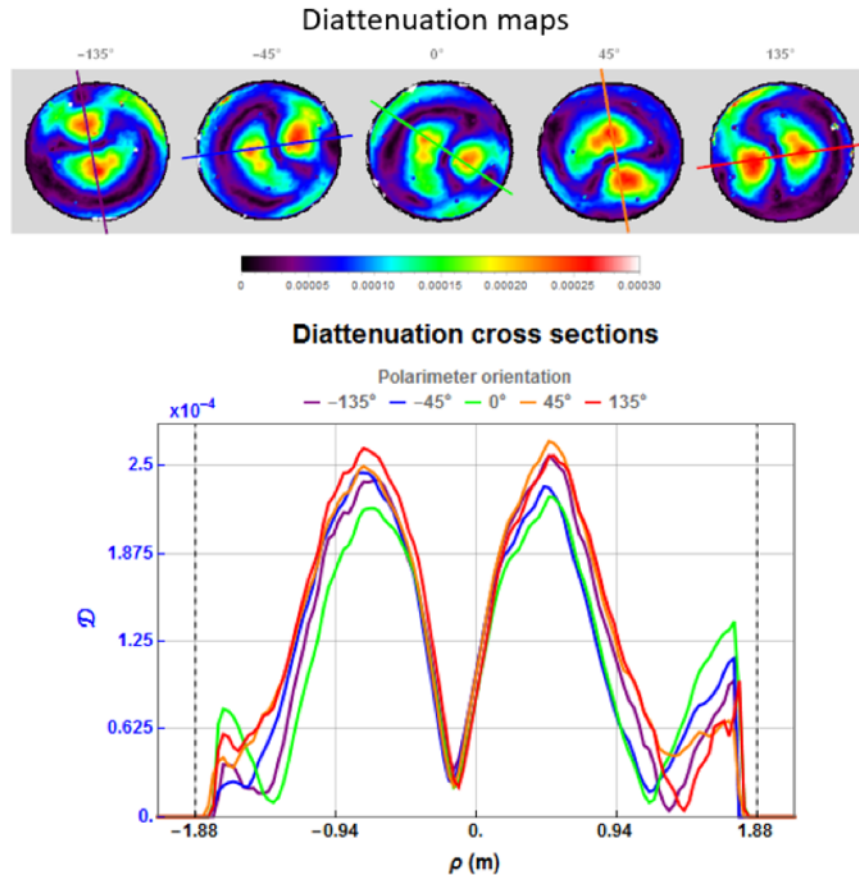
Figure 7-22: Diattenuation maps acquired with the polarimeter at different orientations.
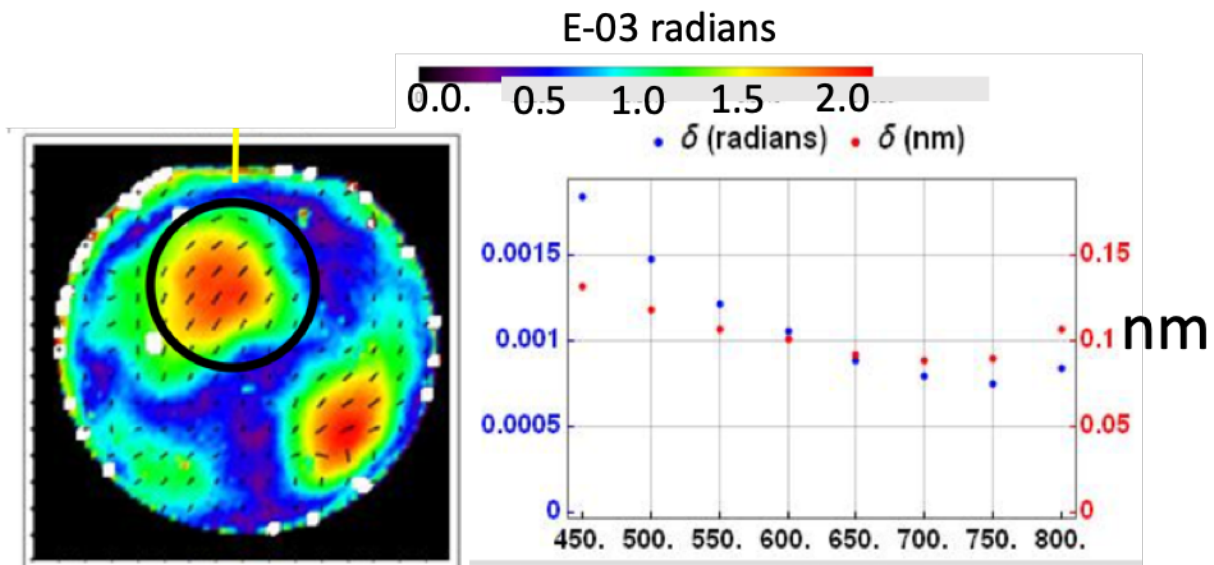
Figure 7-23: Left color-coded form birefringence map of the 3.75 meter test sphere with an Al standard astronomical coating that is used on the Mayall 4-m telescope at KPNO. Birefringence varies from 0 to 2 milliradians. **Right** shows birefringence in radians as a function of wavelength in nm from 450 to 800 nm as measured.

8   HABEX CONTRAST MODELED WITH "REAL-WORLD" COATINGS

In this section we model an estimate of the HabEx system performance as a coronagraph assuming that the system employs a "typical" large aperture primary mirror whose polarization characteristics are those of the 3.75-m mirror whose measurements were presented in the previous section. NASA HQ awarded $26K to JPL to assist us in optimizing the HabEx A/O system by revealing device specifications and providing a software transfer function (FALCO). Unfortunately JPL was unable to provide this data. We inserted the baseline design coronagraph, but used flat deformable mirrors because we could not get timely support from JPL to help us with FALCO to model the A/O system correctly.

Contrast is a metric that describes the optical system's suppression of the on-axis starlight which forms the PSF. The definition of contrast usually involves radial averages over a given annulus in the PSF[118]. Smaller values for contrast indicate that more of the parent starlight is eliminated by the coronagraph.

Dr. Jeff Davis, 2019 (PhD dissertation titled: Polarization aberrations in coronagraphs, 227 pages, University of Arizona, Tucson AZ.) modeled the polychromatic point spread function for reflection from the primary mirror, isotropic reflection with polarization aberrations included, and polarization aberrations plus form birefringence. He found that the form birefringence causes a clear reduction in contrast from the isotropic case. Details follow in this section.

Figure 8-1 below gives the optical path schematic for HabEx. This schematic shows the flow of radiation through the system. The purpose of the figure is to identify those surfaces where light interacts with matter. Missing is the fact that each optical surface interacts with a three-dimensional complex wavefront. Errors across that wavefront contribute to aberrations in the image. Some of these optical surfaces are curved, others flat and some semi-transparent as is the case for the dichroic beamsplitter. The figure below was prepared to facilitate our discussion of how our polarization aberration computations were performed.
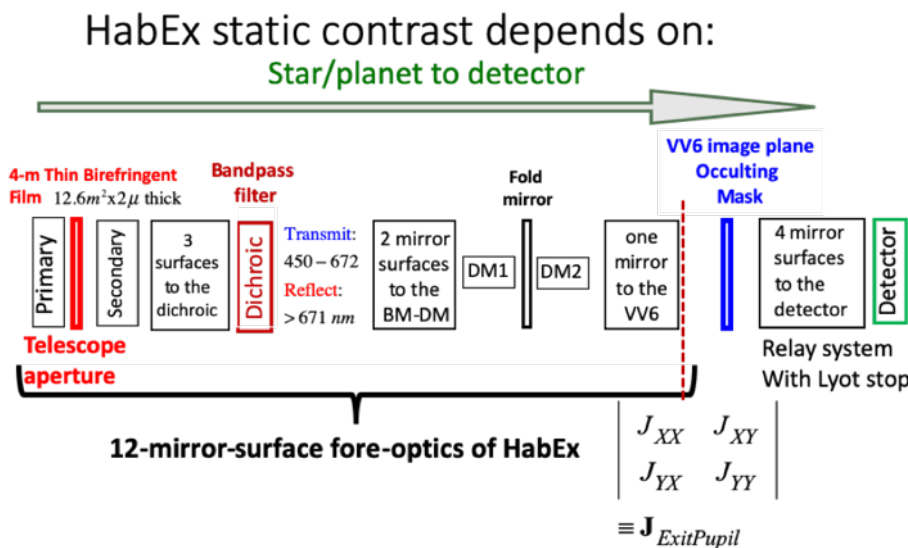
Figure 8-1: Optical path schematic derived from the optical prescription[119] for HabEx from the primary mirror to the detector. A vector Vortex (VV6) mask was used at the image plane of the 12 mirror-surface fore-optics of HabEx. Light from the star/planet at infinity enters the system travelling left to right, first striking the 4-meter off-axis primary mirror which is coated with a 12.6-m² by 2-micron thick metal thin film. The light is reflected to a secondary mirror, then reflects from three surfaces to a dichroic bandpass filter which is designed to transmit 450 to 672 nm and reflect all light > 671 nm. Light passes to reflect from two mirror surfaces to strike a deformable mirror (DM1). It then continues on to reflect from a second deformable mirror (DM2) and then reflects from an additional flat mirror before the radiation falls onto the VV6 occulting mask. After the VV6 occulting mask, the light is relayed by 4 mirror surfaces through a Lyot stop to cast an image of the optical field as modified by the VV6 and the Lyot stop onto the detector.

Dr. Davis divided the optical system into two parts: A and B. The first part A contains the 12-surface fore-optics which transmits the radiation from the primary mirror to the exit pupil that forms the entrance pupil to the coronagraph system, Part B. We calculate the Jones representation of the complex field at this exit pupil surface. We define this to be:

$$J_{ExitPupil} \equiv \begin{bmatrix} J_{XX}(x,y,z) & J_{XY}(x,y,z) \\ J_{YX}(x,y,z) & J_{YY}(x,y,z) \end{bmatrix}$$

<div align="right">

Equation 8-1

</div>

where we have assumed the exit pupil field is on a curved surface, and XX is the electric field in the X-direction out for X-direction polarized light in, and XY is the electric field in the X-direction out for Y-direction polarized light in, etc. J is a complex representation of the electric field with a real (amplitude) and an imaginary (phase) part.

The first surface of the second part B is the vector-vortex starlight suppression occulting mask, which is located at the focal plane of part A. The electric field at this focal plane passes through the occulting mask and into a four mirror optical relay that contains the Lyot stop. The wavefront travels onto the detector, at another focal plane where the modulus squared of the field is recorded as intensity.

We make the reasonable assumption that the system has no nonlinearities in the field propagation. Therefore, the Jones pupils within the system add linearly. The important advantage of this pupil decomposition is that the Jones pupil of each subsystem can be computed from ray-traces without being repeated for various coronagraph designs. This saves computation time.

Spatially varying irradiance at the detector – The spatially varying irradiance at the detector plane depends upon the PSF and the input polarization state. For incoherent sources, such as stars and exoplanets, the irradiance is the sum of the four PSF components. A linear polarizer at the input and another linear polarizer at the output of the system can be oriented in the X- or Y- directions to probe each of the four PSF components. There are four unique orientations for these pair of polarizers: XX, YY, XY and YX. At each orientation of the pair of polarizers the polychromatic thermal (white-light) irradiance at the detector plane is denoted as

$$I(x,y;\lambda) = \begin{bmatrix} I_{XX}(x,y;\lambda) & I_{XY}(x,y;\lambda) \\ I_{YX}(x,y;\lambda) & I_{YY}(x,y;\lambda) \end{bmatrix}$$

Equation 8-2

Here $I(x,y;\lambda)$ is a 2 x 2 real-valued matrix in units of W/m^2. ExoPlanet telescope-coronagraph optical systems require a broad optical bandwidth to obtain enough power for detection, characterization and spectroscopy. Ray-trace programs simulate white-light by ray tracing at intervals across the bandwidth and then sum up the results as shown in the equation:

$$I(x,y) = \frac{1}{K} \sum_{k=1}^{K} I(x,y;\lambda_k).$$

Equation 8-3

In our work here, we use K=18 and λ_k = {450, 453, 456, 460, 469, 475, 478, 492, 500, 503, 510, 517, 525, 528, 535, 540, 546, 550} nm to synthesize thermal white light of uniform radiance from 450 to 550 nm. We will denote the incoherent sum of each polarization sum by a tilde over the symbol for intensity to give:

$$\tilde{I}(x,y) = I_{XX}(x,y) + I_{YY}(x,y) + I_{XY}(x,y) + I_{YX}(x,y)$$

Equation 8-4

To quantify the performance of the coronagraph mask we compare the image plane intensity with the mask, which we denote as: I^M, to the image plane intensity without the mask which we denote as I^O to obtain a normalized polychromatic irradiance $\alpha(x,y)$ which we write as:

$$\alpha(x,y) = \frac{1}{\tilde{I}^O(0,0)} \begin{bmatrix} I_{XX}^M(x,y) & I_{XY}^M(x,y) \\ I_{YX}^M(x,y) & I_{YY}^M(x,y) \end{bmatrix}$$

Equation 8-5

Where $\alpha(x,y)$ is a real valued 2 x 2 matrix that varies across the detector plane and $\tilde{I}^O(0,0)$ is the on-axis polychromatic incoherent irradiance without a coronagraph mask. The normalized irradiance shows the shape of the irradiance pattern at the detector plane and describes its departure from an Airy pattern imparted by the coronagraph.

We polarization ray traced the end-to-end HabEx optical system, including the VV6, but without Falco optimization of the A/O cavity. The polarization ray trace was performed three times, each time under different assumptions: (1) geometric and polarization aberration free, diffraction limited, shown in black; (2) all reflecting surfaces with isotropic coatings, shown in blue; and (3) anisotropic primary mirror using our laboratory measurements with all other surfaces isotropic metal coatings. The output of these three polarization ray-traces is shown in **Figure 8-2**.

Figure 8-2 shows that were the form birefringence properties we measured for the 3.75 meter mirror with its anisotropic astronomy coating placed onto the 4-m HabEx primary, the normalized, unpolarized polychromatic irradiance, $\mathrm{NPI}(\theta)$, also $\alpha(x, y)$ in Equation 7-9 would be approximately 100 times worse than that for mirrors which were coated to give perfectly isotropic coating properties. Form birefringence degrades contrast by a factor of ~100.

A/O correction of birefringence and PSF asymmetry – We were going to determine the extent to which the polychromatic optical cavity A/O given by DM1 to DM2 can correct the form birefringence aberrations present on the primary mirror. We had $26K on contract at JPL to provide consultations on Falco, but, when asked, JPL management reported to our team that no qualified engineer had time to deliver telephone response consulting services to our team at Arizona.

After a few weeks of trying to find JPL support, we called Professor Dimitri Mawet at Caltech and he intervened to help us. Our task delivered the end-to-end optical system HabEx Jones pupils that included our measurement results for a real-world 4-meter class primary mirror with coatings to John Krist and his engineers at JPL.

The extent to which FALCO when used physical parameters of the dual-cavity A/O system with can improve this contrast performance remains to be determined. In addition to minor assistance with the FALCO software we need knowledge of the A/O architecture, actuator density, impulse response, p-p excursion, and mirror reflectivity/scattered light. This work will be proposed for the 2021 opportunity.

The JPL team decided not to use our measured results. JPL calculated polarization for only one polarization direction (X), assumed the coatings were perfectly isotropic, and calculated the mean contrast, which are shown in **Figure 8-3** below copied from Krist, Martin, Kuan, Mennesson, et. al.[120]. The X polarization errors shown in this
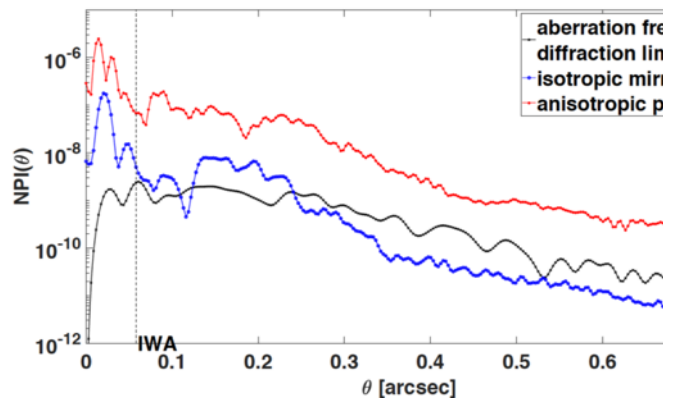
Figure 8-2: Normalized polychromatic irradiance (NPI), also related contrast from 10-6 to 10-12 as a function of arc-sec field of view from the inner working angle (IWA) [0.058 arc-sec] and the outer working angle (OWA) [0.740 arc-sec] for HabEx under three conditions: (1) no geometric or polarization aberrations (black) and (2) standard isotropic Al coated mirrors (blue) and (3) the as-measured anisotropic primary at the Steward Observatory Mirror Lab with standard Al coated mirrors (red). Plotted in the radial direction along the X-direction slice through the FOV at the image plane.

paper differ significantly from our results shown in **Figure 8-2** above and the differences remain unresolved.
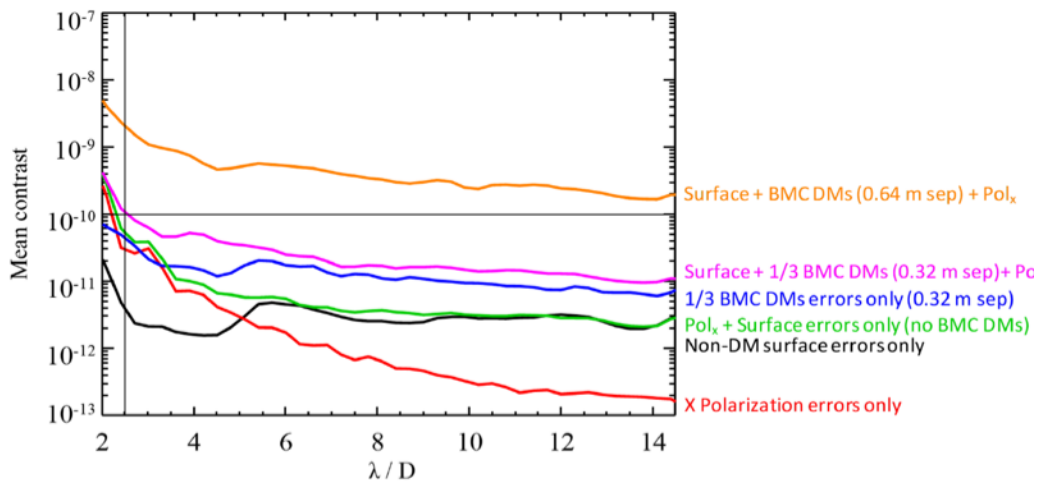
Figure 8-3: Post-EFC HabEx coronagraph (450 – 550 nm) radial contrast curves for a variety of aberrations present in the system.

Figure 8-4 below shows four graphs of the normalized polychromatic irradiance as a function of field angle between the IWA (58 mas) and the OWA (740 mas) in the form of horizontal and vertical slices through the PSF for XX (top row) and YY light (bottom row)[121]. These figures show that the exoplanet coronagraph contrast is not rotationally symmetric with the optical axis.

We conclude that the form birefringence that appears on large aperture coated surfaces, if left uncorrected will reduce terrestrial exoplanet contrast by a factor of 50 to 100.

(a) Horizontal XX slices

(b) Vertical XX slices

(c) Horizontal YY slices

(d) Vertical YY slices
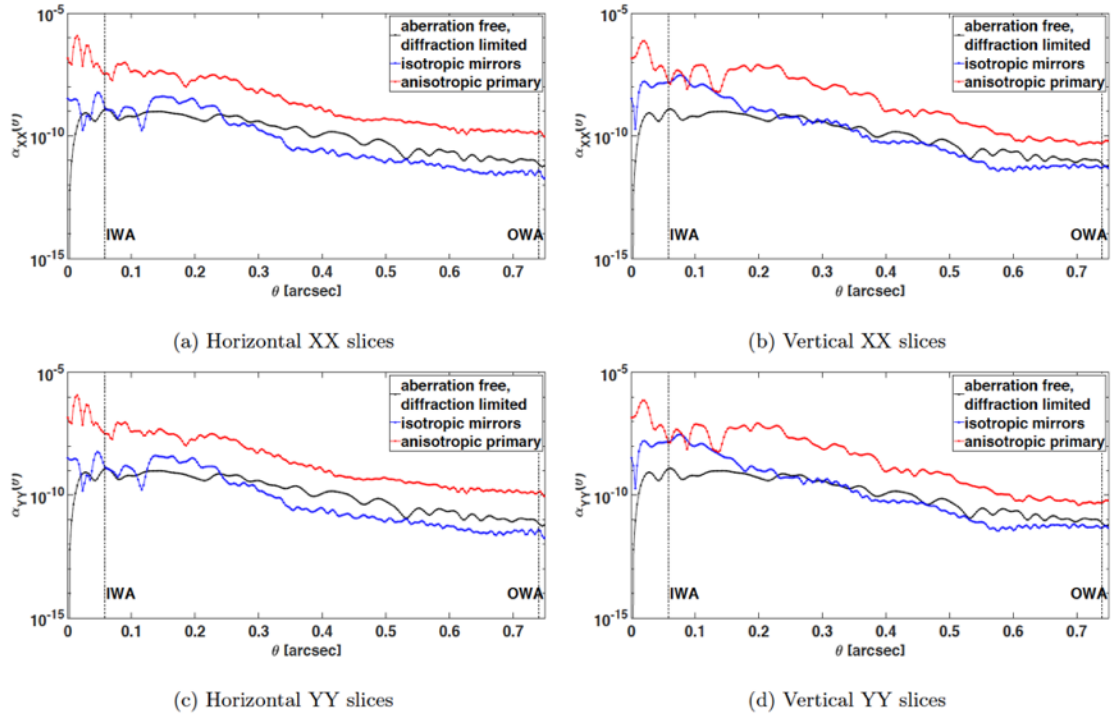
Figure 8-4: Normalized polychromatic irradiance shows that the HabEx coronagraph contrast is not rotationally symmetric with the axis of the system.

8.1   CONCLUSION AND FUTURE WORK

The form birefringence of a large diameter mirror was measured for the first time. The mirror had a peak retardance of 0.002 radians about 0.2 nm at 450 nm, and a peak diattenuation of 0.00025. These measurements were repeated at several system orientations to verify they were a property of the mirror and not the form birefringence polarimeter. The polarization components of interest were encoded onto different frequency components of the signal, produced by measuring the minimum transmission and its orientation for different analyzer angles, further distinguishing the polarization from other sources of radiation reaching the CCD.

More work should be done to understand how this type of form birefringence would impact the design requirements for exoplanet missions.

Additional measurements to either reproduce the results here or to test other large mirrors would provide useful information, especially if one instrument could measure multiple large mirrors coated by different methods.

The amount of allowable form birefringence to achieve a required contrast should be calculated and provided to the coating vendor as an upper limit to the coating performance requirement.

9   ACKNOWLEDGEMENTS

The authors would like to thank Ryan Irvin and Jim Harvey (Photon Engineering, Tucson AZ), Dae Wook Kim (Wyant College of Optical Sciences, University of Arizona, Tucson AZ), Tony Hull (University of NM), Brendan Crill & John Krist (NASA/JPL), Ewen Douglas (Steward Observatory, University of Arizona, Tucson AZ), Charles Lillie (NGAS retired) and Dimitri Mawet (Astronomy, Caltech, Pasadena, CA.) for their interest and help.

A. PROCESS DEVELOPED AND USED BY THE NATIONAL OPTICAL ASTRONOMY OBSERVATORY

This appendix A. provides the cleaning and coating processes used by the coating engineers at KPNO to fabricate the highly reflecting Al coating on the 3.75-m mirror measured for Milestone # 3. This is the same process coating engineers use to deposit the highly-reflecting metal thin film coat for the 4-meter Mayall telescope and other large astronomical primaries in Southern Arizona.

Doc #: 7000-AD-015-0002 by Gary Poczulp: poczulp@noao.edu and Patrick Dunlop

National Optical Astronomy Observatory

Kitt Peak National Observatory • Cerro Tololo Inter-American Observatory • NOAO Gemini Science Center

Doc #: 7000-AD-015-0002
Revision: Rev

Procedure for Removing Evaporated Aluminum Coatings from Glass or Glass- Ceramic Mirrors

Author(s): Larry Reddell, Gary Poczulp, Patrick Dunlop

A.1 Revision History

Rev	Date Approved	Sections Affected	Reason for Change Remarks and/or Change Details	Name
--	Circa 1960		Original: Procedure for Stripping and Cleaning NOAO Mirrors	
--	Circa 1994		Procedure for Stripping and Cleaning NOAO Mirrors	Larry Reddell Gary Poczulp
A	6/20/2014	all	Number document and put in proper format	Larry Reddell Gary Poczulp Patrick Dunlop

Approved by:

SigEng

_____

Name, ME Title

SigEM

_____

Name, EL Maint

SigSci

_____

Name, SciOps

Signature   24 January 2017

_____

Tammie Lavoie, Safety Manager   Date

A.2   Purpose

This procedure describes the processes for stripping/removing optics first surface in preparation for re-aluminizing optics. The document includes an overview of chemicals, preparation of chemicals and materials, and removal of optics 1st surface.

Applicable To

Aluminizing Procedure

Scope

The scope of this document is to outline the procedure for proper removal of evaporated aluminum coating from a mirrors substrate, and how to properly clean and prepare a mirror for a new evaporated aluminum coating.

Definitions

Training

1.   Respirator Fit Tested

2.   Handling of caustic chemicals

Safety

1.   JHA Form

2.   Daily Briefing Form 3.

A.3 Personnel, Equipment and Materials Required

The supplies needed for removing the aluminum coating are shown in Table 1 below.

Supplies for Aluminum Coating Removal		
	Chemicals	
	Hydrochloric Acid	
	Copper Sulfate	
	Potassium Hydroxide	
	Nitric Acid	
	Calcium Carbonate	CaCO3
	Cleaning Materials	
	Orvus Soap	1 oz. / 1 US gal. H2O
	Sea Sponge	Conditioned prior to use*
	TexWipes 609 Wipers	
	Kaydry	
	Long Q Tips	
	Dust Masks	
	Hair Net	
	Nitrile Gloves	
	Eye Protection	
	Water Boots	
	Water Bib	
	Distilled Water	
	Pressurized Spray Bottles	1 with soap mix
		1 with distilled water
	Visqueen Plastic	
	3M 764 Orange Tape	Or cloth type duct tape
	Safety	
	Chemical Resistant Suit	
	Chemical Resistant Gloves	Ansel Edmont Sol-Vex
	Chemical Resistant Boots	
	OSHA Respirator	Acid Vapor Cartridge

*Conditioned: Soaked in a 2%-10% HCl/H2O Solution until coral dissolved Table 1: Supplies and Tools
Table 2: Supplies and Tools

A.4   Procedure

Overview

1.   The following tasks are to be planned prior to and during the optics aluminum coating removal process.

   • Perform a visual inspection of each component to assess the overall condition. Document and make notes of any anomalies that are observed.

   • Stage the area with all necessary equipment/tools used during the removal process.

   • Ensure all personnel involved understand the daily process, safety and goals.

   • A safety meeting is held every day prior to any work taking place and again at the end of the day to discuss any safety issues.

   • For steps 2 through 8, use Ansel Edmont Sol-Vex chemical resistant gloves (style 37-185, size 10, 22 mil. thick by 18" long). Then change to a powder free nitrile or latex (clean room type) glove during the final rinse, drying and inspection stages, taking care to change gloves whenever they become contaminated.

   • For steps 2 through 8 chemical protection suits, goggles, and appropriate respirators are required.

   • Do not allow any wipers to contact the side of mirror and then continue to be used on the optical surface.

A.5   Aluminum Coating Removal, Chemical Preparation:

The recipes for mixing the chemicals are as follows:

1.   Chemical "A" (Hydrochloric Acid and Copper Sulfate, also locally known as "Green River")

   • 2.72 kg (6 lb) hydrochloric acid (HCl, 37%) reagent grade. 227 g (0.5 lb) cupric sulfate (CuSO4 5H2O) reagent grade.

   • Put 6 L of distilled water into a 10 L (2.5 US gal) container and add HCl and CuSO4 5H2O. Add distilled water to make 10 L (2.5 US gal). Shake until CuSO4 5H2O is dissolved.

2.   Chemical "B" (Potassium Hydroxide)

   • 2 cups (dry measure) potassium hydroxide (KOH) reagent grade pellets.

   • Put 6 L of distilled water into a 10 L (2.5 US gal) container and add KOH pellets. Add distilled water to make 10 L (2.5 US gal). Shake until KOH is dissolved.

3.   Chemical "C" (Nitric Acid)

   • 3.2 kg (7 lb) nitric acid (HNO3, 70%) reagent grade.

   • Put 6 L of distilled water into a 10 L (2.5 US gal) container and add HNO3. Add distilled water to make 10 L (2.5 US gal).

A.6   Aluminum Coating Removal Procedure:

The following procedures assume all necessary materials are available and accessible. At a minimum, 2 people are needed to perform this operation. As a rule of thumb, it has been found that one person per meter diameter of mirror are required to clean the mirror and at least one additional person to handle supplies and hoses for the cleaning crew. The process below assumes 5 people. The entire operation should able to be completed in about 1 day.

1.   Gently wash the mirror with distilled water and Orvus soap (1 oz. Orvis per 1 US gal H2O) to remove large particulates. Inspect the mirror for any oils and remove using reagent grade acetone and Kaydry EX-L Delicate Task wipers.

2.   Cover the mirror with Kaydry EX-L Delicate Task wipers and then pour on "A". With a gloved hand smooth out the saturated wipers to keep the liquid in place on the surface. When most of the aluminum is removed, gather the saturated wipers into wads and swab any remaining spots. After the optical surface is clean use the saturated wads to remove any aluminum from the side of the mirror.

> *Note: After working on the side of the mirror discard the saturated wad and DO NOT return to work on the optical surface or risk contamination.*

3.   Rinse with filtered water and clean gloves.

4.   Sprinkle calcium carbonate (CaCO3) on the mirror and wet with "B" while rubbing with a wad of three or four Kaydry EX-L Delicate Task wipers, also wet with "B". The resultant slurry is thoroughly scrubbed over the surface in a circular or figure eight swirling motion, paying particular attention to the edges and adding more "B" as necessary to keep the CaCO3 from caking or drying out.

> *Note: After working on the side of the mirror discard the saturated wad and DO NOT return to work on the optical surface or risk contamination.*

5.   Rinse with filtered water.

Repeat step 4 using "B" and CaCO3 at least three times, with rinses in between.

6.   Rinse with filtered water and clean gloves.

7.   Pour on "C" as a rinse and quickly swab with a wad Kaydry EX-L Delicate Task wipers. This step will remove all traces of calcium carbonate.

> *Note: After working on the side of the mirror discard the saturated wad and DO NOT return to work on the optical surface or risk contamination.*

8.   Rinse with filtered water for five to ten minutes. Final rinse with bottled deionized or distilled water. Remove chemical protection suits and switch to nitrile or latex cleanroom gloves.

9.   Systematically dry the mirror using two sheets of TexWipe 609 wipers at a time. Holding a corner of the wipers with one hand, place the other hand on the wipers to make contact with the substrate and drag the wipers toward the edge of the mirror and off. Starting from a dry

area pull the wiper into the wet edge and follow this edge to the side of the mirror and off again. This is repeated until the entire surface is dried.

> Note: Never allow the water to evaporate from the substrate, always dry with clean wipes.

10.   A final "buff" of the optical surface is done using a Texwipe 609 wipe with a drop or two of reagent grade ethanol. The wiper is folded such that it covers the entire gloved hand (preventing the glove from touching the surface) and the entire surface is rubbed using a circular motion several times.

> Note: The wiper pad with the minute quantity of ethanol on the center wets the surface and simultaneously dries it – you should not see any ethanol streaks evaporating as the wiper is rubbed on the surface. As the wiper is rubbed on the surface it is possible to feel a contaminated area by feeling a change in the drag of the wiper. These areas are attended to using freshly prepared ethanol spotted wipers until no change in drag is felt over the entire surface.

11.   Use CO_2 snow or filtered gaseous nitrogen (N_2) to blow off any dust or lint.

12.   With the room lights dimmed, inspect surface with high intensity lamps for lint, drying streaks and soils.

> Note: It has been found that if the final ethanol buffing has been done correctly, an inspection with a high intensity LED light source will not be necessary. If the soils are not removed by buffing, it may be necessary to go back and repeat the process from step 4.

13.   Just before closing the chamber use CO_2 snow for a final dust off.

A.7   Records

1.   JHA signature sheet; kept by safety office, scanned and stored \ets_share\Safety

2.   Fall protection training: kept by Safety Office

3.   Rigging, suspended load: kept by Safety office

4.   Maintenance record

A.8   References

1.   KPNO Emergency Manual

2.   Other procedures that are called out list by number

B.   DIFFRACTED AND SCATTERED LIGHT IN OPTICAL SYSTEMS FOR EXOPLANET SCIENCE

B.1   Introduction

A review of the literature indicated that diffracted light from a segmented primary aperture and scattered light from surfaces in the optical paths within exoplanet telescope/coronagraph systems could be better optimized for characterization of the physical properties of terrestrial exoplanets. At the same time, the LUVOIR project had fallen behind their schedule to deliver Lyot coronagraph designs to us for our polarization analysis task. We redirected our workforce to identify innovative concepts to control diffracted and scattered light. The contents of this Appendix B introduces these concepts.

The primary mirror for LUVOIR is segmented into nested hexagonal mirrors. Each mirror is separated from its neighbor to allow deployment and thus straight-line gaps in an otherwise continuous surface mirror appear across the aperture. In addition, the secondary support system obscures the primary to leave shadows. Much work has been done to reduce the effects of the gaps and shadows by placing specially constructed apodizing masks over a relayed image of the pupil [122] [123]. Most of these approaches required excessive absorption of light and reduction of SNR to reduce terrestrial exoplanet yield.

Our approach was to examine the reasons the hex segment pattern was originally chosen and identify a segmentation architecture that improves coronagraph performance, preserves a mirror deployment architecture, is less complicated with fewer surfaces and may be more cost effective and optimum for terrestrial exoplanet science.

B.2   Diffraction masks exoplanets

In this section, we recognize that the telescope-coronagraph complex-wave optical system performance needs to be optimized end-to-end. That is, the complex-wave performance of the telescope must be designed to match that of the coronagraph system if we expect the end-to-end optical performance to be optimum for exoplanet characterization. The two optical systems (fore-optics and instrument) need to be pair-wise optimized simultaneously during both the design approach phase and later at the detailed design and development project.

Large-aperture telescope systems are segmented for manufacturing, assembly and packaging for launch purposes. The aperture appears discontinuous because of the gaps between segments needed for hinged deployment of the reflecting surface from a launch vehicle envelop into the spacecraft telescope system. These segment gaps project unique signatures across the image plane. Large-aperture telescope primary mirrors today are partitioned into arrays of hexagonally shaped segments for structural purposes and to enable in-space deployment there are gaps between these segments. These periodic straight-line gaps diffract light across the image plane which mask exoplanets and pollute the faint exoplanet spectra with light from the parent star. The gaps appear as slits which may introduce unwanted polarization[124] to affect precision polarimetry. The periodic structure topology used today across large primary apertures causes unwanted ghost images of the star which may mask exoplanets.

Figure B-1 left, given below shows the aperture for a "typical" classic segmented telescope, tessellated using regular hexagonal segments. The figure on the right shows the image plane monochromatic irradiance for the aperture on the left. Looking at the aperture to the left we see that the gap-lines that separate the segments line-up to form segments of slits and we see that these "broken" gaps form an array of slits whose spacing we identify as w/2 where w is the face-to-face width of each regular mirror segment. The hexagonal symmetry of the segments results in the hexagonal symmetry shown in the PSF at the right in this figure. The monochromatic irradiance distribution at the image plane of a 10-meter segmented aperture is shown at the right covering the center 1 x 1 arc second field of view.
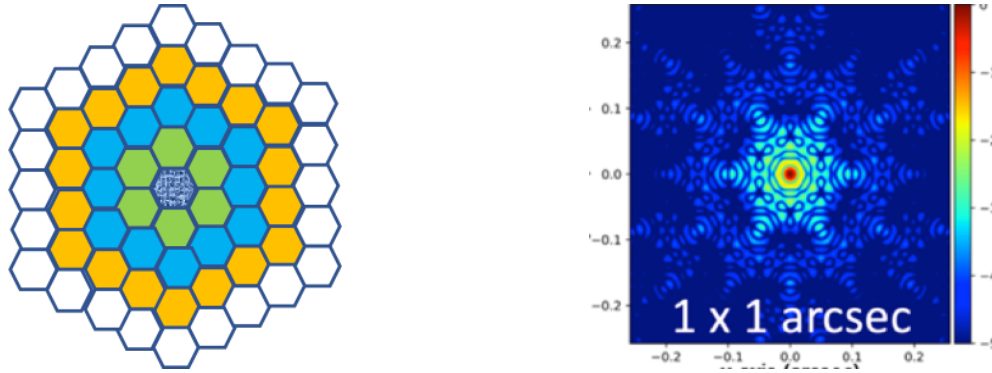
Figure B-1: Left: classic segmented telescope 10-m class aperture tessellated using hexagonal segments. **Right:** corresponding complicated point spread function (PSF) or signature characteristic of the aperture segmentation pattern shown to the left. The PSF brightness scale is Log_{10}.

We want to characterize terrestrial exoplanets in the habitable zone to maximize our probability of finding life like ours. Therefore, it is of interest to calculate the location of earth-sun twin exoplanets at the image plane of a 10-m aperture. In **Table B-1** we present a calculation of the angle in mas of a terrestrial exoplanet twin as a function of range from the earth in units of parsecs. Note that the earth-twin terrestrial exoplanets are located at field angles between 50 and 10 milli-arc-seconds (mas).

We next calculate the image plane location of the diffraction grating images of the parent star. This is the angular separation in the optical system field of view between the parent star and the exoplanet. We use the well-known diffraction grating equation and write:

$$n\lambda = 2d\sin\theta$$

Where n is the diffraction order, λ is the wavelength of light, d is the period of the grating and θ is the angle of diffracted star image as it appears at the image plane for order n. For hexagonal segments this grating period is w/2, where w is the edge to edge distance across one hexagonal segment. Using this equation, we calculate the entries in Table B-2, below.

Table B-2: image plane radius, in milliarcseconds (mas) from the central star at 500-nm wavelength for the diffraction order 1 and the radii of the resulting diffraction order n=1 grating spectrum from 450 to 550 nm wavelength for 1 , 2 and 3 meter "across the flats" hexagonal segments.

2d in m	Order n=1	450=>550 nm
Hex F to F in meters	Center mas	Dispersion mas
1	103	±10.3
2	52	±5.2
3	34	±3.4

If we compare the angular location of the diffracted star **Table B-2** with the location of candidate terrestrial exoplanets **Table B-1** we see that diffraction and its resulting dispersion from the ensemble of hex segments cause the exoplanets to be masked.

Table B-3: Exoplanets masked.

Distance Parsecs PC	Angle between star and Earth twin in milli-arc-sec	Aperture in meters Diffraction limited at 500 nm	Aperture in meters third Airy diffraction ring
10	100.0	1.2	3.7
20	50.0	2.5	7.5
30	33.3	3.7	11.1
40	25.0	5.0	15.0
50	20.0	6.2	18.6
60	16.7	7.4	22.2
70	14.3	8.7	26.1
80	12.5	9.9	29.7
90	11.1	11.1	33.3
100	10.0	12.0	36.0

Table B-1: Image plane location in milli-arc-seconds (mas) of earth-twin exoplanets as a function of distance or range from the earth in units of parsecs. Column 1 distance in parsecs, column 2 angular separation in mas between the parent star and the earth twin, and column 3 is the telescope aperture in m required to place the terrestrial exoplanet at the 3rd Airy diffraction ring of a 10-m aperture at 500-nm wavelength.

Distance	Angle	Aperture
(pc)	(mas)	(m)
20	50.0	8.1
40	25.0	16.3
60	16.7	24.4
80	12.5	32.6
100	10.0	40.7

The Hipparcos catalog shows that there are 2347 stars with measured parallaxes of pi = 33.33 mas, which correspond to a distance of 30 pc down to stellar magnitude V=8[125]. Exoplanets are ~10^{10} fainter than their parent star. If the parent star has magnitude V=8, then the faintest terrestrial exoplanets within 30 pc will be between stellar magnitudes 31 and 34. For reference, the Hubble (2.4-m) ultra-deep field magnitude limit is ~29 and required an exposure of approximately $2*10^{+5}$ seconds[126].

B.3   Physical Optics OF Diffraction

B.3.1   *Ground and space telescopes*

Discontinuous telescope pupils, that is telescope apertures that have some portion of the aperture blocked are responsible for diffraction "noise" at the image plane. Breckinridge, Kuper and Shack (1982)[127] were the first to discuss the role of secondary support diffraction spikes in finding exoplanets. **Figure B-2** shows the diffraction pattern from the HST caused by the secondary support structure. Near the star we also see the "diffuse-light" effects of narrow angle scattered light. The sources of narrow angle scattered light in telescope-coronagraph systems were discussed by Harvey, et. al.[128]

Figure B-3 shows the pupil, left and the irradiance at the image plane for an on-axis star at 1-micron wavelength for the 30-meter diameter CELT (now called the Thirty Meter Telescope, TMT)[129]. The PSF is plotted on a $\log_{10}$ intensity scale and the grey scale across the top of the PSF image on the right shows intensity order of magnitude from 10^0 to 10^{-10}. The field of view is 1 x 1 arc-second. We see light scattered beyond 1 arc-second at intensities greater than 10^{-4} to obscure accurate exoplanet radiometric and spectral measurements. This scattered light is caused by the periodic structure across the telescope primary mirror produced by the close-packet hexagonal segments. Clearly if we can devise a pupil architecture or topology to mitigate these prominent diffraction pattern science data quality and exoplanet yield will increase.
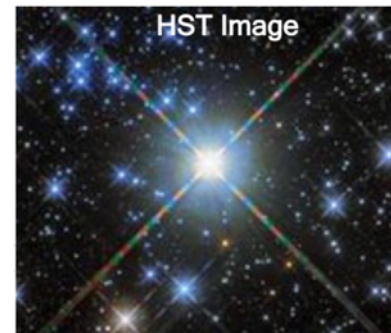
Figure B-2: HST image of a star showing the diffraction spikes that mask exoplanets at 4 position angles. The halo around the star is produced in the telescope-instrument system by narrow angle scattered light. The Airy diffraction pattern for HST is about 100 milliarc seconds which is too large to observe terrestrial exoplanets.
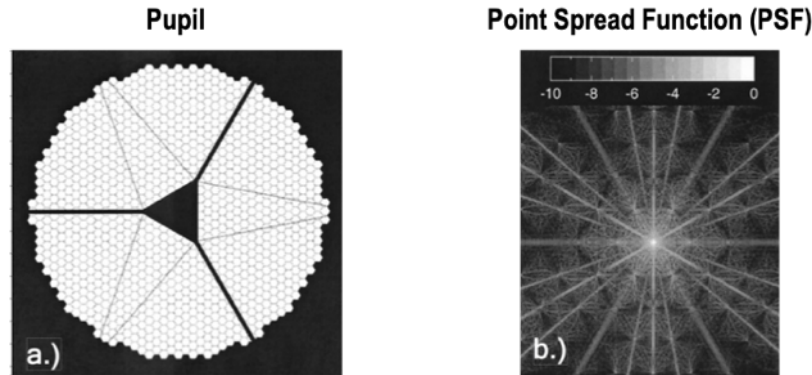
Figure B-3: **a.)** Illustration of the proposed 30 m diameter pupil of the CELT (now called the Thirty-meter telescope), complete with segmentation geometry, central obscuration and associated secondary mirror struts; **b.)** Monochromatic logarithmic PSF for this Image. The field of view is 1 x 1 arcsecond. Diffraction effects of the triangular central obscuration and the secondary mirror struts are readily apparent, as are the characteristic hexagonal symmetry of the mirror perimeter and the inter-segment gaps.

B.3.2 *Segmented space telescope diffraction*

Today, large-aperture space telescopes (for example JWST) use apertures that are close-packed regular hexagon-sided mirrors to pack into a nearly circular telescope pupil. This telescope primary exhibits three diffraction gratings which diffract light from the much brighter star across the image plane and create background noise for imaging and spectroscopy of exoplanets. The direction of the "rulings" of the gratings are shown using colored lines.

The rulings are discontinuous across the LUVOIR pupil, but that does not make a difference to the diffractive properties of the straight lines. **Figure B-4** shows two of the three sets of diffraction grating rulings across the hexagonally segmented LUVOIR pupil. The third set of rulings, the horizontal set are not shown to avoid confusion in the drawing.

Figure B-4 shows the close-packed hexagon-segmented primary mirror with lines drawn to show the grating "rulings" and the direction of the rulings. Note that to keep confusion down we have not drawn in the set of horizontal "rulings". The "groove-spacing" is seen to be d, where d is one-half the face-to-face distance across the individual regular hexagons. The diffraction causes a structured background across the image plane that may obscure important exoplanets and may introduce unwanted polarization aberrations into the coronagraph to affect image quality.

B.3.3 *The PSF for a Monochromatic Star*

Gratings diffract light into orders which map a single on-axis point (a star, for example) into multiple images of that star. If the source is polychromatic then the grating maps the polychromatic single on-axis point into multiple spectral images stretched out radially.
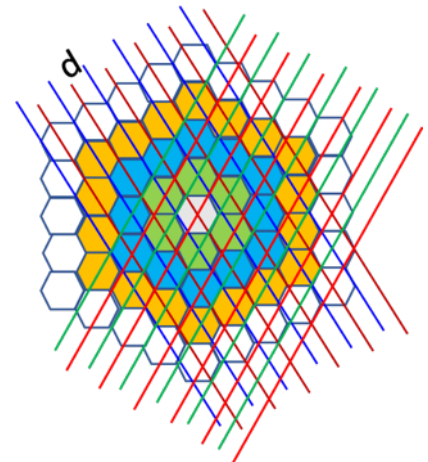
Figure B-4: Two of the three diffraction gratings across the close-packed hexagon-segmented primary mirror are shown. The spacing of the "ruling" is d.

Let λ = wavelength; d=ruling spacing; n=diffraction order and θ= angle from the axis, then the grating equation that relates these four variables is written:

**Equation
B-1**

The angular separation between diffraction orders is θ as given in **Equation B-1**, above.
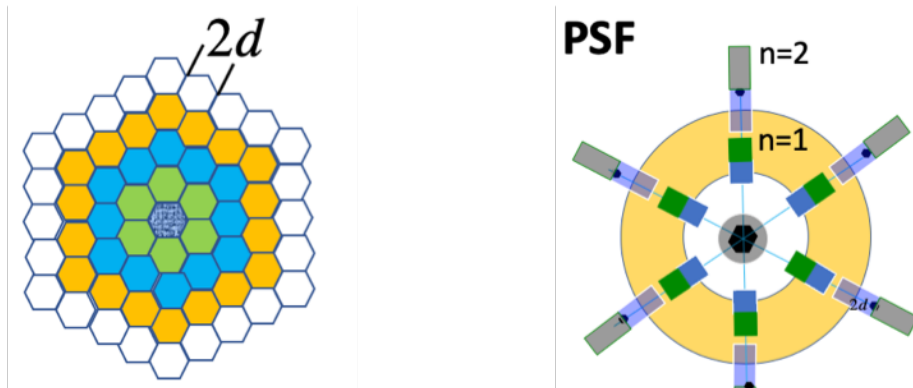
**Aperture has three diffraction
gratings across it.**

**Image plane n=0,1,2 spectrum
of the star.**

Figure B-5: Shows, **left**, a pupil map and right a representation of the monochromatic PSF associated with the close-packed hexagon-segmented primary mirror shown on the left. The points on the **right**-hand side show the location of the diffraction orders. The center is the image of the star and the first ring of points corresponds to the 1st order of the three diffraction gratings. The second ring of points corresponds to the 2nd order of the three diffraction gratings.

In **Figure B-5** we see that a Lyot coronagraph occulting mask would only block light from the zero-diffraction order, which contains light from the bright central star. But light from the higher diffraction orders n>1 will scatter around the occulting mask to flood the detector plane. The occulting mask could be designed such that each order has its own mask, but that would block portions of the FOV where exoplanets might be found.

To determine if the diffraction images of the parent star will obscure exoplanets, we calculate the angular separation between zero order and the first order, n=1, for polychromatic light. **Table B-4** below shows the angular separation of the 450, 500, 550 nm wavelength monochromatic diffraction orders as a function of the face-to-face segment size.

Table B-4: Angular separation of the diffraction orders for face-to-face segment sizes: 1, 2, 3, 4 meters. This applies to the diffraction orders shown in **Figure B-5**, above.

Face-to Face segment size in meters	Angle for 450-nm masec	Angle for 500-nm masec	Angle for 550-nm masec
1	93	103	113
2	47	52	57
3	31	34	38
4	23	26	28

We compare the entries in **Table B-2** with the entries in **Table B-1** and see that the unwanted diffraction images of the parent star fall within the same FOV region as the exoplanets. Clearly there would be a significant advantage to the development of a straightforward, low absorption way to eliminate these diffraction orders. The pinwheel pupil provides that opportunity.

B.3.4 *The PSF for a Polychromatic Star*

Exoplanets are very faint thermal sources. If they are to be observed in monochromatic or narrow band light integration times become impossibly long. The HabEx coronagraph is planned to observe in 100 nm bandwidths. One of these bandwidths is 450 to 550 nm and we have used those values to compute the diffraction angles shown in **Table B-4** The star image at n=1 for the 1-meter face-to-face segments is a colored radial streak or small spectrum with 450 nm light at 93 masec and 550 nm light at 113 masec. The 2-meter face-to-face segments is a colored radial streak or small spectrum with 450 nm light at 47 masec and 550 nm light at 57 masec. This continues to the 4-meter face-to-face segments which give a colored radial streak or small spectrum with 450 nm light at 23 masec and 550 nm light at 28 masec.

B.3.5 *Isoplanatic Point Spread Function for Image Processing*

The polychromatic PSF shown in **Figure B-5 (right)** is not linear shift invariant and therefore the optical system is not isoplanic. Also, looking at **Figure B-5 (right)**, we see that the PSF is not rotationally symmetric either. These two facts complicate digital image processing. In this paper, we have devised a pupil segmentation or topology architecture that will produce images from an emulated filled aperture telescope pupil even though the pupil is mechanically segmented. This promises to reduce significantly the effects of an anisoplanatic PSF and will make digital image processing more reliable and less uncertain.

B.3.6 *Compensating for Hexagonal Segments*

Technologies to compensate for the diffraction patterns produced by straight line gaps and straight-line support structures across primary mirrors of large telescopes has been an area of active study recently [130,131,132,133,134,135]. None of these methods may be completely satisfactory, however, since light is absorbed in the process to reduce exoplanet yield.

B.4 Curved secondary support structures not neW

B.4.1 *Background*

Breckinridge (2018)[136] suggested partitioning the primary into curved sided segments and curving the secondary support structures to reduce diffraction noise at its source to control diffraction noise at the image plane of exoplanet coronagraphs. We have shown above that the hexagonal segment architecture or pupil topology leads to unwanted diffraction noise in the system. It is good engineering practice to seek ways to eliminate or reduce "noise" at its source, rather than devise complicated, difficult to calibrate and signal absorbing methods to compensate. Methods to mitigate diffraction noise were developed over the years by amateur astronomers, and later optical scientists. However, the professional space and ground astronomical optical telescope and instrument community is not aware of these techniques.
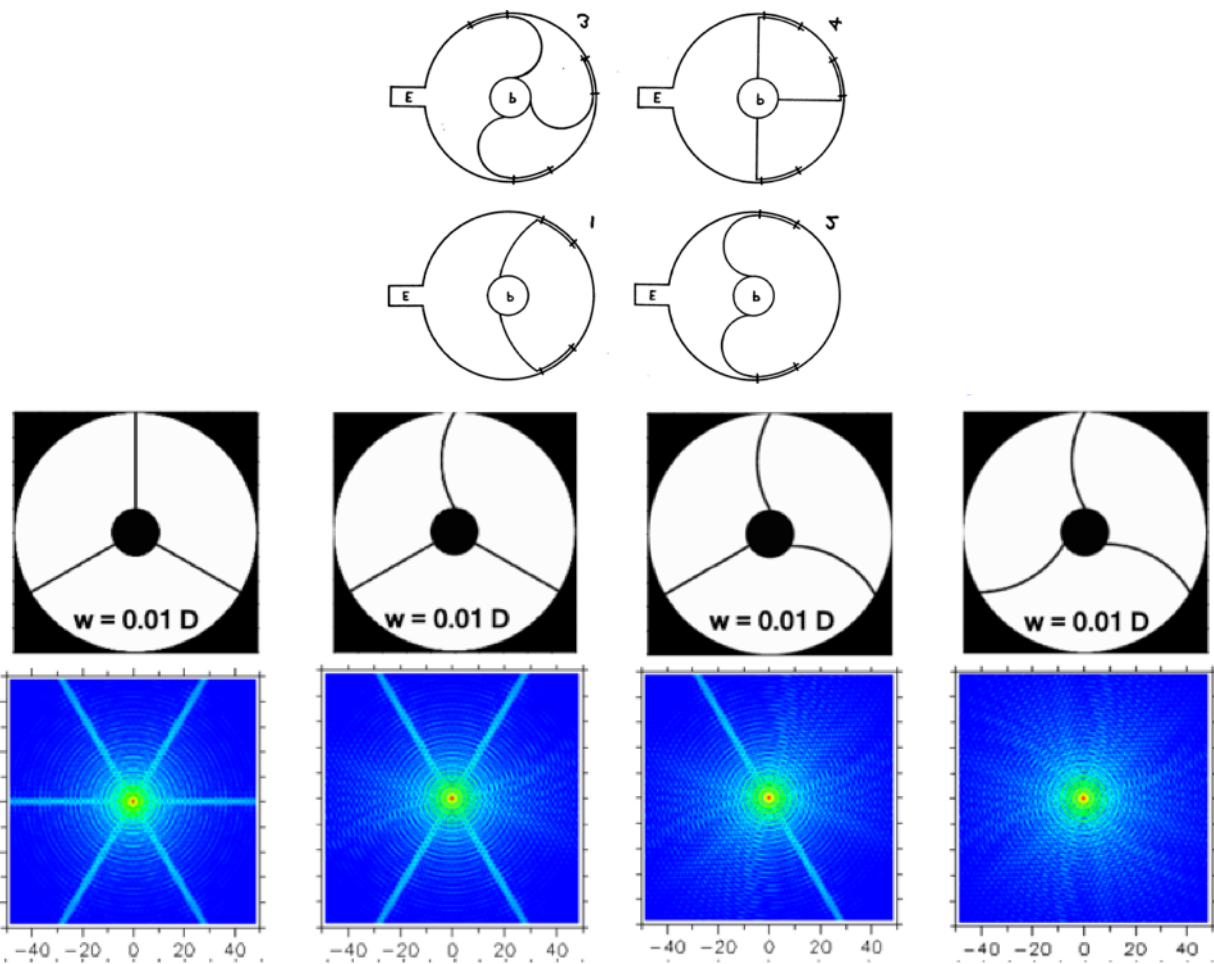
Figure B-6: [TOP] The four secondary support structures built by Werenskiold[14] and used for visual observation of planets. View looking from the open end of a reflecting telescope back toward the primary mirror. He reports that #4 gives the lowest quality image and that curving the support structure appears to remove the diffraction spikes from visual images to give higher contrast for visual planetary observations. [BOTTOM 2 ROWS] Top row telescope entrance pupil obscured by secondary support system to show how curving the strut eliminates diffraction spikes at the image plane shown in the lower row.

C. H. Werenskiold (1941)[137] reported on the work of A. Couder published in the French journal: Astronomy, Jan 1934 and translated into English and republished in Amateur Telescope Making Advanced (scientific American Publishing), pp 620-622. Couder proposed controlling diffraction in Newtonian and Cassegrain type telescopes by placing lune shaped curved masks over the straight edge support structure of the secondary. These masks blocked significantly, the light-gathering ability of the telescope, negatively affecting the telescope transmittance. Werenskiold proposed curving the secondary support structures themselves as shown in **Figure B-6** to reduce masking of the primary mirror and control the diffraction spikes.

Werenskiold writes: *"It is generally conceded that a reflector, in regard to definition obtained, is apt to be somewhat inferior to a refractor of comparable size. However, the use of a curved spider in a reflector appears to be a promising step towards reducing this difference in comparative performance of the two telescope types."*

B.5   Modelling a 10-Meter Pinwheel Pupil

B.5.1   *Pupil Architecture of Topology*

Richter[138] selected 6 diffraction masks and photographed the diffraction pattern from each to show that curved arcs on the pupil left no discernible diffraction pattern at the image plane. Harvey[139] used FRED[140] and applied the design methodology outlined in Richter[138] and developed further by Harvey and Ftaclas[141] along with the computer analysis program FRED to show that the image plane diffraction patterns from curved secondary support structure is less than 10^{-6} where-as the image plane diffraction patterns from straight line secondary support structure are $\sim 10^{-2}$.

Based on our intuitive understanding of diffraction from curved segments we designed a pupil topology for a "first look" at the diffraction effects. The design we chose is shown in **Figure B-7** below. We selected a 10-meter Cassegrain primary with an obscuration ratio of 0.16 and six curved secondary mirror support struts, each with a 30° arc of a circle and 20 mm wide gaps. There are three rings or zones of segments curved on all sides. Each zone contains 12 curved sided segments to create a telescope entrance pupil that has 36 segments.

Figure B-8 shows a plot of monochromatic intensity, on a linear scale, as a function of azimuth angle at field 0.75 arc sec. for three 10-m diameter pupil architectures: unobstructed, spider and pinwheel. The computation was performed using MatLab. Computational capacity limited the size of the sample interval across the pupil and we believe that may have resulted in an incorrect representation of the image plane diffracted light. However, several features in **Figure B-8** are worth noting. The profile for the 4-spider mask, shown in red, is much higher than that for the pinwheel which indicates that the pinwheel pupil is making a contribution to smoothing out the diffraction pattern. The prominent dip in energy at the feet of the spider diffraction pattern is probably the result of the very narrow bandwidth of this monochromatic computation. The noise on the pinwheel is probably caused by having an insufficient number of samples across the pupil, which was dictated by the array sizes and the computational time limits of Matlab. Consequently, we decided to drop MatLab as our computational tool and turn to Photon Engineering. LLC and the FRED software. Computations using FRED were successful and are shown in the paper: SPIE Proc 10698-60[137].

For large-aperture telescopes, we discovered a pinwheel segmented aperture topology that minimizes this diffraction-caused "noise" structure at the image-plane[142,143]. This topology and its performance are compared to that for a hexagonally segmented aperture in **Figure B-8**, below.

Obscuration = ε = 0.16
R1 = radius of 1st zone = 2.43m
R2 = radius of 2nd zone = 3.65m
R3 = radius of 3rd zone = 5.07m

12 Curved Radial Gaps thru all 3 tiers (30º arc of circle) are 10mm wide. 6 are obscured by struts.

6 Curved Secondary Mirror Struts (30º arc of circle) are 20mm wide.

2 Centered Circular Gaps separating the 3 tiers (360º arc of circle) are 10mm wide.
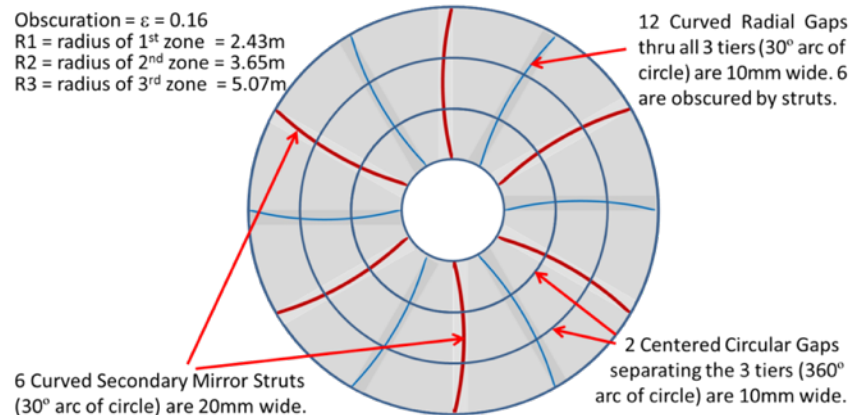
Figure B-7: Cassegrain primary with an obscuration ratio of 0.16 and six curved secondary mirror support struts (shown in Red), each with a 30º arc of a circle and 20 mm wide. There are three rings or zones of segments curved on all sides. Each zone contains 12 curved sided segments to create a telescope entrance pupil that has 36 segments. Design by Jim Harvey.
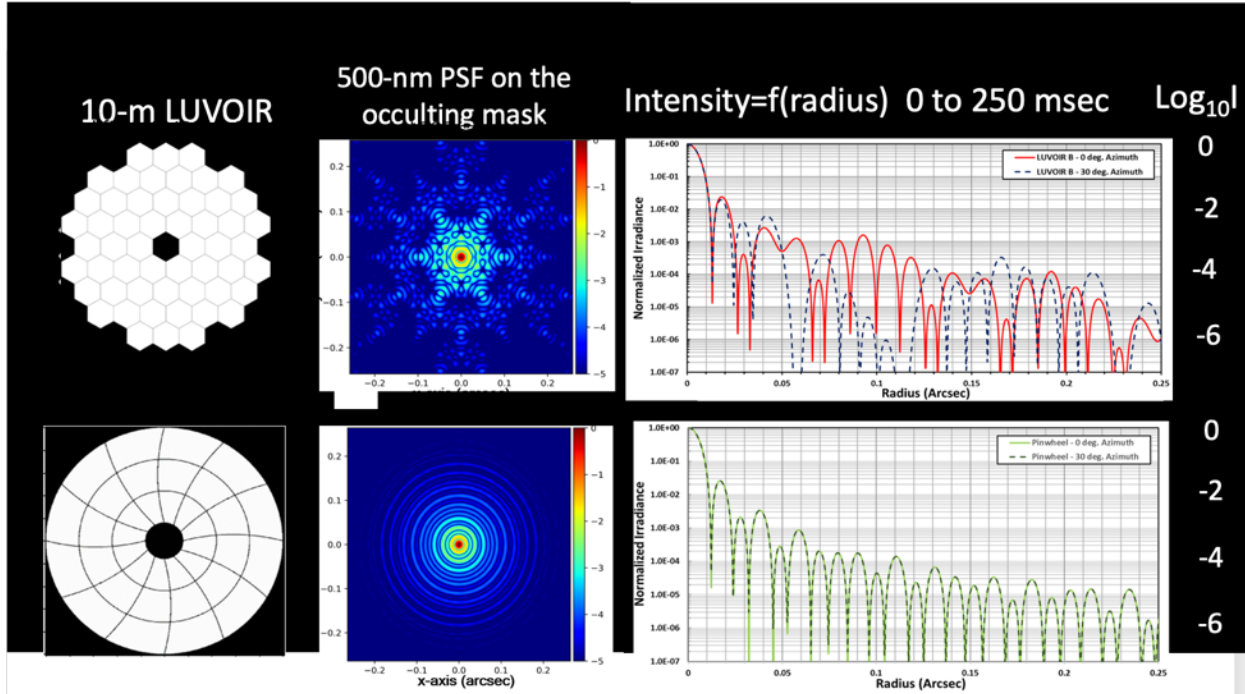
Figure B-8: Monochromatic diffraction patterns for a modified LUVOIR-B aperture stretched from 8-m to 10-m diameter with 5-mm segment gaps is compared to a 10-m diameter pinwheel aperture with 5-mm segment gaps. Top row L to R: modified LUVOIR-B aperture map, $\log_{10}$ stretch of the PSF and a plot of the normalized irradiance as a function of radius for 0^0 (red) and 30^0 (blue dots) azimuth angle. Bottom row L to R: pinwheel aperture map, $\log_{10}$ stretch of the PSF and a plot of the normalized irradiance as a function of radius for 0^0 (green) and 30^0 (grey dots) azimuth angle. The center plots on a blue background show the expected system point spread function that falls onto the coronagraph occulting mask. The PSF structure shown at top-center indicates that many false-positive identifications of exoplanets may occur and exoplanets would be masked if a hex segmented aperture is used.

The axially-symmetric pinwheel-aperture, for an on-axis "Cassegrain" telescope configuration is shown in the lower left of **Figure B-8**. The Cassegrain secondary is suspended above the primary and held centered by curved vane structures. The vane structures are curved to match the pinwheel curvatures. The match is made by rotating or clocking the vanes to shadow the segment gaps. This aperture will be less expensive to fabricate, assemble, test and align than is the axially-symmetric hexagonal-segmented aperture because of the decreased diversity within the opto-mechanical mirror assembly. This primary aperture mirror requires building one curved and tapered wedge which has 3 optical prescriptions on each of three curved sided segments and then duplicating that wedge 12 times for the remainder of the aperture. An anticipated technical issue is the sharp angles on the surface of each segment. However, recent technical developments in magnetorheological polishing[144] of mirror surfaces indicate that the mirror substrate will hold an optical figure of 0.05 wave or better to the edge.

In addition to the obvious design, fabrication, test and alignment advantages of the pinwheel aperture there is a spacecraft system operational gain since the space-craft does not need to be bore-sight rolled to various field azimuth angles to accommodate the non-rotationally symmetric image plane mask introduced across the field by diffraction from the hexagonal segments. Almost twice as many terrestrial exoplanets can be characterized using the pinwheel aperture telescope-coronagraph system during the mission lifetime as can be characterized using an aperture tessellated with hexagonal segments.

Future work on the pinwheel aperture concept includes the design of a Lyot coronagraph for the PSF shown in **Figure B-8**, lower center; with a quantitative assessment of the achievable contrast. This will be followed by an assessment of sensitivity of that contrast to polarization aberrations and mechanical dynamic deformations of the pinwheel aperture using software models and hardware testbeds.

One design approach that may eliminate the need for wide (~5-mm) gaps between segments is in-space assembly of the large aperture[145,146].

Figure 8-8 above, which shows diffraction patterns for a modified LUVOIR-B aperture stretched from 8-m to 10-m diameter with 5-mm segment gaps is compared to a 10-m diameter pinwheel aperture with 5-mm segment gaps, suggests that the hexagonal segmentation may yield a darker background and thus increased capability for higher contrast coronagraphy than does the pinwheel aperture. But this is probably not the case. The plot in the upper right of the figure (intensity as a function of radial field) shows this may be true in the case of narrow-band monochromatic light. However, terrestrial exoplanet coronagraphy needs at least a 100 nm bandwidth to have sufficient signal to obtain a record and the dark background at 50 milli-arc-seconds will be filled in with polychromatic light.

B.6   Manufacture of curved-sided segments

About 1980 astronomers[147], without a trade-off for image quality, decided that hexagonal segments were optimum both for manufacture and for general astronomical imaging optical telescopes. Since then, all astronomical telescopes larger than 8-meters have used hexagonal segments to tile their large aperture primary mirrors.

Mirror fabrication technology, developed over the past 40-years, now enables more diverse segment patterns. The architecture for segmentation can now be based on desired optical system image quality criteria. In this section we discuss a mirror fabrication technology that will produce a segment architecture optimized for terrestrial exoplanet science.

The manufacture of curved-sided non-circular aspheric-surface segments is not different than the manufacture of hexagonal-sided aspheric-surface segments, provided the radius of curvature of the sides are gentle, as shown in **Figure B-7**. The biggest challenge is maintaining the "global" optical surface figure for those regions near the "points" of each segment. Technology developed by Tinsley for the figuring of the Keck hexagonal-sided segments included: stressed mirror polishing and deterministic polishing is applicable to the curved sided segments. One approach is given here.

With a full-sized tool use rapid material removal polish for the roundels, removing most of the volume between the "nearest sphere" and the off-axis aspheric form.
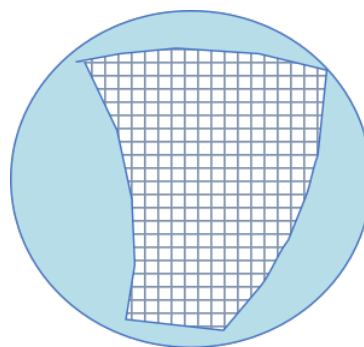
Figure B-9: Pinwheel pupil segment is shown within its Zerodur roundel. The rectangular grid support structure is shown to indicate an isogrid back structure. Engineering details of this isogrid structure would follow detailed structural engineering for thermal, mechanical, and structural design of the mirror as a space-flight element attached to a back-plane.

Then shape the roundel into a curved sided segment and remove the remaining small volume of surface error with deterministic small tools. The curved-sided segment is then finely polished with deterministic tools as was done for the 18 hexagonal segments of the JWST primary mirror.

Pinwheel mirror segments may be made of a number of different materials. For example, SCHOTT offers extremely stable monolithic mirror substrates of ZERODUR. These have been aggressively light-weighted up to 4-m in diameter. A pinwheel segment can be undercut around its perimeter, as shown in **Figure B-9**. The steps to processing would be: 1. cut the roundel, 2. mill to near optical shape, 3. lightweight by removing up to 90% material, leaving "lands" for mounting, and 4, acid etch to mitigate subsurface damage. The segment would be light-weighted as an isogrid (not the rectangular grid pattern shown in **Figure B-9**) to minimize mass and give maximum strength for launch and alignment stability. After optical fabrication as an off-axis roundel the petal would be parted out by machining.

C. PROCEDURES FOR COATING 4-METER MAYALL PRIMARY MIRROR AND THE 3.75-M MIRROR-LAB TEST MIRROR.

Purpose

      This procedure describes the processes for stripping/removing optics first surface in preparation for re-aluminizing optics. The document includes an overview of chemicals, preparation of chemicals and materials, and removal of optics 1st surface.

Applicable To

      Aluminizing Procedure

Scope

      The scope of this document is to outline the procedure for proper removal of evaporated aluminum coating from a mirrors substrate, and how to properly clean and prepare a mirror for a new evaporated aluminum coating.

Definitions

Training

1.   Respirator Fit Tested

2.   Handling of caustic chemicals

Safety

1.   JHA Form

2.   Daily Briefing Form

Personnel, Equipment and Materials Required

      The supplies needed for removing the aluminum coating are shown in Table 1 below.

Chemicals		
	Hydrochloric Acid	
	Copper Sulfate	
	Potassium Hydroxide	
	Nitric Acid	
	Calcium Carbonate	$CaCO_3$
Cleaning Materials		
	Orvus Soap	1 oz. / 1 US gal. H_2O
	Sea Sponge	Conditioned prior to use*
	TexWipes 609 Wipers	
	Kaydry	
	Long Q Tips	
	Dust Masks	

	Hair Net	
	Nitrile Gloves	
	Eye Protection	
	Water Boots	
	Water Bib	
	Distilled Water	
	Pressurized Spray Bottles	1 with soap mix
		1 with distilled water
	Visqueen Plastic	
	3M 764 Orange Tape	Or cloth type duct tape
Safety		
	Chemical Resistant Suit	
	Chemical Resistant Gloves	Ansel Edmont Sol-Vex
	Chemical Resistant Boots	
	OSHA Respirator	Acid Vapor Cartridge

Conditioned: Soaked in a 2%-10% HCl/H$_2$O Solution until coral dissolved Table 1: Supplies and Tools

Procedure

Overview

1. The following tasks are to be planned prior to and during the optics aluminum coating removal process.

   a. Perform a visual inspection of each component to assess the overall condition. Document and make notes of any anomalies that are observed.

   b. Stage the area with all necessary equipment/tools used during the removal process.

   c. Ensure all personnel involved understand the daily process, safety and goals.

   d. A safety meeting is held every day prior to any work taking place and again at the end of the day to discuss any safety issues.

   e. For steps 2 through 8, use Ansel Edmont Sol-Vex chemical resistant gloves (style 37-185, size 10, 22 mil. thick by 18" long). Then change to a powder free nitrile or latex (clean room type) glove during the final rinse, drying and inspection stages, taking care to change gloves whenever they become contaminated.

   f. For steps 2 through 8 chemical protection suits, goggles, and appropriate respirators are required.

   g. **Do not** allow any wipers to contact the side of mirror and then continue to be used on the optical surface.

Aluminum Coating Removal, Chemical Preparation:

The recipes for mixing the chemicals are as follows:

Chemical "A"

(Hydrochloric Acid and Copper Sulfate, also locally known as "Green River")

1.   2.72 kg (6 lb) hydrochloric acid (HCl, 37%) reagent grade.

2.   227 g (0.5 lb) cupric sulfate ($CuSO_4$ $5H_2O$) reagent grade.

3.   Put 6 L of distilled water into a 10 L (2.5 US gal) container and add HCl and $CuSO_4$ $5H_2O$. Add distilled water to make 10 L (2.5 US gal). Shake until $CuSO_4$ $5H_2O$ is dissolved.

Chemical "B" (Potassium Hydroxide)

1.   2 cups (dry measure) potassium hydroxide (KOH) reagent grade pellets.

2.   Put 6 L of distilled water into a 10 L (2.5 US gal) container and add KOH pellets. Add distilled water to make 10 L (2.5 US gal). Shake until KOH is dissolved.

Chemical "C" (Nitric Acid)

1.   3.2 kg (7 lb) nitric acid (HNO_3, 70%) reagent grade.

2.   Put 6 L of distilled water into a 10 L (2.5 US gal) container and add HNO_3. Add distilled water to make 10 L (2.5 US gal).

Aluminum Coating Removal Procedure:

The following procedures assume all necessary materials are available and accessible. At a minimum, 2 people are needed to perform this operation. As a rule of thumb, it has been found that one person per meter diameter of mirror are required to clean the mirror and at least one additional person to handle supplies and hoses for the cleaning crew. The process below assumes 5 people. The entire operation should able to be completed in about 1 day.

1.   Gently wash the mirror with distilled water and Orvus soap (1 oz. Orvis per 1 US gal H_2O) to remove large particulates. Inspect the mirror for any oils and remove using reagent grade acetone and Kaydry EX-L Delicate Task wipers.

2.   Cover the mirror with Kaydry EX-L Delicate Task wipers and then pour on **"A"**. With a gloved hand smooth out the saturated wipers to keep the liquid in place on the surface. When most of the aluminum is removed, gather the saturated wipers into wads and swab any remaining spots. After the optical surface is clean use the saturated wads to remove any aluminum from the side of the mirror.

Note: After working on the side of the mirror discard the saturated wad and **DO NOT** return to work on the optical surface or risk contamination.

3.   Rinse with filtered water and clean gloves.

4.   Sprinkle calcium carbonate ($CaCO_3$) on the mirror and wet with **"B"** while rubbing with a wad of three or four Kaydry EX-L Delicate Task wipers, also wet with **"B"**. The resultant slurry is thoroughly scrubbed over the surface in a circular or figure eight swirling motion, paying particular attention to the edges and adding more **"B"** as necessary to keep the $CaCO_3$ from caking or drying out.

Note: After working on the side of the mirror discard the saturated wad and **DO NOT** return to work on the optical surface or risk contamination.

5.   Rinse with filtered water.

6.   Repeat step 4 using **"B"** and $CaCO_3$ at least three times, with rinses in between.

7.   Rinse with filtered water and clean gloves.

8.   Pour on **"C"** as a rinse and quickly swab with a wad Kaydry EX-L Delicate Task wipers. This step will remove all traces of calcium carbonate.

        Note: After working on the side of the mirror discard the saturated wad and **DO NOT** return to work on the optical surface or risk contamination.

9.   Rinse with filtered water for five to ten minutes. Final rinse with bottled deionized or distilled water. Remove chemical protection suits and switch to nitrile or latex cleanroom gloves.

10.   Systematically dry the mirror using two sheets of TexWipe 609 wipers at a time. Holding a corner of the wipers with one hand, place the other hand on the wipers to make contact with the substrate and drag the wipers toward the edge of the mirror and off. Starting from a dry area pull the wiper into the wet edge and follow this edge to the side of the mirror and off again. This is repeated until the entire surface is dried.

        Note: Never allow the water to evaporate from the substrate, always dry with clean wipes.

11.   A final "buff" of the optical surface is done using a Texwipe 609 wipe with a drop or two of reagent grade ethanol. The wiper is folded such that it covers the entire gloved hand (preventing the glove from touching the surface) and the entire surface is rubbed using a circular motion several times.

        Note: The wiper pad with the minute quantity of ethanol on the center wets the surface and simultaneously dries it – you should not see any ethanol streaks evaporating as the wiper is rubbed on the surface. As the wiper is rubbed on the surface it is possible to feel a contaminated area by feeling a change in the drag of the wiper. These areas are attended to using freshly prepared ethanol spotted wipers until no change in drag is felt over the entire surface.

12.   Use CO_2 snow or filtered gaseous nitrogen (N_2) to blow off any dust or lint.

13.   With the room lights dimmed, inspect surface with high intensity lamps for lint, drying streaks and soils.

        Note: It has been found that if the final ethanol buffing has been done correctly, an inspection with a high intensity LED light source will not be necessary. If the soils are not removed by buffing, it may be necessary to go back and repeat the process from step 4.

14.   Just before closing the chamber use CO_2 snow for a final dust off.

 Procedure Review

Records

1.   JHA signature sheet; kept by safety office, scanned and stored \ets_share\Safety

2.   Fall protection training: kept by Safety Office

3.   Rigging, suspended load: kept by Safety office

4.   Maintenance record

References

1.   KPNO Emergency Manual

2.   Other procedures that are called out list by number

D.   REFERENCES

1 Chipman, R. A. , W. T. Lam, G. Young (2019) *Polarized Light and Optical Systems* CRC Press International Standard Book Number-13: 978-1-4987-0056-6. 975 page textbook.

2 Breckinridge, J. B. (2012) *Basic Optics for the Astronomical Sciences,* Ch 2 and 3. 400 page textbook SPIE Press.

3 WFIRST-*AFTA 2015 Report by the Science Definition Team (SDT) and WFIRST Study Office. D. Spergle*, N. Gehrels, C. Baltay, D. Bennett J. Breckinridge, M. Donahue, et. al.

4 HabEx Habitable Exoplanet Observatory: Exploring new worlds, Understanding our Universe. download @ https://www.jpl.nasa.gov/HabEx/pdf/HabEx-Final-Report-Public-Release.pdf

5 LUVOIR Large UV/Optical/IR surveyor https://asd.gsfc.nasa.gov/luvoir/reports/

6 Brian Daugherty (2019) *Advances In Polarization Engineering* Chapter 1: *Form Birefringence of 3.75 Meter Aluminum Mirror,* PhD dissertation College of Optical Sciences University of Arizona, Tucson AZ 85712.

[7] Bolcar, M., K. N. Balasubramanian, M. Clampin, J. Croocke, L. Feinberg, M. Postman, et. al. *"Technology development for advanced large aperture space telescope (ATLAST) as a Candidate LUVOIR system"*, (2015)

[8] Lillie, C. F. and J. B. Breckinridge *"Prime focus architectures for large space telescopes: reduce surfaces to save cost",* Proc SPIE 9904 – 4K (2016)

9 Breckinridge, J., N. Bryant, J. Lorre (2008) Innovative pupil topographies for sparse aperture telescopes and SNR, Proc. SPIE 7013, 2008.   doi: 10.1117/12.787011

10 Shao, M. , J. Catanzarite, X. Pan (2010) THE SYNERGY OF DIRECT IMAGING AND ASTROMETRY FOR ORBIT DETERMINATION OF EXO-EARTHS, ApJ, 720

11 E. Ribak, F. Roddier, C. Roddier and J. B. Breckinridge (1987) Signal to noise limitations in white-light holography Applied Optics, vol 27, 1183 to 1186

12 Stam, M., Hovenier, J. W. & Waters, L. B. F. M. 2004, Astron. & Astroph, 428, 663

13 Tomasko, M. G. & Doose, L. R. 1984, Icarus, 58, 1

14 West, R. A., Sato, M. & Hart, H. 1983, Journal of Geophysical Review-Space Physics, 88, 8699

15 Gehrels, T., Herman, B. M. & Owen, T. 1969, Astron. J., 74, 190

16 Stam, M., Hovenier, J. W. & Waters, L. B. F. M. 2004, Astron. & Astroph, 428, 663

17 Berdyugina, S. V., Berdyugin, A. V., Fluri, D. M. & Piirola, V. 2011, ApJL, 728, L6

18 de Kok, R. J., Stam, D. M., & Karalidi, T. 2012, ApJ, 741, 59

19 Stolker, T. M. Sitko, B. Lazareff (2017), ApJ 849, #143.

20 Ginski, C. ; M. Benisty and R. G. van Holstein, Et. Al (2018) Astron. & astroph. Vol. 616, article # A79

21 Karalidi, T., Stam, D. M. & Hovenier, J. W. 2011, Astron. and Astroph, 530, A69

22 Madhusudhan, N. & Burrows, A. 2012, ApJ, 747, 25

23 Fluri, D. M. & Berdyugina, S. V. 2010, A&A, 512, A59

24 Graham, J. R., Kalas, P. G. & Matthews, B. C. 2007, ApJ, 654, 595

25 Perrin, M. D., et al. 2009a, ApJ, 707, L132   and Perrin, M. D., et al. 2009b, *iii* Proceedings of the international conference. AIP Conference Proceedings, 1158, 17

26 M. Born and E. Wolf (1999) **Principles of Optics**, Chapter 10: *Partially coherent light*, Cambridge University Press

27 L. Mandel & E. Wolf (1965) *Coherence Properties of Optical Fields*, Rev. Mod. Phys **37**, 231-280

28 J. Goodman (2015) *Statistical Optics* 2nd edition Ch 5: *Coherence of Optical Waves*, Wiley ISBN 978-1-119-00945-0

[29] R. Gerharz (1977) *Polarization-dependent MTF defects in off-axis imaging systems*, Optik, 48 #1 23-28

[30] R. E. Swing and J. R. Clay, (1967) J. Opt. Soc. Am. 57, 1180-1185

[31] A. Thelen, *Design of Optical Interference Coatings* (McGraw-Hill, New York, 1988). AND

H. A. Macleod, *Thin-Film Optical Filters* (Institute of Physics, 2002), pp. 185–186. AND J.A. Dobrowolski, "Coatings and Filters," in *Handbook of Optics*, W.G. Driscoll and W. Vaughan, ed. (McGraw-Hill, New York. 1978), 8.1-8.124.

[32] R. M. A. Azzam and N. M. Bashara (2003) *Ellipsometry and Polarized Light,* North Holland – Elsevier ISBN 0 4444 87016 4 ; 527 pages.

[33] Ward, L. 1988, *Optical Constants of Bulk Materials and Films*, Adam Hilger, p245

[34] E. M. Purcell and D. J. Moran (2013) *Electricity and Magnetism 3rd Ed.* , Cambridge University Press

[35] H. A. Macloed (2001) "*Thin-film optical filters 3rd ed*" Ch # 10 Factors affecting layer and coating properties pp 462-485 Institute of Physics, publisher Bristol and Philadelphia

[36] E, Hecht (2002) *Optics 4th* edition Addison Wesley ISBN 0-321-18878-0

[37] Breckinridge, Lam, Chipman (2015) "*Polarization Aberrations in Astronomical Telescopes: The Point Spread Function*", Publications of the Astronomical Society of the Pacific**,** 127**:445–468**

[38] Chipman, Lam and Breckinridge (2015) "*Polarization aberrations in astronomical telescopes*" Proc SPIE 9613-16

[39] R. C. Jones, (1941) JOSA, 31, 488

[40] E. Wolf (2007) *Theory of Coherence and Polarization of Light,* Chapter 8, Cambridge University Press, 225 page book. And J. W. Goodman (2015) Statistical Optics, Wiley And J. D. Strong (1958) Classical Optics, Freeman, page 178 *interference of polarized light,.*

[41] E. Wolf (2007) *Theory of Coherence and Polarization of Light,* Chapter 8, Cambridge University Press, 225 page book. And J. W. Goodman (2015) *Statistical Optics*, Wiley And J. D. Strong (1958) *Classical Optics*, Freeman, page 178 *interference of polarized light,.*

[42] J.P. McGuire, Jr., R.A. Chipman, *Diffraction image formation in optical systems with polarization aberrations I: Formulation and example, Journal of the Optical Society of America A.*, vol. 7, no. 9, pp. 1614-1626 (Sept. 1990).

[43] James B. Breckinridge, Wai Sze T. Lam and Russell A. Chipman, *Polarization Aberrations in Astronomical Telescopes: The Point Spread Function*, Publications of the Astronomical Society of the Pacific (PASP), 127**:445–468** May 2015

[44] Russell A. Chipman, Wai Sze T. Lam and James B. Breckinridge *Polarization Aberration in Astronomical Telescopes*, Proc. SPIE 9613-16, Polarization Science and Remote Sensing VII , San Diego, CA 2015

[45] J. Davis, M. Kupinski, R. A. Chipman and J. B. Breckinridge (2018) *HabEx Polarization Ray Trace and aberration analysis,* Proc. SPIE 10689-H3

[46] J. B. Breckinridge, M. Kupinski, J. Davis, B. Daugherty, R. A. Chipman (2018) *Terrestrial Exoplanet coronagraph image quality polarization aberrations in HabEx,* Proc SPIE 10698-1D

[47] N. Clark & Breckinridge, J. *Polarization compensation of Fresnel aberrations in telescopes*. 2011 SPIE 8146 # 81460O

[48] W. S. T. Lam and Russell Chipman (2015) *Balancing polarization aberrations in crossed fold mirrors,* Applied Optics 54, 3236-3245.

[49] J. Krist, Martin, S., Kuan, G., Mennesson, G., Ruane, G. et.al. (2019) *Numerical Modeling of the HabEx coronagraph*, Proc. SPIE 1111705, 16 pages.

[50] F. Horowitz (1983) *Structure-induced optical anisotropy,* PhD dissertation, College of Optical Sciences, University of Arizona, Tucson, AZ. 120 pages

[51] Breckinridge, J. B. & Oppenheimer, B. 2004, ApJ, 600, 1091

[52] J. B. Breckinridge (2004) *Image formation in high-contrast optical systems: the role of polarization*, SPIE 5487 doi:10.1117/12.548932; http://dx.doi.org/10.1117/12.548932

[53] Shaklan, S. B. and J. J. Green (2006) *Reflectivity and optical surface height requirements in a broadband coronagraph* Applied Optics 45, 5143-5153

[54] J. W. Goodman, 2010, *Some properties of speckle from smooth objects*, Optical Engineering 49, 068001.

[55] Bruegge, T. J. 1989, Proc. SPIE, 1166, 165

[56] Chipman, R. A. 1989a, "*Polarization analysis of optical systems*". Opt. Eng., 28, 90 and 1989b, Proc. SPIE, 1166, 79.

[57] Wolff, L. B. and D. J. Kurlander, 1990, *IEEE Computer Graphics and applications* vol. 10, 6, 44–55.

[58] J.D. Trolinger, Jr., R.A. Chipman, D.K. Wilson, (1991) *Polarization ray tracing in birefringent media*, *Optical Engineering*, vol. 30, no. 4, pp. 461-466 (April 1991).

[59] Yun, G., Crabtree, K. & Chipman, R., 2011a, Appl. Opt. 50, 2855 & 2011b, AND Appl. Opt. 50, 2866

[60] S.C. McClain, L.W. Hillman, R.A. Chipman, (1993) *Polarization ray tracing in anisotropic optically active media I, algorithms, & II, theory and physics*, *Applied Optics* vol. 10, no. 11, pp. 2371-2393.

[61] R. A. Chipman and W. S. T. Lam (2015) *The Polaris-M ray tracing program,* Proc. SPIE 9613-18

[62] Kuboda, H. & Inoué, S. 1959, JOSA, 49, 191

[63] Urbanczyk, W. 1986, Opt. Acta., 33, 53

[64] McGuire, J. P. & Chipman, R. A. 1990, JOSA A, 7, 1614 & 1991, JOSA A, 8, 6

[65] Tu, Y., Wang, X., Li, S. & Cao, Y. 2012, Opt. Lett., 37, 2061

[66] R.A. Chipman, L.J. Chipman, (1989) *Polarization aberration diagrams*, *Optical Engineering*, vol. 28, no. 2, pp. 100-106.

[67] J.P. McGuire, Jr., R.A. Chipman, (1994) *Polarization aberrations I: Rotationally symmetric optical systems and Polarization aberrations II: Tilted and decentered optical systems*, *Applied Optics*, vol. 33, no. 2, pp. 5080-5107.

[68] D.J. Reiley, R.A. Chipman, (1994) *Coating-induced wave-front aberrations: On-axis astigmatism and chromatic aberration in all-reflecting systems* *Applied Optics*, , vol. 33, no. 10, pp. 2002-2012.

[69] I. C. Gardner (1927) *Application of the Algebraic Aberration Equations to Optical Design, NBS Scientific Papers* Vol 22 # 550.

[70] Stefan Martin, Mayer Rud, Paul Scowen, Daniel Stern, Joel Nissen, John Krist (2017), <u>*HabEx Space Telescope Optical System*</u>. Proceedings of the SPIE, Vol 10398 Paper # 05

[71] Ibid.

[72] W. S. T. Lam and R. A. Chipman (2015) *Balancing polarization aberrations in crossed fold mirrors*, Applied Optics **54**, 3236-3245

[73] Clark and Breckinridge (2011) *Polarization compensation of Fresnel aberrations in telescopes*, Proc. SPIE 81460 O

[74] J. B. Breckinridge, W. Lam and R. A. Chipman (2015) Polarization aberrations in astronomical telescopes: the Point Spread Function, Publication of the Astronomical Society of the Pacific 127:445-468

[75] J. B. Breckinridge (1971) *Polarization Properties of a Grating Spectrograph*, Applied Optics 10, 286-294,

[76] J. B. Breckinridge, *Image-formation in high contrast optical systems: the role of polarization*, SPIE Proc 5487, doi: 10.1117/12.548932; 1337-1345.

[77] I. J. Hodgkinson, "*Optical anisotropy in thin films deposited obliquely: in situ observations and computer modeling,*" Applied Optics, vol. 30, p. 1303, 4 1991.

[78] S. Liedtke, C. Grüner, A. Lotnyk and B. Rauschenbach, "*Glancing angle deposition of sculptured thin metal films at room temperature,*" Nanotechnology, vol. 28, p. 385604, 9 2017.

[79] S. Liedtke, C. Grüner, A. Lotnyk and B. Rauschenbach, "*Glancing angle deposition of sculptured thin metal films at room temperature,*" Nanotechnology, vol. 28, p. 385604, 9 2017.

80 A. Barranco, A. Borras, A. R. Gonzalez-Elipe and A. Palmero, "*Perspectives on oblique angle deposition of thin films: From fundamentals to devices*," Progress in Material Sciences; vol. 76, pp. 59-153, 2016.

81 D. O. Smith, M. S. Cohen and G. P. Weiss, "*Oblique-Incidence Anisotropy in Evaporated Permalloy Films*," Journal of Applied Physics, vol. 31, pp. 1755-1762, 10 1960

82 N. Nakhodkin, "*Effect of vapour incidence angles on profile and properties of condensed films,*" Thin Solid Films, vol. 10, pp. 109-122, 4 1972.

83 A. Dirks, "*Columnar microstructure in vapor-deposited thin films*," Thin Solid Films, vol. 47, pp. 219-233, 12 1977.

84 L. Abelmann and C. Lodder, "*Oblique evaporation and surface diffusion*," Thin Solid Films, vol. 305, pp. 1-21, 8 1997.

85 K. Robbie and M. J. Brett, "*Sculptured thin films and glancing angle deposition: Growth mechanics and applications*," vol. 15, pp. 1460-1465, 1997.

86 R. Messier, V. C. Venugopal and P. D. Sunal, "*Origin and evolution of sculptured thin films*," Journal of Vacuum Science Technology A: Vacuum Surfaces and Films, vol. 18, pp. 1538-1545, 7 2000.

87 A. Lakhtakia, R. Messier and D. K. Paul, *"Sculptured Thin Films: Nanoengineered Morphology and Optics,"* Physics Today, vol. 59, p. 70, 2006.

88 Y. He and Y. Zhao, "*Advanced multi-component nanostructures designed by dynamic shadowing growth,"* vol. 3, p. 2361, 2011.

89 J. B. Breckinridge, "*Image formation in high-contrast optical systems: the role of polarization*," in Optical, Infrared, and Millimeter Space Telescopes, SPIE proc # 5487, pp 1337 to 1352 2004.

90 J. B. Breckinridge and B. R. Oppenheimer, "*Polarization Effects in Reflecting Coronagraphs for White-Light Applications in Astronomy*," The Astrophysical Journal, vol. 600, pp. 1091-1098, 1 2004.

91 J. R. Gee, I. J. Hodgkinson and P. W. Wilson, "*Reflection anisotropy in evaporated aluminum: Consequences for telescope mirror coatings,*" Journal of Vacuum Science & Technology A: Vacuum, Surfaces, and Films, vol. 4, pp. 1875-1878, 7 1986.

92 N. Woolf and J. R. Angel, "*Astronomical Searches for Earth-Like Planets and Signs of Life*," Annual Review of Astronomy and Astrophysics, vol. 36, pp. 507-538, 9 1998.

93 J. E. Krist, J. T. Trauger, S. C. Unwin and W. A. Traub, *End-to-end coronagraphic modeling including a low-order wavefront sensor*, vol. 8442, M. C. Clampin, G. G. Fazio, H. A. MacEwen and J. M. Oschmann, Eds., SPIE, 2012, pp. 8442 - 8442 - 11.

94 H. P. Stahl, *Overview and performance prediction of the baseline 4-meter telescope concept design for the habitable-zone exoplanet observatory,* vol. 10698, H. A. MacEwen, M. Lystrup, G. G. Fazio, N. Batalha, E. C. Tong and N. Siegler, Eds., SPIE, 2018, pp. 10698 - 10698 - 10.

95 H. P. Stahl, M. Postman, G. Mosier, W. S. Smith, C. Blaurock, K. Ha and C. C. Stark, "*AMTD: update of engineering specifications derived from science requirements for future UVOIR space telescopes*," in Space Telescopes and Instrumentation 2014: Optical, Infrared, and Millimeter Wave, 2014.

96 L. B. Wolff and D. J. Kurlander, "*Ray tracing with polarization parameters*," IEEE Computer Graphics and Applications, vol. 10, pp. 44-55, 11 1990.

97 Y. Tu, X. Wang, S. Li and Y. Cao, "*Analytical approach to the impact of polarization aberration on lithographic imaging,*" Optics Letters, vol. 37, p. 2061, 5 2012.

[98] G. Yun, K. Crabtree and R. A. Chipman, "*Three-dimensional polarization ray-tracing calculus I: definition and diattenuation,*" Applied Optics, vol. 50, p. 2855, 6 2011.

[99] G. Yun, S. C. McClain and R. A. Chipman, "*Three-dimensional polarization ray-tracing calculus II: retardance,*" Applied Optics, vol. 50, p. 2866, 6 2011.

[100] R. M. A. Azzam, "*Direct relation between Fresnel's interface reflection coefficients for the parallel and perpendicular polarizations*," Journal of the Optical Society of America, vol. 69, p. 1007, 7 1979.

[101] R. M. A. Azzam and N. M. Bashara, *Ellipsometry and Polarized Light* (North-Holland Personal Library), North Holland, 1988, 500 page book .

[102] E. Garcia-Caurel, A. D. Martino, J.-P. Gaston and L. Yan, "*Application of Spectroscopic Ellipsometry and Mueller Ellipsometry to Optical Characterization,*" Applied Spectroscopy, vol. 67, pp. 1-21, 1 2013.

[103] I. Ohlídal and D. Franta, "*Ellipsometry of Thin Film Systems,*" in Progress in Optics, Elsevier, 2000, pp. 181-282.

[104] R. M. A. Azzam and A. G. Lopez, "*Accurate calibration of the four-detector photopolarimeter with imperfect polarizing optical elements*," Journal of the Optical Society of America A, vol. 6, p. 1513, 10 1989.

[105] R. M. A. Azzam, E. Masetti, I. M. Elminyawi and F. G. Grosz, "*Construction, calibration, and testing of a four-detector photopolarimeter*," Review of Scientific Instruments, vol. 59, pp. 84-88, 1 1988.

[106] K. Brudzewski, "*Static Stokes Ellipsometer: General Analysis and Optimization,*" Journal of Modern Optics, vol. 38, pp. 889-896, 5 1991

[107] D. H. Goldstein, "*Mueller matrix dual-rotating retarder polarimeter,*" Applied Optics, vol. 31, p. 6676, 11 1992.

[108] P. K. Smith, (2013) "*Characterizing dielectric tensors of anisotropic materials from a single measurement*,"

[109] E. Compain, S. Poirier and B. Drevillon, "*General and self-consistent method for the calibration of polarization modulators, polarimeters, and Mueller-matrix ellipsometers,*" Applied Optics, vol. 38, p. 3490, 6 1999.

[110] Chipman, Russell A. Polarized Light and Optical Systems (2019), CRC Inc, 800 page text book

[111] Green, Joseph J. and Stuart B. Shaklan (2006) "*Reflectivity and optical surface height requirements in a broadband coronagraph. 1. Contrast floor due to controllable spatial frequencies*" Applied Optics 45, 5143-5153

[112] A. Ciattoni and C. Palma, "*Optical propagation in uniaxial crystals orthogonal to the optical axis: paraxial theory and beyond*," Journal of the Optical Society of America A, vol. 20, p. 2163, 11 2003.

[113] S. C. McClain, L. W. Hillman and R. A. Chipman, "*Polarization ray tracing in anisotropic optically active media I Algorithms,*" Journal of the Optical Society of America A, vol. 10, p. 2371, 11 1993.

[114] S. C. McClain, L. W. Hillman and R. A. Chipman, "*Polarization ray tracing in anisotropic optically active media II Theory and physics,*" Journal of the Optical Society of America A, vol. 10, p. 2383, 11 1993.

[115] A. Yariv and P. Yeh, *Optical Waves in Crystals: Propagation and Control of Laser Radiation*, Wiley-Interscience, 1983

[116] Bass, Decusatis, & Enoch (2009). *Handbook of Optics, Third Edition Volume IV: Optical Properties of Materials, Nonlinear Optics, Quantum Optics* (set) ISBN-13: 978-0071498920

[117] W. S. T. Lam, (2015) "*Anisotropic ray trace*," University of Arizona PhD dissertation; 306 pages

[118] John Krist, Stefan Martin, Gary Kuan, Bertrand Mennesson, Garreth Ruane; *Numerical modeling of the Habex coronagraph*. Proc. SPIE 11117-05 2019.

[119] From Stephen Martin, NASA JPL. The HabEx optical prescription dated 2017. Private communication

[120] Krist, J., S. Martin, G. Kuan, B. Mennesson, G. Ruane, N. Saini, J. Trauger, J. Breckinridge, D. Mawet, P. Stahl, J. Davis (2019) *Numerical modeling of the Habex coronagraph*, Proc. SPIE 11117-05

[121] From Davis, J., M. Kupinski, R. Chipman, and J. Breckinridge; *HabEx Polarization Ray Trace and Aberration Analysis*, Proc. SPIE, 10698-120, 2018.

[122] LUVOIR Final Report pp 8-17 , 2019

[123] Segmented Coronagraph Design and Analysis (SCDA) Study ; ExoPlanet Program Office summary in LUVOIR Final Report

[124] J. B. Breckinridge (1971) *Polarization properties of a grating spectrograph*, Applied Optics, pp 287-294

[125] Trunbull, M. C., ExoCat-1: The Nearby Stellar Systems Catalog for Exoplanet Imaging Missions, arXiv:1510.01731 [astroph.SR] arXiv:1510.01731 [astro-ph.SR] chapter 1; 2015.

[126] Beckwith, S. V. W.; M. Stailelli, A. M. Koekemoer, J. A. R. Calswell, et. al.; "*The Hubble Ultra Deep Field*" Astron. J. 132:1729-1755 (2006).

[127] Breckinridge, J. B., T. G. Kuper and R. V. Shack "*Low-scattered light camera: a model*" Optical Engineering 23, pp 816-820; (1984)

[128] Harvey, J. E., R. N. Pfister and J. B. Breckinridge, "*The role of narrow angle forward surface scatter and particulate scatter in exoplanet exploration*", Proc SPIE 10698-188, 2018.

[129] Troy, M. and G. Chanan, "*Diffraction effects from giant segmented-mirror telescopes,*" Appl.Opt.42,3745–3753(2003). 30-meter diameter CELT telescope, (renamed the Thirty Meter Telescope or TMT which uses 1.44 meter segments)

[130] Pueyo, L., and Norman, C., *High Contrast Imaging with an arbitrary aperture: active compensation of aperture discontinuities*. The Astroph. Journ., 769:102 (31pp), doi:10.1088/0004-637X/769/2/102 C _2013.

[131] Garreth Ruane, Dimitri Mawet, Jeffrey Jewell, Stuart Shaklan, "*Performance and sensitivity of vortex coronagraphs on segmented space telescopes*," Proc. SPIE 10400, 104000J ; doi: 10.1117/12.2274508 (2017)

[132] Jewell, J. G. Ruane, S. Shaklan, D. Mawet, D. Redding, "*Optimization of coronagraph design for segmented aperture telescopes*," Proc. SPIE 10400, 104000H; doi: 10.1117/12.2274574 (2017)

[133] Vanderbei, R.J., Spergel, D.N., and Kasdin, J.N., "*Spiderweb Masks for High Contrast Imaging,*: ApJ vol. 590, 593, 2003.

[134] Lillie, C., M. Flannery, D. Dailey "*Segmented Telescopes For Coronagraphs*" Proc of SPIE Vol. 5487 0277-786X/04/$15 · doi: 10.1117/12.552348 (2004)

[135] Alexis Carlottia, Dimitri Mawet, Laurent Pueyo *Optimal apodizers for the vector vortex coronagraph with on-axis telescopes*, Proc. of SPIE Vol. 8864, 88641P; CCC code: 0277-786X/13/$18 · doi: 10.1117/12.2024511

[136] Breckinridge, J. B. "*The pinwheel pupil discovery: exoplanet science and improved processing with segmented telescopes*" Paper # 439.04 231st meeting of the American Astronomical Society, Washington, DC. January 2018.

[137] C. H. Werenskiold (1941) "*Improved Telescope Spider Design*", Journ. Royal Astron. Soc. Canada, 35, 268-272. AND C. H. Werenskiold, ''*A note on curved spiders*,'' Sky Telesc. 262–263, 1969

[138] Richter, J. L. (1984) "*Spider diffraction: a comparison of curved and straight legs*", AO, 23 1907-1913

[139] Harvey, J. E. , R. G. Irvin, K. Crabtree, R. N. Pfister and J. B. Breckinridge "*Diffraction Analysis of Large Segmented Mirror Concepts for Exoplanet Exploration*", SPIE proceedings 10698-060, 2018.

[140] J. E. Harvey, R. G. Irvin and R. N. Pfisterer, "*Modeling Physical Optics Phenomena by Complex Ray-tracing*", Opt. Eng., 54 (3), 035105 (2015). doi: 10.1117/1.OE.54.3.035105.

[141] Harvey, J. E. and C. Ftaclas, "*Diffraction Effects of Telescope Secondary Mirror Spiders upon Various Image Quality Criteria*", Appl. Opt. 34, 6337-6349 (1995).

[142] Harvey, James E., James B. Breckinridge, Ryan G Irvin, Richard N. Pfisterer, (2018) "*Novel Designs for minimizing diffraction effects in large segmented mirror telescopes*", SPIE 10745 -0L

[143] Breckinridge, James B. , James Harvey, Karleton Crabtree, et. al. "*ExoPlanet telescope diffracted light minimized: the pinwheel pupil solution*", SPIE Proc 10698-1P (2018)

[144] Chunlin Miao, Shai Shafrir, John Lambropoulos, Joni Mici, et. al. "*Shear stress in magnetorheological finishing for glasses*", Applied Optics 48, 2585-2595, (2009)

[145] Lillie, C. F. , H. A. MacEwen, R. S. Polidan and J. B. Breckinridge "*A 4-m evolvable space telescope configured for NASA's HabEx Mission: the initial stage of LUVOIR*", Proc. SPIE 103980R (2017)

[146] Polidan, R. S., Breckinridge, J. B., Lillie, C. F., MacEwen, H. A., Flannery, M. R., and Dailey, D. R., "*Innovative telescope architectures for future large space observatories*", JATIS 2(4), 041211, (2016)

147 Nelson, J. , T. S. Mast, (1982) *Figure control for a fully segmented telescope mirror* , Applied Optics, 21, 2631 to 2641